



Review

Diversity of Iron Oxides: Mechanisms of Formation, Physical Properties and Applications

Kamil G. Gareev^{1,2}

¹ Department of Micro and Nanoelectronics, Saint Petersburg Electrotechnical University “LETI”, 197022 Saint Petersburg, Russia; kggareev@etu.ru

² Engineering Centre for Microtechnology and Diagnostics, Saint Petersburg Electrotechnical University “LETI”, 197022 Saint Petersburg, Russia

Abstract: Iron oxide compounds have naturally formed during the whole of Earth’s history. Synthetic compositions with iron oxides are produced with the use of various techniques and widely used for scientific and applied purposes. This review considers an attempt to classify all the information on different iron oxide compound formation mechanisms and intended applications in biomedicine, catalysis, waste remediation, geochemistry, etc. All the literature references analyzed were divided into several groups by their number of included iron oxide compounds: compositions containing only one compound (e.g., magnetite or wüstite), including various polymorphs of iron(III) oxide (α -, β -, γ -, ε -, ζ -, δ - Fe_2O_3); compositions with two different distinguishable iron oxide phases (e.g., maghemite and hematite); compositions containing non-crystalline phases (amorphous iron oxide or atomic clusters); and compositions with mixed iron oxide phases (indistinguishable separate iron oxide phases). Diagrams on the distribution of the literature references between various iron oxide compounds and between various applications were built. Finally, the outlook on the perspectives of further iron oxide studies is provided.

Keywords: iron oxides; phase diagrams; mechanisms of formation; synthetic materials; biomimetic materials; biogenic materials; iron oxide application



Citation: Gareev, K.G. Diversity of Iron Oxides: Mechanisms of Formation, Physical Properties and Applications. *Magnetochemistry* **2023**, *9*, 119. <https://doi.org/10.3390/magnetochemistry9050119>

Academic Editor: Alejandro Gómez Roca

Received: 7 March 2023

Revised: 14 April 2023

Accepted: 25 April 2023

Published: 27 April 2023



Copyright: © 2023 by the author. Licensee MDPI, Basel, Switzerland. This article is an open access article distributed under the terms and conditions of the Creative Commons Attribution (CC BY) license (<https://creativecommons.org/licenses/by/4.0/>).

1. Introduction

The chemistry of iron is of great interest because iron is an abundant element present in various fields [1]. The elemental abundance of oxygen, hydrogen and iron at the surface of and within the Earth’s crust has fostered widespread occurrences of iron oxides and oxyhydroxides in a diverse range of aquatic and terrestrial environments; most of the known iron oxides and oxyhydroxides are known to occur in nature [2]. Iron oxides are formed naturally through the weathering of Fe-containing rocks both on land and in the oceans and play an important role in geochemistry [3]. Iron-rich sedimentary rocks have had important implications in the evolution of Earth’s atmosphere and hydrosphere [4]. Iron oxide copper gold, apatite-magnetite and other ore deposits have very important heavy industrial applications [5,6]. There are iron oxides on the surface of Mars, in the depths of Earth, in old rusting factories, in pigeon brains and magnetotactic bacteria [7]. Despite the precise mechanism of biogenic magnetite mineralization on early Earth still being unknown, the understanding of this mechanism includes the origin of banded iron formations [8]. Iron oxides are also linked to pathological states of the human body, such as iron dysregulation in the brain and neurological disorders [9,10].

Metallurgy has been developed relating to iron and iron oxides and used for various applications including colored pigments, magnetic materials, catalysts, water oxidation, biomedical uses including therapy and diagnostics, etc. [1,11–14]. The stability of the structural incorporation of uranium into the hematite crystal structure suggests the feasibility of iron oxides for inhibiting the mobility of aqueous uranium (VI) [15]. The use of special

stainless steels (i.e., Eurofer steel) for some portions of the main wall of a nuclear fusion experimental reactor may come into consideration in industrial applications of nuclear fusion; therefore, the detailed knowledge and quantification of their interactions between atoms, molecules and plasma, including electron impact ionization cross sections of iron oxide molecules, is of considerable interest [16]. Iron oxides are, furthermore, of great interest with regard to the corrosion and oxidation processes of iron metal and steel, which are mediated by the surface whose structure depends greatly on environmental variables such as temperature, oxygen or water partial pressures [17,18]. Additionally to the various Fe oxidation states, ferric oxide (Fe_2O_3) may be stable or metastable in the known α , β , γ , ε , ζ and δ polymorphs [19–22]. Polymorphism in this case means a possibility for a compound to exist in two or more solid phases that are isochemical but have distinct crystal structures and thus, different physical properties. Due to their different physical properties, which arise from the differences in their crystal structures, all of the polymorphs have found applications in nanotechnology [20]. Moreover, there are also not simply polymorphs of known iron oxides, but distinct compounds with the formula Fe_4O_5 [23]. Other iron oxides with unconventional stoichiometry, such as Fe_5O_6 , Fe_5O_7 , Fe_7O_9 and more complicated compounds have been predicted in theory, some of which have been successfully synthesized at pressures of $10 \sim 80$ GPa and annealed from high temperatures [24]. Magnetite (Fe_3O_4), maghemite ($\gamma\text{-Fe}_2\text{O}_3$) and hematite ($\alpha\text{-Fe}_2\text{O}_3$), including in the form of the oxidized zerovalent iron core-shell structure, are widely used in heterogeneous catalysis processes and have been used as attractive alternatives for the treatment of wastewaters and soils contaminated with organic compounds [25–27].

Structures containing the various iron oxide crystalline or amorphous phases can either be macro- (ceramics [18]), micro- (microbial-induced precipitates [28]) or nanometer-sized (nanoparticles and nanoclusters [29]). The nucleation and growth of inorganic crystals, including iron oxides, from solutions occurs throughout geochemical, biological and synthetic systems [30]. Iron oxide biominerals are formed under “green” conditions without a loss of functionality such that they have the potential for numerous scientific as well as industrial applications [31]. Global iron cycling is driven by both abiotic and biotic reactions, and in the presence of oxygen and under circumneutral pH conditions, ferrous iron is quickly oxidized to Fe(III) and precipitates as iron oxides [32,33].

The physical properties of the various iron oxide compounds can be extremely different, e.g., magnetite and maghemite have been commonly used in biomedicine because of their saturation magnetization being the highest [34]. The ε -polymorph of Fe_2O_3 possesses the highest coercive force (up to 2 T at room temperature [20,35–37]) among the other ferrimagnetic oxides, while maghemite-magnetite nanoparticles (NPs) can have almost zero coercivity [38] with a very low difference in their average size. In some applications, e.g., in catalysts, amorphous iron oxide NPs can be more active than crystalline polymorphs of the same diameter thanks to their “dangling bonds” and higher surface–bulk ratio in their amorphous phase [39]. Based on the literature data, a generalized scheme illustrating the diversity of the known iron oxide compounds, including stable, metastable, atomic clusters and amorphous, is given in Figure 1.

The current review attempts to summarize the main information on the various iron oxide compounds to date. The next section is devoted to a comparison of some of the main physical properties of the various iron oxide compounds.

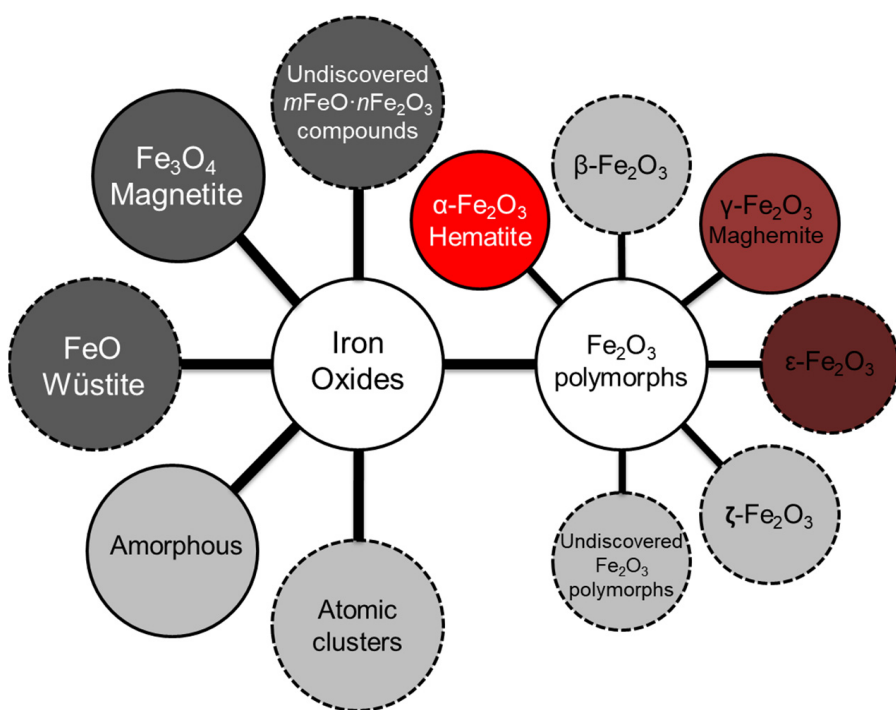


Figure 1. Diversity of stable (solid line) and metastable (dashed line) iron oxides.

2. Physical Properties of Various Iron Oxide Compounds

An Fe–O phase diagram is given in Figure 2. According to the ratio of Fe^{2+} and Fe^{3+} , the phase diagram of Fe–O can be divided into six phase zones from right to left [40].

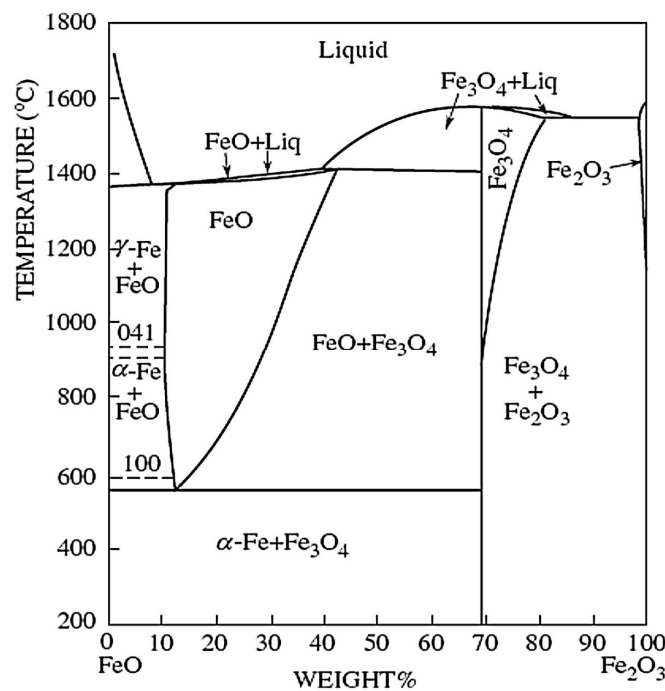


Figure 2. Equilibrium phase diagram for Fe–O system. Reprinted from [40], with permission from Elsevier.

The shown phase diagram does not take into account the polymorphisms of ferric oxides. Sakurai et al. [41] discuss the crystal structures and magnetic properties of the four phases are the following: ferrimagnetic $\gamma\text{-Fe}_2\text{O}_3$ with a spinel structure; ferrimagnetic

ε - Fe_2O_3 with an orthorhombic structure; antiferromagnetic β - Fe_2O_3 with a bixbyite structure; and weak ferromagnetic α - Fe_2O_3 with a corundum structure. The observed phase transformations for Fe_2O_3 phases inside of the mesoporous silica matrix are due to the surface (or interface) energy G_S contribution to the total free energy $G = G_B + (6V_m/d)G_S$, where G_B is the free energy in the bulk, V_m is the molar volume and d is the diameter of the NP. The G vs. d curves should appear as shown in Figure 3.

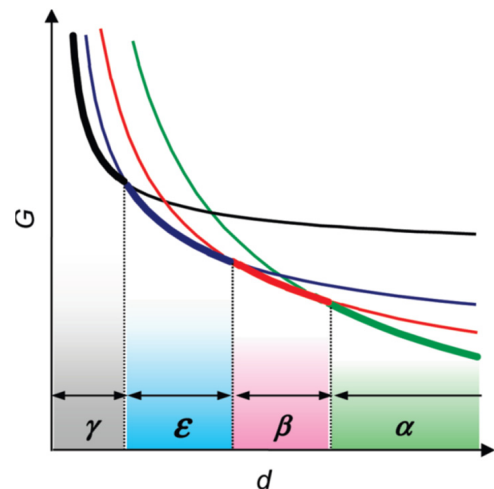


Figure 3. Representation of free energy G vs. particle diameter d curves for the four Fe_2O_3 phases. Gray, blue, green and red lines represent the G values of γ -, ε -, β - and α - Fe_2O_3 , respectively. Thick solid lines indicate the most stable Fe_2O_3 phases over the corresponding size ranges. Copyright 2009 by the American Chemical Society. Reprinted with permission from [41].

Such a strong correlation between the most stable iron oxide crystal phase and the matrix makes it possible to create nanomaterials with diametrically different magnetic properties. Our team has provided the studies on the natural and synthetic silica-based systems containing inclusions of iron oxide NPs. Figure 4 illustrates the static magnetic characteristics of the silica-based systems with NPs of ε - Fe_2O_3 with a coercive force $H_c = 1.07 \text{ T}$ [37], γ - Fe_2O_3 – Fe_3O_4 with $H_c = 0.5 \text{ mT}$ [38] and natural magnetite from the Kovdor deposit with $H_c = 4 \text{ mT}$ [6]. Thus, despite their almost identical chemical composition, the similar structures with iron oxides can possess different H_c values by more than three orders of magnitude.

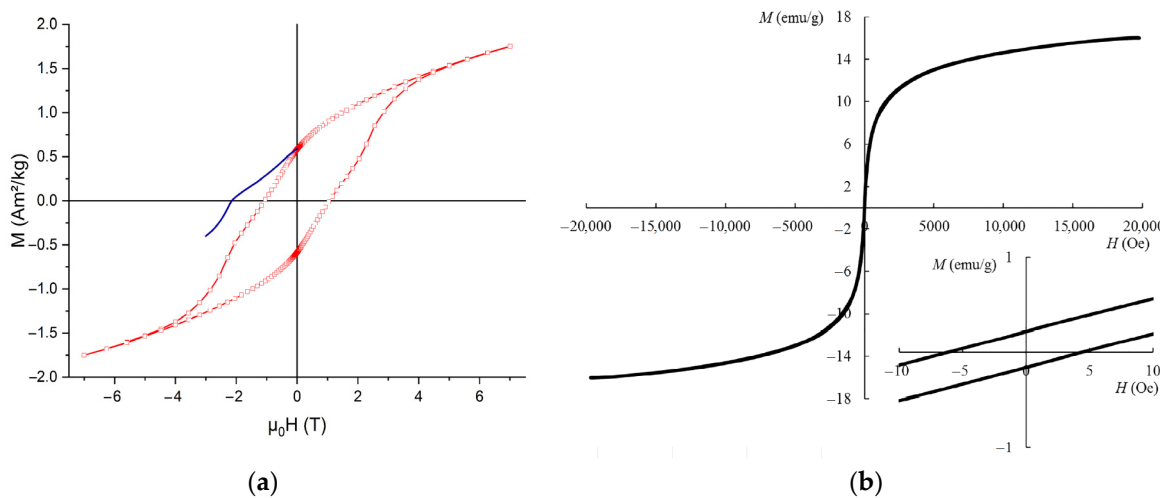


Figure 4. Cont.

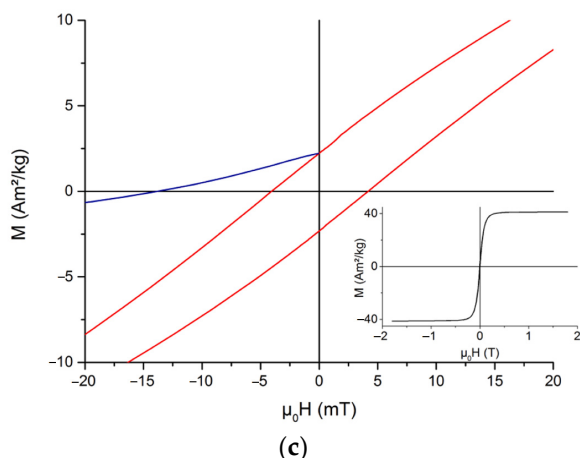


Figure 4. Static magnetic properties of various samples of silica–iron oxide systems: (a)—Hysteresis loop and backfield demagnetization curve of a sample containing $\varepsilon\text{-Fe}_2\text{O}_3$. Reprinted from [37], license CC BY 4.0; (b)—Magnetic hysteresis curve of $\text{Fe}_m\text{O}_n\text{-SiO}_2$ synthetic colloidal nanoparticles. Reprinted from [38], with permission from Elsevier; (c)—Backfield curve and central part of the hysteresis loop of magnetite ore powder; full loop in the 1.8 T maximum field is shown in the inset. Reprinted from [6], with permission from Elsevier.

Iron oxide compounds can differ not only by their coercive force, as shown above, but also by their other physical characteristics. Some of them are shown in Table 1.

Table 1. Comparison of the physical characteristics of various iron oxide compounds [42–73].

Parameter	Iron Oxide Compound					
	FeO	Fe_3O_4	$\alpha\text{-Fe}_2\text{O}_3$	$\beta\text{-Fe}_2\text{O}_3$	$\gamma\text{-Fe}_2\text{O}_3$	$\varepsilon\text{-Fe}_2\text{O}_3$
Mineral name	Wüstite	Magnetite	Hematite	–	Maghemite	–
Crystal structure	Cubic [42]	Cubic spinel [43]	Rhombohedral [44]	Cubic [62]	Cubic spinel [45]	Orthorhombic [46]
Static dielectric permittivity	22.6 [47]	20–40 [48,49]	12–26 [48–50]	n/a	20 [48]	n/a
High-frequency dielectric permittivity	10.8 [47]	7–16 [51]	7.6–7.9 [50]	n/a	14.2 [52]	4–10 [53,54]
Saturation mass magnetization ¹ at 300 K, emu/g	11–18 [55,56]	92–94 [57]	0.3–1.9 [58,59]	0.02–0.05 [63,64]	74–80 [60,61]	15 [46]
Curie/Neel point, K	196 [47,55]	838–856 [66]	948–963 [41,58]	110–119 [62,64]	618–928 [41,67]	480–495 [41,46]
Optical band gap at 300 K, eV	1.0 [47]	0.2 [68,69]	1.9–2.2 [59,70–72]	1.7–1.9 [64,65]	2.0 [60]	2.0–2.4 [73]

¹ The values of saturation mass magnetization are given for the bulk materials.

The crystal structure of an iron oxide compound can be attributed to various symmetry groups: cubic for FeO [42], Fe_3O_4 [43] and $\gamma\text{-Fe}_2\text{O}_3$ [45], rhombohedral for $\alpha\text{-Fe}_2\text{O}_3$ [44], and orthorhombic for $\varepsilon\text{-Fe}_2\text{O}_3$ [46]. Crystal structure variation influences the electron zone structure, which can be semi-metallic with an optical band gap (at 300 K) of 0.2 eV for Fe_3O_4 [68,69] and semiconductive for FeO with an optical band gap of 1.0 eV [46], as well as for α -, γ - and $\varepsilon\text{-Fe}_2\text{O}_3$ with an optical band gap of 1.9–2.4 eV [58,59,70–73]. There is no clear correlation between the crystal structure of an iron oxide compound and its dielectric permittivity, for which values are in the range of 12–40 for static permittivity [46–49] and

4–16 for high-frequency permittivity [46,49–53]. Since the various iron oxides can possess antiferromagnetic or ferrimagnetic properties, their value of saturation mass magnetization can differ by a few orders of magnitude: from 0.3 emu/g (at 300 K) for pure hematite [57,58] to 92–94 emu/g for stoichiometric magnetite [56]. Such variation in electrical and magnetic characteristics lies in the versatility of the structures containing iron oxides for their wide spectrum of possible applications. The next section is devoted to the main mechanisms of iron oxide formation disclosed in the scientific literature.

3. Mechanisms of Iron Oxide Formation

The literature data on the iron oxide formation mechanisms were divided into several groups according to the iron oxide compounds in the studied structures: the structures containing pure crystal iron oxide phases, the ones containing iron oxide atomic clusters and amorphous iron oxides, the ones containing two co-existing iron oxide crystal phases, and the ones containing three or more co-existing iron oxide phases. Their formation mechanism, either natural or synthetic, is briefly described based on the data in the cited reference. Furthermore, their existing and potential (declared) applications are also given.

3.1. The Structures Containing Pure Phases of FeO , Fe_4O_5 , Fe_3O_4 , and α -, β -, γ -, δ -, ε - and ζ -Polymorphs of Fe_2O_3

The information on the structures with a pure iron oxide crystal phase is given separately for each iron oxide compound in Tables 2–6.

Based on the gathered information, it was possible to determine the most frequently obtained form of the structures containing FeO (Table 2). This form is FeO NPs produced for biomedical applications via various chemical or physical routes, but not naturally originated, since this iron oxide compound is metastable under normal conditions [42,74–80].

As one of the stable iron oxide compounds, magnetite can be obtained from the various structures, including natural abiotic or biogenic and synthetic ones (Table 3). Fe_3O_4 NPs can be considered as one of the most frequently used iron oxide magnetic materials and their production techniques are mostly chemical since this approach is most suitable for biomedical applications [81–89]. Additionally, “green” techniques, involving the use of natural plant extracts [90,91], biomimetic formation [92] or microbial mineralization [93–98], are widely used. Other commonly described forms of magnetite are its inclusion within ore samples [6,99–104] widely used in geosciences and the external magnetite layer of metal surfaces [105–109], which is an important object of iron corrosion studies.

The most stable (under normal conditions) iron oxide compound, hematite, attracts the highest attention of scientists, according to the overall amount of published papers (Table 4). Similarly to magnetite, the most frequently obtained form of $\alpha\text{-Fe}_2\text{O}_3$ is a chemically synthesized NP, predominantly used for photocatalysis, biogeochemistry and the bioremediation of toxic compounds [105–119]. The second important form of hematite is the natural ore with inclusions of $\alpha\text{-Fe}_2\text{O}_3$, which is used in Earth sciences [117–124]. The use of the pure $\gamma\text{-Fe}_2\text{O}_3$ is quite rare. The most frequently produced form of $\gamma\text{-Fe}_2\text{O}_3$ is as NPs (Table 5), including chemically synthesized [125–129] or biogenic [93].

Structures with $\beta\text{-Fe}_2\text{O}_3$, $\varepsilon\text{-Fe}_2\text{O}_3$, $\zeta\text{-Fe}_2\text{O}_3$, $\delta\text{-Fe}_2\text{O}_3$ or Fe_4O_5 metastable phases (Table 6) are much less described compared to the main stable compounds of iron oxides. $\varepsilon\text{-Fe}_2\text{O}_3$ is the only one seriously applicable in biomedicine [130,131], electronics [132,133] or geosciences [134,135] and can be obtained both synthetically [37,136,137] or by extraction from various archeological objects [138–140]. There have also been some attempts to use $\beta\text{-Fe}_2\text{O}_3$ NPs in biomedicine [63], sensors and lithium-ion batteries [20,64].

Table 2. Data on the structures containing an FeO phase.

Composition	Main Mechanisms of Iron Oxide Formation	Declared Applications	Phase Verification Techniques	Refs.
FeO NPs	Thermal decomposition of the iron(II) precursor, mechanochemical reduction of magnetite, flame synthesis, laser target interaction in liquid carrier media	Biomedicine, electronics, spintronics, magnetic force microscopy, metastability studies	XRD ¹ , UV-Vis ² , MALDI-TOF MS ³ , EELS ⁴ , F-AAS ⁵ HAADF-STEM ⁶ ,	[41,74–80]
Ultra-thin FeO film	Oxidation of iron monocrystal surface	Iron oxidation kinetics study	RMDS ⁷	[141]
	Electron-beam deposition on Au(111) surface	Iron catalysis, electronics, biomedicine	STM ⁸	[142]
Millimeter-sized iron oxide particles	Magnetite reduction with iron as reducing agent	Catalysts for ammonia synthesis	TG-DSC ⁹	[40]
FeO layer on the metal alloy surface	Invar oxidation in a static carbon dioxide atmosphere	Iron oxidation kinetics study	XRD, TG-DSC, TEM ¹⁰	[143]
Wüstite inclusions in titanomagnetite particles	Titanomagnetite iron sand-fluidized bed reduction by hydrogen	Commercial iron making	XRD	[144]
FeO powder	Reduction of hematite in a gas-controlled electric furnace	Earth's mantle sound velocity studies	XRD, IXS ¹¹	[145]
FeO inclusions in the mold flux	Iron oxide formation in molten mold flux	Study of the oxidation mechanism of mold flux-covered molten iron	XRF ¹²	[146]
FeO inclusions within the dense iron shell	Porous hematite gas reduction under isothermal conditions	Industrial exploitation of low-grade iron ores	TG-DSC, XRD	[147]
FeO clusters within the stable iron oxide matrix	The reduction of magnetite/hematite at temperatures of 400~500 °C	Iron catalysis	Quantitative theoretical analysis	[148]

¹ X-ray powder diffraction. ² UV-visible(-NIR) spectroscopy. ³ Matrix-assisted laser desorption ionization time-of-flight mass spectrometry. ⁴ Electron energy loss spectroscopy.⁵ Flame atomic absorption spectroscopy. ⁶ High-angle annular dark-field scanning transmission electron microscopy. ⁷ Reactive molecular dynamics simulations. ⁸ Scanning tunneling microscopy. ⁹ Thermogravimetry/differential scanning calorimetry. ¹⁰ Transmission electron microscopy. ¹¹ Inelastic X-ray scattering. ¹² X-ray fluorescence.

Table 3. Data on the structures containing an Fe_3O_4 phase.

Composition	Main Mechanisms of Iron Oxide Formation	Declared Applications	Phase Verification Techniques	Refs.
Fe_3O_4 NPs	Co-precipitation from iron salt solution, co-precipitation from iron oxyhydroxide solution, solvothermal synthesis, electrochemical formation from a pure iron, thermal decomposition of the iron oleate complex, biomimetic process with use of a leaf extract, nucleation mediated by iron-binding protein Mms6, biogeneration with a use of amyloid peptide A β 42	Biomedicine, magnetic separation, antimicrobial and antioxidant applications, contaminant removal, black pigment production, ferrofluids	TEM, XRD, SAXS ¹ , RS ² , FTIR ³ , XPS ⁴ , HAADF-STEM, EELS, TG-DSC, UV-Vis, PL ⁵ , MSP ⁶ , SAED ⁷	[81–91,149–162]
Bacterial magnetosomes	Bacterial biomineralization, transient phosphate-rich ferric hydroxide reduction to magnetite, formation by dissimilatory iron-reducing bacteria	Biomedicine, paleomagnetism, microbial iron cycle studies, bioremediation of toxic compounds	HAADF-STEM, TEM, XAS ⁸ , SAED, XMCD ⁹	[93–98,163]
Inclusions of Fe_3O_4 within ore samples	Abiotic hydrothermal mineralization, iron oxide formation derived from continental weathering, extrusive magmatic formation from iron oxide-melt liquid	Geochemistry, environmental magnetism studies, early Earth iron cycle studies, origin and evolution of iron oxides studies	XRD, RS, XPS, EDS ¹⁰ , ICP-AES ¹¹	[99–102]
External magnetite layer on a metal surface	Oxidation of a steel surface, slow oxidation of green rusts at room temperature, high-temperature corrosion	Corrosion studies	XRD, EDS, XRF, RS, XPS, AES ¹²	[105–110]
Fe_3O_4 microparticles	Microbial-induced precipitation with the use of <i>Sporosarcina pasteurii</i>	Green synthesis of magnetite	EDS	[28]
	Aging of ferrous hydroxide gels at elevated temperatures	Colloidal crud formation studies	XRD, TEM	[162]

Table 3. *Cont.*

Composition	Main Mechanisms of Iron Oxide Formation	Declared Applications	Phase Verification Techniques	Refs.
Self-assembled Fe ₃ O ₄ mesocrystalline films	Heat-up method with the use of iron(III) chloride and sodium oleate	Biomedicine and industrial applications	TEM, SAED, XAS, SAXS	[163]
Fe ⁰ /Fe ₃ O ₄ composite	Controlled reduction of the starting Fe ₃ O ₄ with H ₂	Treatment of wastewater	MSP, XRD	[164]
Magnetite nanowires	Supercritical fluid inclusion within a mesoporous silica matrix	Soft magnetic materials	TEM, SAED, XRD, FTIR	[165]
Inclusions of Fe ₃ O ₄ NPs	Bacterial reduction of amorphous hydrous ferric oxide	Biogeochemistry	TEM, SAED, XRD, EDS	[166]
Fe ₃ O ₄ layer on the zerovalent iron surface	Surface oxidation of iron by oxygen in an aqueous medium	Organic pollutant removal	EDS, XRD	[167]
Epoxy/magnetite nanocomposites	Reduction of anhydrous ferric chloride by ammonium hydroxide	Marine coatings of steel	FTIR, XRD, TEM	[168]
Iron oxide nanocomposite hydrogel	Co-precipitation process by ammonium hydroxide	Biomedicine	XRD, TEM, TG-DSC, EDS	[169]
Surface film containing Fe ₃ O ₄ NPs	Bacterial mineralization in the air–water interface in Arctic tundra waters	Anaerobic microbial carbon cycle	TEM, EDS, STEM, EELS, FTIR, RS	[170]
Nanocomposite hydrogel with Fe ₃ O ₄ NPs	Reduction with ammonia from a remixed solution of FeCl ₃ and FeCl ₂	Biomedicine	TEM, XRF, EDS, TG-DSC, FTIR	[171]
Biochar composite with Fe ₃ O ₄ NPs	One-pot solvothermal method using phoenix tree leaf-derived biochar	Treatment of wastewater	TEM, XRD, FTIR, XPS, ICP-AES	[172]
Fe ₃ O ₄ NP inclusions in the surface layer	Formation of NPs along with cracks and pores during pre-oxidation	Plasma nitriding of steel	XRD	[173]
Chitosan/graphene oxide composite with Fe ₃ O ₄	Co-precipitation of Fe ₃ O ₄ and chitosan/graphene oxide	Organic pollutant removal	XRD, XPS, RS, FTIR	[174]
Fe ₃ O ₄ layer on carbon fibers of a carbon paper	Deposition on the carbon paper gas diffusion layer at the cathode	Corrosion studies	XRD, EDS	[175]

Table 3. *Cont.*

Composition	Main Mechanisms of Iron Oxide Formation	Declared Applications	Phase Verification Techniques	Refs.
Mesocrystals assembled from Fe_3O_4 nanocubes	Heat-up method with the use of iron(III) chloride and sodium oleate	Mesocrystal applications	TEM	[176]
Fe ₃ O ₄ nanorods	Formation in electron-beam-induced deposition from iron pentacarbonyl	Electronics	TEM, EELS	[177]
Lipase immobilized on coated Fe ₃ O ₄ NPs	Solvothermal method with the use of $\text{FeCl}_3 \cdot 6\text{H}_2\text{O}$ and ethylene glycol	Biodiesel production	TEM, XRD, FTIR	[178]
Spherical mesoporous magnetite aggregates	Precipitation from iron(III) ethoxide with ethanol in the surfactant solution	Catalysis, sustainability	FTIR, XPS, EDS, TEM, MSP	[179]
Perfluorocarbon-loaded hydrogel microcapsules	Coaxial interface shearing double emulsion method	Biomedicine	–	[180]
Mesoporous magnetite	Ball milling of Fe ₃ O ₄ and SiO ₂ followed by partial reduction	Recyclable absorbent for toxic Cr(VI) ions	TEM, XRD, XPS, ICP-AES	[181]
Magnetite crystal model	Local spin-density approximation density-functional calculation	Magnetite electron structure studies	Density-functional calculations	[43]
Spherulite nanostructure with inclusions of Fe ₃ O ₄	Electron-beam irradiation of the precursor solution with iron nitrate	Crystal growth dynamics studies	TEM, STEM, EDS	[182]

¹ Small-angle X-ray scattering. ² Raman spectroscopy. ³ Fourier-transform infrared spectroscopy. ⁴ X-ray photoelectron spectroscopy. ⁵ Photoluminescence spectroscopy. ⁶ Mössbauer spectroscopy. ⁷ Selected area electron diffraction. ⁸ X-ray absorption spectroscopy. ⁹ X-ray magnetic circular dichroism. ¹⁰ Energy-dispersive X-ray spectroscopy. ¹¹ Inductively coupled plasma atomic (optical) emission spectroscopy. ¹² Auger electron spectroscopy.

Table 4. Data on the structures containing an $\alpha\text{-Fe}_2\text{O}_3$ phase.

Composition	Main Mechanisms of Iron Oxide Formation	Declared Applications	Phase Verification Techniques	Refs.
$\alpha\text{-Fe}_2\text{O}_3$ NPs	Hydrothermal synthesis, precipitation from a ferric salt solution using a natural leaf extract, precipitation and aging of ferrihydrite in an oxidized system, direct transformation of $\alpha\text{-FeOOH}$ via high-energy ball milling	Biomedicine, bioremediation of toxic compounds, photocatalysis, geochemistry, electronics, antibacterial activity studies, geochemistry	XRD, FTIR, UV-Vis, EDS, TEM, RS, XPS, XAS, ICP-AES, EPR ¹ , HAADF-STEM, WAXS ²	[105–111,180–192]
Inclusions of $\alpha\text{-Fe}_2\text{O}_3$ in ore samples	Precipitation from oxygenated iron-rich water or biomineralization, dissolution of Fe(III) hydroxides by Fe(III)-reducing bacteria, terrestrial subglacial oxidation of glacial iron fluvial deposition	Terrestrial iron oxide concretion studies, Precambrian iron formation studies, Antarctic glacier studies, biogeochemistry	EDS, RS, TEM, HAADF-STEM, XRD, SAED, FTIR, UV-Vis	[112–119]
$\alpha\text{-Fe}_2\text{O}_3$ layer on a metal surface	Anodic potentiostatic oxidation of stainless steel sheet	Anodic passivation of stainless steel	AES	[193]
	Oxidation of steel in an $\text{O}_2\text{-N}_2$ atmosphere at high temperature	Improvement of steel coating quality	TEM, EDS, GD-OES ³	[194]
	Corrosion of chromia-forming alloys in simplified combustion atmosphere	Fireside corrosion studies	EDS, XRD	[195]
Porous $\alpha\text{-Fe}_2\text{O}_3$ nanostructures	Hydrothermal synthesis from $\text{FeCl}_3\cdot6\text{H}_2\text{O}$ in a microwave reactor	Lithium-ion batteries	XRD, TEM, SAED, XPS, TG-DTG	[196]
	Sol-gel transformations of precursors in self-organized nanocellulose	Energy conversion and storage	XRD, TEM, SAED, XPS, TG-DSC	[197]
Martian hematite deposits	Precipitation from oxygenated iron-rich water or biomineralization	Search for evidence of life on Mars	EDS, TEM	[198]
Hematite layers on sandstone grains	Precipitation from oxidizing iron-saturated fluid	Geochemistry	XRD, ICP-MS ⁴	[199]
Double-walled hematite nanotubes	Growth of Fe nanowires inside porous templates and oxidation	Photocatalysis, biomedicine	XRD, EELS, HAADF-STEM, RS	[200]

Table 4. *Cont.*

Composition	Main Mechanisms of Iron Oxide Formation	Declared Applications	Phase Verification Techniques	Refs.
Coral-like and nanowire $\alpha\text{-Fe}_2\text{O}_3$	Thermal oxidation of iron foils in air- and water vapor-assisted conditions	Removal of Cr ions from aqueous systems	XRD, RS, TEM, XPS	[201]
$\alpha\text{-Fe}_2\text{O}_3$ NPs on mineral surfaces	Weathering of Fe-bearing silicate minerals or partial oxidation of Fe_3O_4	Paleoclimate studies	XRD, TEM, SAED	[202]
$\alpha\text{-Fe}_2\text{O}_3$ nanorods	Controlled aqueous growth from $\text{FeCl}_3\cdot 6\text{H}_2\text{O}$ and NaNO_3	Photoelectrochemical water splitting	XRD	[203]
Inclusions of $\alpha\text{-Fe}_2\text{O}_3$ in regolith simulant	Ball milling of commercial $\alpha\text{-Fe}_2\text{O}_3$ samples in isopropyl alcohol	Combustion studies	XRD, TG-DSC	[204]
Inclusions of $\alpha\text{-Fe}_2\text{O}_3$ in stone matrix	Bacterial mineralization	Heritage sciences	XRD, EDS, RS	[205]
Inclusions of $\alpha\text{-Fe}_2\text{O}_3$ in auriferous quartz	Terrigenous abiotic mineralization	Geochemistry	EDS	[206]
Hematite layers on sandstone grains	Terrigenous co-precipitation with sandstone and uranium	Geochemistry of radionuclides	Gamma-ray spectrometry, ICP-MS	[207]
Hematite inclusions encapsulated in chert	Dehydration of the interstitial goethite to hematite microplates	Geochemistry	TEM, XRD, EDS	[208]
Hollow $\alpha\text{-Fe}_2\text{O}_3$ nanofibers	Electrospinning with a use of iron chloride and poly(vinylpyrrolidone)	Photoelectrochemical water splitting	EDS, TEM, SAED, TG-DSC, UV-Vis	[209]
Fossilized bacteria with $\alpha\text{-Fe}_2\text{O}_3$	Biomineralization by anoxygenic photoferrotrophy	Biogeochemistry	RS	[210]
Porous $\alpha\text{-Fe}_2\text{O}_3$ xerogel and aerogel	Sol-gel synthesis from Fe(III) salts with addition of propylene oxide	Catalysis, sensors, biology	TEM	[211]
Iron oxide nanostructures	Microbial Fe(II) oxidation of carbonate green rust by Fe(II)-oxidizing bacteria	Precambrian iron formation studies	MSP	[212]
Iron oxide biogenic precipitates	Bacterial mineralization	Biogenic iron oxide formation studies	XAS	[213]

Table 4. *Cont.*

Composition	Main Mechanisms of Iron Oxide Formation	Declared Applications	Phase Verification Techniques	Refs.
Steel-wearing ejected debris with $\alpha\text{-Fe}_2\text{O}_3$	Steel fretting wear controlled by oxygen ingress to the contact	Steel fretting wear studies	XRD	[214]
$\alpha\text{-Fe}_2\text{O}_3$ NPs on a steel surface	Oxidation of iron-bonded diamond precision-polishing wheel	Grinding of hard and brittle materials	XRD, XPS, TEM	[215]
Nanostructured $\alpha\text{-Fe}_2\text{O}_3$ films	Electrochemical anodization of steel in an alkaline solution	Photocatalysis, anti-bioadhesion	RS, UV-Vis	[216]
Monodispersed micaceous $\alpha\text{-Fe}_2\text{O}_3$	Hydrothermal synthesis from iron chromium hydroxide precursors	Iron chromium grinding waste recycling	ICP-AES, XRD, XPS	[217]
Nanoporous $\alpha\text{-Fe}_2\text{O}_3$ layer on an iron foil	Anodization of iron in an ethylene glycol and NH_4F aqueous solution	Photocatalysis	TEM, RS, XRD, UV-Vis, EDS, EELS	[218]
Natural $\alpha\text{-Fe}_2\text{O}_3$ from the iron deposits	Terrigenous abiotic mineralization	Photocatalytic recycling of toxic wastewater	RS, EDS, UV-Vis	[219]
Nanocomposite containing $\alpha\text{-Fe}_2\text{O}_3$	Wet impregnation of Co_3O_4 powder with an $\text{Fe}(\text{NO}_3)_3\cdot 9\text{H}_2\text{O}$ solution	Catalysis	XPS, XRD, TG-DSC, EDS, TEM	[220]
Stepped $\alpha\text{-Fe}_2\text{O}_3$ (0001) surfaces	First principles spin-polarized density-functional theory simulation	Chloride-induced iron depassivation studies	Density-functional theory calculations	[221]
$\alpha\text{-Fe}_2\text{O}_3$ powder	In situ generation of iron oxide via decomposition of $\text{Fe}(\text{NO}_3)_3\cdot 9\text{H}_2\text{O}$	Catalysis	XRD	[222]
$\alpha\text{-Fe}_2\text{O}_3$ nanorods	Hydrothermal precipitation and air calcination of goethite nanorods	Catalysis, lithium-ion batteries, sensors	XRD, MSP, UV-Vis, EDS, TG-DSC	[223]
$\alpha\text{-Fe}_2\text{O}_3$ nano- and microparticles	Chemically synthesized commercial $\alpha\text{-Fe}_2\text{O}_3$ samples	Mechanisms of oxide toxicity toward bacteria	FTIR, XAS	[224]
$\alpha\text{-Fe}_2\text{O}_3$ nanowires	Heating of iron wires suspended between two electric contacts	Vacuum electronic devices	TEM, EDS, XPS, RS	[225]
$\alpha\text{-Fe}_2\text{O}_3$ layer on zerovalent iron NPs	Iron oxide film formation under aerobic conditions	Remediation of water pollutants	TEM, FTIR, XPS, XRD	[226]
Inclusions of $\alpha\text{-Fe}_2\text{O}_3$ in rock varnish	Terrigenous abiotic mineralization or biotic processes	Geomicrobiology	XRD, RS, EDS	[227]

Table 4. *Cont.*

Composition	Main Mechanisms of Iron Oxide Formation	Declared Applications	Phase Verification Techniques	Refs.
Nanolayers of $\alpha\text{-Fe}_2\text{O}_3$ in polymer composite	Iron pentacarbonyl transformation with diamond anvil cells in Ar gas	High-energy density solid studies	RS, TEM, XRD	[228]
Jian ware blue-colored glaze with $\alpha\text{-Fe}_2\text{O}_3$	Calcination of a milled mix at a high temperature in oxidizing atmosphere	Ancient ceramics studies	XRD, UV-Vis, TEM, XPS	[229]
Inclusions of $\alpha\text{-Fe}_2\text{O}_3$ in sediment samples	Microbial reduction of surface Fe(III) by iron-reducing bacteria	Microbial iron reduction studies	XRD	[230]
Core-shell iron/iron oxide NPs	Zerovalent Fe core-controlled oxidation during deposition	Oxide formation under e-beam radiation studies	TEM, EELS	[231]
$\alpha\text{-Fe}_2\text{O}_3$ film on a dielectric substrate	Liquid-phase atomic layer deposition of crystalline hematite	Catalysis, sensors, lithium-ion batteries	XRD, UV-Vis	[232]
Cube-shaped $\alpha\text{-Fe}_2\text{O}_3$ microstructures	Facile hydrothermal method using hydrated ferric nitrate and NaOH	Ethanol gas sensing	XRD, FTIR, EDS, RS	[233]
Iron oxide/Ti composites	Plasma electrolytic oxidation, impregnation and annealing	Phenol photodegradation	XRD, EDS, FTIR, XPS	[234]
Microporous $\alpha\text{-Fe}_2\text{O}_3$ NPs	Precipitation from iron(II) sulfate using a natural leaf extract	Sustainability	XRD, UV-Vis, XPS, FTIR	[235]
Inclusions of $\alpha\text{-Fe}_2\text{O}_3$ in artificial clay	Fe(OH) ₃ colloid mixing into chemically pure kaolin	Laterite engineering	XRD	[236]
Iron oxide nanotubes	Potentiostatic anodization of iron foil in electrolytes containing NH ₄ F	Catalysis, sensors, supercapacitors	XRD, TEM, SAED	[237]
$\alpha\text{-Fe}_2\text{O}_3$ thin film	Spray pyrolysis from FeCl ₃ and methanol solution	Electrochemical supercapacitors	XRD, UV-Vis	[44]
Corroded steel tube samples with $\alpha\text{-Fe}_2\text{O}_3$	Steel corrosion in an aqueous medium with oxygen and chlorine	Pipeline corrosion assessment	XRD, EDS, TEM, SAED	[238]
Inclusions of $\alpha\text{-Fe}_2\text{O}_3$ in stone samples	Formation by washing and leaching of a stone object by rainwater	Limestone artifact studies	RS, FTIR, EDS, XRF	[239]
Iron oxide-loaded slag	Precipitation from FeCl ₃ solution with NaOH into melted slag	Arsenic removal from water	ICP-AES, XRD	[240]

Table 4. *Cont.*

Composition	Main Mechanisms of Iron Oxide Formation	Declared Applications	Phase Verification Techniques	Refs.
3D-ordered macroporous $\alpha\text{-Fe}_2\text{O}_3$	Impregnation of polymer matrices and high-temperature calcination	Catalysis	XRD, TG-DSC, FTIR, SAED, UV-Vis, XPS	[241]
$\alpha\text{-Fe}_2\text{O}_3$ /mesoporous silica core-shell NPs	Solvothermal synthesis from ferric nitrate with sol-gel silica coating	Catalysis, biomedicine	XRD, TEM, FTIR, UV-Vis	[242]
Spindle-shaped $\alpha\text{-Fe}_2\text{O}_3$ mesocrystal	Interface-driven nucleation by ferrihydrate oxidation and attachment	Thermoelectronics, photonics, catalysis, photovoltaics	TEM, SAED, FTIR, EDS	[243]
Hematite nanopillars	Electron-beam evaporation using anodized aluminum oxide templates with well-defined pore diameters	Photoelectrochemical water splitting	XRD, XPS, UV-Vis	[244]

¹ Electron paramagnetic resonance spectroscopy. ² Wide-angle X-ray scattering. ³ Glow-discharge optical emission spectrometry. ⁴ Inductively coupled plasma mass spectrometry.

Table 5. Data on the structures containing a $\gamma\text{-Fe}_2\text{O}_3$ phase.

Composition	Main Mechanisms of Iron Oxide Formation	Declared Applications	Phase Verification Techniques	Refs.
$\gamma\text{-Fe}_2\text{O}_3$ NPs	Solvothermal synthesis from iron salts, bacterial mineralization, lepidocrocite calcination in an air atmosphere, hydrothermal and solvothermal synthesis from salt solutions	Catalysis, biomedicine, nucleation and formation of biogenic iron oxide studies, electronics, maghemite to hematite transition studies, sensors	TEM, EDS, SAED, XRD, XPS, EPR, FTIR, UV-Vis, ICP-AES, HAADF-STEM, MSP, in situ total scattering, XAS, SAXS, RS	[93,125–129]
$\gamma\text{-Fe}_2\text{O}_3$ NPs in silica matrix	Gas-phase synthesis in a furnace aerosol reactor from iron pentacarbonyl	Biomedicine	XRD, TEM, EDS, FTIR, UV-Vis	[245]
	Dehydration of iron(III) hydroxide to magnetite followed by oxidation	Catalysis	XRD, FTIR	[246]
$\gamma\text{-Fe}_2\text{O}_3$ powder	Chemically synthesized commercial $\gamma\text{-Fe}_2\text{O}_3$ samples	Catalytic oxidation of S(IV)	ICP-MS, FTIR	[247]
26-faceted maghemite polyhedrons	Direct burning of ferrocene in different solvents in an alcohol lamp	Lithium-ion batteries	XRD, TEM	[248]
Magnetic polymeric NPs with $\gamma\text{-Fe}_2\text{O}_3$	Co-precipitation of $\text{FeCl}_3/\text{FeCl}_2 \cdot 4\text{H}_2\text{O}$ with NH_4OH solution	Biomedicine	TEM, TG-DSC, FTIR	[249]
$\gamma\text{-Fe}_2\text{O}_3$ NP superlattice thin films	Chemically synthesized commercial $\gamma\text{-Fe}_2\text{O}_3$ samples	Electronics, optical coatings	Grazing incidence small angle X-ray scattering	[250]
Maghemite-decorated graphene nanoscrolls	Hydrolysis of $\text{FeCl}_3 \cdot 6\text{H}_2\text{O}$ and $\text{W}(\text{CO})_6$, promoted with hydrazine	Energy storage	TEM, XPS, TG-DSC, RS	[251]
Hollow iron oxide NPs	Gas-phase vaporization synthesis of Fe NPs and oxidation to $\gamma\text{-Fe}_2\text{O}_3$	Optics, nanoelectronics	TEM, HAADF-STEM, EDS	[252]
Mesoporous iron oxide	Inverse micelle synthesis from $\text{Fe}(\text{NO}_3)_3 \cdot 9\text{H}_2\text{O}$ butanol solution	Arsenic removal from water	XRD, FTIR, RS, XPS	[253]

Table 6. Data on the structures containing a β -Fe₂O₃, ε -Fe₂O₃, ζ -Fe₂O₃, δ -Fe₂O₃ or Fe₄O₅ metastable phase.

Composition	Main Mechanisms of Iron Oxide Formation	Declared Applications	Phase Verification Techniques	Refs.
Pristine and co-substituted ε -Fe ₂ O ₃	Simulated crystal structure with a use of density-functional calculations	Magnetoelectric material development	Density-functional theory calculations	[254]
ε -Fe ₂ O ₃ embedded in biomimetic graphene	Precipitation from ferric and ferrous chloride with a biocompatible polymer	Biomedicine	XRD, TEM, SAED, RS, XPS, TG-DSC, FTIR	[130]
Epitaxially stabilized thin-film ε -Fe ₂ O ₃	Epitaxy on (100)-oriented yttrium-stabilized zirconia substrates	Electronics, permanent magnets, biomedicine	XRD, HAADF-STEM	[136]
ε -Fe ₂ O ₃ in ancient black glazed wares	Surface iron enrichment and a firing of wares under reducing conditions	Electronics, spintronics	XRF, XAS, XRD, RS, TEM, EDS	[132]
ε -Fe ₂ O ₃ NPs	Hydrolysis of tetraethoxysilane in a solution of ferric nitrate and annealing	Wireless technologies, electronics	XRD, TEM, THz-TDS ¹	[255]
ε -Fe ₂ O ₃ inclusions in fired clay samples	Stabilization of ε -Fe ₂ O ₃ NPs in a matrix of silicates during firing of clays	Paleomagnetism	XRD, EDS	[134]
Y ₃ Fe ₅ O ₁₂ matrix including ε -Fe ₂ O ₃	Formation of ε -Fe ₂ O ₃ in the Y ₃ Fe ₅ O ₁₂ matrix using the sol-gel method	Magnetoelectric material development	XRD, XPS, TG-DSC, FTIR	[256]
δ -Fe ₂ O ₃ in layered double hydroxyl	Dry impregnation of layered double hydroxyl structure with ferric nitrate	Photocatalysis	XRD, FTIR, XRF, TG-DSC, UV-Vis	[22]
ε -Fe ₂ O ₃ -SiO ₂	Reverse micelle method with the use of ferric nitrate	Oxidative dehydrogenation of n-butene	XRD	[136]
β -Fe ₂ O ₃	Milling of Fe ₂ (SO ₄) ₃ and NaCl and calcination at 550 °C in air			
Ga-substituted ε -Fe ₂ O ₃ NPs	Calcination of a mesoporous silica impregnated with metal nitrates	Biomedicine	XRD, XRF, TEM, ICP-MS	[131]

Table 6. *Cont.*

Composition	Main Mechanisms of Iron Oxide Formation	Declared Applications	Phase Verification Techniques	Refs.
$\epsilon\text{-Fe}_2\text{O}_3$ in archeological brick and baked clay	High-temperature firing of bricks and clays in air		RS	[138]
$\epsilon\text{-Fe}_2\text{O}_3$ in archeological samples, $\epsilon\text{-Fe}_2\text{O}_3$ NPs	Sol-gel synthesis from ferric and barium nitrate with tetraethyl orthosilicate	Archaeomagnetism, paleomagnetism	XRD, RS	[135]
$\epsilon\text{-Fe}_2\text{O}_3$ coatings on Si(100) substrates	One-pot sol-gel recipe assisted by glycerol in an acid medium	Paleomagnetism, biomedicine, electronics	RS, XAS, EELS, HAADF-STEM	[257]
$\epsilon\text{-Fe}_2\text{O}_3/\text{SiO}_2$ composite powder	Sol-gel synthesis from ferric and barium nitrate with tetraethyl orthosilicate	Electronics	XRD, TEM	[133]
$\epsilon\text{-Fe}_2\text{O}_3$ nanorods	Chemical vapor deposition from the Fe organic liquid source	Photocatalysis, electronics	XPS	[258]
$\epsilon\text{-Fe}_2\text{O}_3/\text{SiO}_2$ composite	Sol-gel synthesis from nitrate with tetraethyl orthosilicate and nitric acid	Electronics, spintronics, magnetizable printing	TG-DSC, XRD, TEM	[259]
$\epsilon\text{-Fe}_2\text{O}_3$ NPs	Immersion of mesoporous silica with an FeSO_4 or $\text{Fe}(\text{C}_{10}\text{H}_9\text{CHO})$ solution and high-temperature calcination	High-coercivity material development	TEM, XRD, MSP, TEM, SAED	[20,41]
$\beta\text{-Fe}_2\text{O}_3$ NPs		Sensors, lithium-ion batteries		
Epitaxial $\epsilon\text{-Fe}_2\text{O}_3$ films on GaN substrate	Pulsed laser deposition on the Ga-terminated surface of the GaN (0001)	Electronics	XRD, RHEED ² , TEM, XAS, XMCD	[260]
Silica-coated $\epsilon\text{-Fe}_2\text{O}_3$ NPs	Sol-gel treatment of $\beta\text{-FeOOH}$ nanorods with tetraethoxysilane and calcination	Electronics	XRD, TEM, EDS, MSP	[261]
$\epsilon\text{-Fe}_2\text{O}_3$ in a Hare's Fur Jian ware	High-temperature firing of local iron-rich area on the ceramic glaze	Magnetoresistance materials	XRF, XAS, EDS, XRD, RS	[140]
Metal-substituted $\epsilon\text{-Fe}_2\text{O}_3$	Impregnation of mesoporous silica NPs with rhodium-substituted $\epsilon\text{-Fe}_2\text{O}_3$	Electronics, magnetic force microscopy, biomedicine	XRD	[262]

Table 6. Cont.

Composition	Main Mechanisms of Iron Oxide Formation	Declared Applications	Phase Verification Techniques	Refs.
$\beta\text{-Fe}_2\text{O}_3$ NPs	Thermally-induced solid-state reaction of NaCl with $\text{Fe}_2(\text{SO}_4)_3$ in air	Sensors, lithium-ion batteries	XRD, MSP, TEM, SAED	[20]
$\zeta\text{-Fe}_2\text{O}_3$	Pressure treatment of $\beta\text{-Fe}_2\text{O}_3$ NPs at pressures above 30 GPa	n/a		
$\varepsilon\text{-Fe}_2\text{O}_3$ in a thin MgO(111) layer	Pulsed laser deposition from MgO and Fe_2O_3 targets ablated using a KrF laser	Electronics	RHEED, XRD, neutron reflectometry	[263]
Single crystal of Fe_4O_5	Synthesis in the diamond anvil cell at high pressure after laser heating	Solid Earth studies	Density-functional theory calculations	[23]
Nanometer-scale lamellae of Fe_4O_5	High-pressure and high-temperature multi-anvil synthesis	Deep Earth studies	XRD, TEM, SAED, EDS, STEM	[264]
Powder of Fe_4O_5	High-pressure and high-temperature direct synthesis from a mixture of Fe_3O_4 and Fe	Electronics	XRD, neutron diffraction	[265]
$\beta\text{-Fe}_2\text{O}_3$ NPs	Thermally-induced solid-state reaction of NaCl with $\text{Fe}_2(\text{SO}_4)_3$ in air	Optoelectronics, sensors, lithium-ion batteries	XRD, MSP, TEM	[64]
	Hydrolysis of 2M FeCl_3 in boiling water and cooling down slowly at room temperature	Biomedicine	UV-Vis, TEM, XRD, FTIR, EDS, SAED	[63]

¹ Terahertz time-domain spectroscopy. ² Reflection high-energy electron diffraction.

3.2. The Structures Containing Iron Oxide Atomic Clusters and an Amorphous Iron Oxide Phase

In their thermodynamic equilibrium state under normal conditions, iron oxides possess a crystal structure; therefore, there are only a few papers describing compositions with amorphous or poorly crystalline iron oxides, which are obtained via chemical [266–269] or biominerization routes [270] and intended for various potential applications (Table 7). Iron oxide atomic clusters are a more frequently studied object and can be obtained either by synthetic chemical [271–274], physical [275] or biomimetic [276,277] techniques. Potential applications for iron oxide clusters include biomedicine [271,273], electronics [271,276], catalysis [273,274], and natural iron storage process studies [276].

The next type of iron oxide structure is ultra-thin, including two-dimensional films on metal surfaces [142,278–280], which are obtained using various chemical and physical techniques and can be applied to the production of molecular hydrogen [278], removal of contaminants [279], catalysis [142] and electronics [280]. Simulated iron oxide atomic clusters [281] and ultra-thin layers on a metal surface [282] are also described and can be useful for the prediction of the magnetic properties of FeO_x NPs [281] and chemical water treatment technique development [282].

3.3. The Structures Containing Two Co-Existing Iron Oxide Crystal Phases

Real structures containing iron oxides in various cases are inhomogeneous, for example, due to the partial oxidation of magnetite to maghemite for synthetic [38,283–293], natural abiotic [6] and biogenic [294] origins. In this section, compositions with iron oxides containing two co-existing crystal phases are described (Tables 8–11).

Crystal phases of $\alpha\text{-Fe}_2\text{O}_3$ and $\gamma\text{-Fe}_2\text{O}_3$ quite rarely co-exist (Table 8), in comparison, for example, with the phases of magnetite and maghemite, according to the analyzed research articles. Nevertheless, such a combination can be found in natural and synthetic objects, including oxidized iron items [295], $\alpha/\gamma\text{-Fe}_2\text{O}_3$ isolement synthetic heterostructures with different crystal content [296], loess and paleosol [297] and saprolite soils [298] samples, graphene–iron oxide nanotube composites [299] and polyacrylonitrile/iron oxide composites [300]. The main applications of such structures are in the removal of contaminants [299–301], pedogenic process studies [297,298] and corrosion studies [302].

A more frequently discovered combination is the co-existence of $\alpha\text{-Fe}_2\text{O}_3$ and Fe_3O_4 crystal phases (Table 9). They can be found in natural ore samples and can be explained by abiotic [303–308] or biogenic [309–311] processes. Besides these natural formations, such combinations of iron oxide phases can be synthetically obtained with the use of chemical [312–314], physical [315] or biomimetic [316] techniques. The main applications of the compositions are geosciences [306,307,310,311], biomedicine [312,314,317] and catalysis [313,316,317].

Cubic iron oxides, wüstite and magnetite can be co-existing (Table 10), despite these cases being rare, in comparison to the structures containing co-existing $\alpha\text{-Fe}_2\text{O}_3$ and Fe_3O_4 phases [303–328], and can be attributed to applications of iron oxides in Earth's mantle studies [329], porous iron growth mechanism studies [330], environmental remediation, electronics, catalysis, biomedicine and energy storage [331].

Structures containing iron oxides with a spinel structure, magnetite and maghemite, are widely used in various applications with a predominance of NPs intended for biomedicine [45,332–337] (Table 11). It is possible to propose the partial oxidation of magnetite NPs to maghemite in the vast majority of cases (except those with inert atmospheric preservation), but this effect can be distinguished only by the use of some additional instruments, including Mössbauer spectroscopy [6], zero-field and field cooling measurements to reveal a Verwey transition and high-resolution transmission electron microscopy [295] to show the crystal structure, while more widely used X-ray powder diffraction cannot resolve magnetite and maghemite [38]. The most frequently used synthetic routes used to obtain $\gamma\text{-Fe}_2\text{O}_3\text{-Fe}_3\text{O}_4$ NPs are by thermal decomposition [337–340] and chemical precipitation [332,336,341,342].

The iron oxide layer on metal surfaces is also a possible structure containing co-existing magnetite and maghemite phases. Such structures can originate from both natural [343,344] and synthetic [345–349] routes, generally implying chemical or electrochemical oxidation in a liquid medium. Overall, such compositions play an important role in iron corrosion studies [344,346,347,350,351]. Finally, compositions with magnetite and maghemite, presumably due to the presence of iron(II) and iron(III) cations, are actively used for the remediation of waste [348,352–357].

Table 7. Data on the structures containing iron oxide atomic clusters and an amorphous iron oxide phase.

Composition	Main Mechanisms of Iron Oxide Formation	Declared Applications	Phase Verification Techniques	Refs.
Iron oxide atomic clusters	Combustion synthesis from $\text{Fe}(\text{CO})_5$ mixed with hydrogen and oxygen, high irradiance laser ionization from pressed Fe_2O_3 and Fe_3O_4 tablets, biomineralization inside the ferritin shell, reaction of laser ablated iron foil with 5% O_2 seeded in a helium carrier gas	Catalysis, biomedicine, electronics, sensors, prediction of the magnetic properties of FeO_x NPs, natural iron storage process studies, photovoltaics	MBMS ¹ , PMS ² , RMDS ³ , TEM, LI-TOFMS ⁴ , density-functional theory calculations, European Synchrotron Radiation Facility	[271–277,281]
Surface iron oxide layer on metal	Multicycling of an iron foil electrode between the switching potentials, formation of iron oxide species after reaction with Cr(VI) and Cu(II)	Chemical water treatment, production of molecular hydrogen, removal of contaminants	RMDS, XRD, XPS, FTIR, EDS	[278,279,282]
Amorphous ferric oxides	Adding Fe(II) or Fe(III) to seawater	Bioavailable iron studies	XAS, XRD	[266]
Amorphous Fe_2O_3 in a silica matrix	Addition of Fe(III) to synthetic buffered solution or soluble microbial systems	Chemical water treatment	UV-Vis	[267]
Poorly crystalline iron oxides	Impregnation of mesoporous silica with ferric nitrate and calcination	Antibiotic adsorption	TEM, XRD, FTIR, UV-Vis	[268]
Amorphous iron oxide nanostructures	Iron oxide biomineralization by iron-reducing bacteria	Geochemistry	ICP-MS	[270]
Two-dimensional iron oxide on Au(111)	Photothermal reaction inside a droplet of iron(III) acetylacetone solution	Electronics, sensors	TEM, SAED, EDS, RS	[269]
Iron oxide layer on zerovalent iron NPs	Evaporating iron atoms, annealing and cooling down to 300 K in O_2	Catalysis	STM, density-functional theory calculations	[142]
Ferric oxide NPs	Zerovalent iron corrosion in an electrolyte solution	Treatment of contaminated aquifers	UV-Vis, XAS	[283]
Ultra-thin iron oxide nanowhiskers	Protein-promoted conversion of Fe(II) into insoluble ferric iron oxides	Mitochondrial iron mishandling studies	UV-Vis	[284]
High valent iron oxo complexes	Iron oleate complex followed by selective decomposition at 150 °C	Biomedicine	TG-DSC, TEM, SAED, RS, XPS, FTIR	[285]
FeO(111)-like film on Fe(110) surface	Fluorine-substituted Fe–tetra-amidomacrocyclic ligand oxidation	Photocatalysis	UV-Vis, EPR, high-resolution mass spectrometry	[286]
Colloidal $\text{Fe}-\text{Fe}_x\text{O}_y$ composite NPs	Initial oxidation of Fe(110) in oxygen via Frank–Van der Merwe mechanism	Catalysis, pigments, electronics	XPS, XAS, STM, AES, LEED ⁵ , STS ⁶	[280]
Biogenic microtubular iron oxides	Oxidation of metal NPs via a nanoscale Kirkendall process	Clean fuels, catalysis, electrochemical energy	TEM, SAXS, WAXS, RMDS	[287]
Iron oxide model thin-film electrodes	Biotic formation of organic sheaths and subsequent abiotic deposition of Fe	Catalysis, pigments	EDS, RS, TEM, XRD, STEM	[288]
Iron(III) oxide/hydroxide nanonetworks	Thermal oxidation of pure metal iron substrates at 300 ± 5 °C in air	Lithium-ion batteries	RS, XPS, SIMS ⁷	[289]
Fe ⁰ -iron oxide core-shell NPs	Synthesis of iron(III) oxide/hydroxide xerogels from a hydrated ferric nitrate	Electronics, catalysis, sensors	XPS, FTIR, XRD, TEM	[290]
Soil samples with amorphous iron oxides	Precipitation from ferrous sulfate with leaf extracts	Removal of nitrate in aqueous solution	EDS, XRD, FTIR	[291]
Reticular pipeline cracks filled with iron oxide	Abiotic mineralization in soil pore structures	Soil weathering studies	XRD, ICP-AES	[292]
	Decarburization and diffusive oxidation of steel matrix	Corrosion resistance studies	EDS	[293]

¹ Molecular beam mass spectrometry. ² Particle mass spectrometry. ³ Reactive molecular dynamics simulations.

⁴ Laser ionization orthogonal time-of-flight mass spectrometry. ⁵ Low-energy electron diffraction. ⁶ Scanning tunneling spectroscopy. ⁷ Secondary ion mass spectrometry.

Table 8. Data on the structures containing co-existing $\alpha\text{-Fe}_2\text{O}_3$ and $\gamma\text{-Fe}_2\text{O}_3$ phases.

Composition	Main Mechanisms of Iron Oxide Formation	Declared Applications	Phase Verification Techniques	Refs.
Saprolitic soil samples	Aerobic weathering of Fe-bearing minerals		XRF, UV-Vis, XRD	[298]
Loess and paleosol samples with iron oxides	Aerobic weathering of Fe-bearing silicate minerals	Pedogenic process studies	XRD, UV-Vis	[297]
Oxidized iron items	Soil iron corrosion limited by the diffusion of dissolved oxygen	Heritage science	EDS, XRD, RS	[295]
Surface iron oxide layer on metal	Anodic film formation on steel immersed in sour acid media	Corrosion resistance studies	XRD, EDS	[302]
Graphene-iron oxide nanotube composite	An adept template-free hydrothermal route from ferrous sulfate	Removal of the toxic heavy metal Cr(VI)	EDS, XRD, FTIR, UV-Vis, TEM	[299]
Polyacrylonitrile/iron oxide composite	Hydrothermal method for in situ growth of iron oxide; iron alkoxide hydrolysis	Removal of Congo red dye from water	FTIR, XRD, EDS, ICP-AES	[300]
Carbon/ Fe_xO_y magnetic composites	Mechanical mixing and thermal treatment under N_2 atmosphere	Wastewater treatment	XRD, TG-DSC, EDS, FTIR	[301]
Isoelement synthetic heterostructures	Hydrothermal method combined with controlled partial annealing process	Visible-light photocatalysis	XRD, TEM, XPS, UV-Vis, EPR	[296]

Table 9. Data on the structures containing co-existing $\alpha\text{-Fe}_2\text{O}_3$ and Fe_3O_4 phases.

Composition	Main Mechanisms of Iron Oxide Formation	Declared Applications	Phase Verification Techniques	Refs.
Inclusions of iron oxides in ore samples	Precipitation during protracted hydrothermal fluid/rock interaction, biological oxidation of Fe(II) by photoautotrophs, microbial sedimentary ferric iron flux, infiltration by hypogene and supergene fluids during or after deformation	Banded iron formation studies, geochemistry, late Archean and early Paleoproterozoic studies, iron oxide copper gold system studies	ICP-MS, EDS, XRF, SAED, TEM, XRD, ICP-AES, TG-DSC	[303–311]
Surface iron oxide layer on metal	Tribo-oxidation wear of the cast iron disc	Brake system wear studies	EDS, XRD, TEM, SAED	[315]
Iron oxide NPs	Anodization of Fe sheet in ethylene glycol electrolyte and calcination	Biomedicine, catalysis, photovoltaics, electronics	XRD, EDS, XPS, RS, FTIR	[312]
Iron oxide inclusions in concrete samples	Corrosion of a steel-reinforcing bar in air-entrained concrete with chlorides	Corrosion resistance studies	EDS	[318]

Table 9. Cont.

Composition	Main Mechanisms of Iron Oxide Formation	Declared Applications	Phase Verification Techniques	Refs.
Iron oxide nanosheets and nanowires	Thermal oxidation of iron foils in the presence of water vapor	Cr(VI) removal	XRD, TEM, RS, UV–Vis	[319]
Iron oxide hollow spheres	Microwave-hydrothermal ionic liquid method, calcination and autocatalysis	Photocatalysis	XRD, TEM, UV–Vis	[314]
Inclusions of iron oxides in mineralized rocks	Abiotic formation of a mineral deposit	Geochemistry	XRF	[320]
Theoretically calculated iron oxide phases	Radiation-chemical oxidation of Fe depending on pH and oxygen content	Precambrian studies	Kinetics of iron oxidation calculations	[321]
Iron oxide NPs supported on biogenic silica	Iron oxide NP impregnation under hydrothermal conditions and calcination	Rhodamine B photocatalytic degradation	EDS, XRD, UV–Vis, TEM	[316]
Sediment samples with inclusions of iron oxides	Mineralization by variable diagenetic processes	Rock magnetism studies	XRD, EDS	[322]
Iron oxide nanorods	Sols of ferric hydroxide radiolysis in water under gamma irradiation	Electronics, biomedicine	XRD, TEM	[314]
Spinel-bearing peridotite	Oxidation of ferrous iron in olivine and pyroxene into ferric iron	Serpentinization studies	FTIR, EDS	[323]
Iron oxide inclusions in kaolin clay samples	Abiotic chemical precipitation	Clay chemistry and morphology studies	ICP-AES, XRD, XRF, TG-DSC	[324]
Precipitates containing iron oxide inclusions	Biomineralization by photosynthetic Fe(II)-oxidizing bacteria	Banded iron formation studies	XRD, EDS	[325]
Iron-mineralized biofilms	Dissolution and re-precipitation of iron oxide minerals	Bioremediation of iron ore mines	–	[326]
Iron oxide nanotubes	Template-based electrodeposition and calcination under oxidizing atmospheres	Biomedicine, electronics, gas sensors, catalysis	TEM, XRD, SAED	[317]
Iron oxide powder	Hydrothermal process with a use of pyrite cinder lixivium	Pyrite cinder reutilization	FTIR, XRD, TEM, SAED	[327]
Growth model for submarine deposits	Transformation of primary (hydr)oxides via reduction by organic matter	Banded iron formation studies	–	[328]

Table 10. Data on the structures containing co-existing FeO and Fe₃O₄ phases.

Composition	Main Mechanisms of Iron Oxide Formation	Declared Applications	Phase Verification Techniques	Refs.
Fe-rich carbonates with inclusions of iron oxides	Laser heating of natural goethite in a diamond anvil cell in CO ₂	Earth's mantle studies	XRD, XAS, TEM, EELS, HAADF-STEM, SAED	[329]
Samples with partially reduced FeO and Fe ₃ O ₄	Porous iron growth from wüstite in CO/CO ₂ and H ₂ /H ₂ O systems	Porous iron growth mechanism studies	–	[330]
Fe/oxide core-shell NPs	Formation of Fe ₃ O ₄ during the oxidation of Fe NPs; high-temperature reduction of Fe ₃ O ₄ to FeO by an electron-beam	Environmental remediation, electronics, catalysis, biomedicine, energy storage	TEM, SAED, EELS, HAADF-STEM, EDS	[331]

Table 11. Data on the structures containing co-existing $\gamma\text{-Fe}_2\text{O}_3$ and Fe_3O_4 phases.

Composition	Main Mechanisms of Iron Oxide Formation	Declared Applications	Phase Verification Techniques	Refs.
Iron oxide NPs	Thermal decomposition of iron oleate, continuous flow synthesis, co-precipitation of $\text{Fe}^{3+}/\text{Fe}^{2+}$ ions, aerosol spray pyrolysis with the use of ferric nitrate and ferric chloride, precipitation from iron salts with natural leaf extract	Biomedicine, soil remediation, metal removal, wastewater treatment, electronics, catalysis, energy storage, groundwater remediation	TEM, XRD, FTIR, SAED, TG-DSC, UV-Vis, SAXS, neutron diffraction, EDS, MSP, EELS, EPR, ICP-MS, XAS, RS	[45,332–340,352–355,358–362]
Surface iron oxide layer on metal	Oxidation of a pure iron surface in oxygen, electrochemical reduction of lepidocrocite and ferrihydrite, in situ formation on an iron surface depending on the applied potential	Iron oxidation studies, atmospheric steel corrosion studies, groundwater remediation, corrosion protection studies	XPS, XRD, XAS, RS, AES, ellipsometry	[345–349]
Oxidation layer on archaeological steel	Combined iron oxidation/iron(III) oxyhydroxide reduction without O_2	Corrosion studies on ancient metallic objects	EDS, RS	[343]
Iron oxide-TiO ₂ nanorod heterostructures	Precipitation by injection of $\text{Fe}(\text{CO})_5$ into stirred TiO ₂ containing mixture	Optoelectronics, biomedicine, catalysis	XRD, XAS, ICP-AES, TEM, UV-Vis	[363]
Iron oxide in nanoscrolls and nanoribbons	Precipitation from ferric and ferrous chloride with ammonia solution	Lithium-ion storage, photocatalysis, biosensors	TEM, FTIR	[364]
Iron oxide hollow core/Shell NPs	Solvothermal synthesis from FeCl_3 and urea in ethylene glycol and calcination	Biomedicine	XRD, TEM, TG-DSC, UV-Vis	[365]
Thin-film nanocomposite membrane with iron oxide	In situ synthesis from aqueous solutions containing ferric chloride	Biofouling protection	EDS, TEM, XPS, UV-Vis, XRD, TG-DSC	[366]
Magnetoferitin iron oxide NPs	Controlled mineralization from recombinant human H-chain ferritin	Biomedicine	TEM	[367]
Iron oxide-based hollow magnetic nanoparticles	Synthesis from iron pentacarbonyl in 1-octadecene and oleylamine	Exchange bias studies	XRD, TEM, FTIR, MSP, F-AAS	[368]
Albumin protein-based magnetic NPs	Co-precipitation of FeCl_2 and FeCl_3 by ammonia in the presence of protein	Biomedicine	TEM, TG-DSC	[369]

Table 11. *Cont.*

Composition	Main Mechanisms of Iron Oxide Formation	Declared Applications	Phase Verification Techniques	Refs.
Composite of organic matrix and iron oxide NPs	Thermal decomposition of iron(III) oleate complex	Biomedicine	TEM	[370]
Iron oxide powder	Photochemical oxidation of siderite (FeCO_3) by ultraviolet radiation	Banded iron formation studies	XRD	[371]
Interfacial iron oxide layer on iron artifacts	Iron corrosion in an anoxic environment after a pH increase at the interface	Anoxic corrosion of archaeological steel studies	HAADF-STEM, RS, EDS, SAED, SIMS	[344]
Iron oxide hydroxyapatite core/shell nanocomposites	Precipitation from ferric and ferrous chloride with ammonia under N_2	Biomedicine	TEM, FTIR, XRD, AAS, EDS	[372]
Chitosan-based beads with iron oxide NPs	Co-precipitation from ferric and ferrous chloride with NaOH solution	Remediation of water sources	XRD, FTIR, TG-DSC, EDS	[356]
Silica–iron oxide nanocomposite	Co-precipitation from ferric and ferrous chloride with ammonia solution	Toxic species removal	XRD, TEM, FTIR, UV-Vis, SAED	[357]
Vertical tube-shaped iron-oxide accumulations	Deep water corrosion of carbon steel	Marine corrosion studies	EDS	[351]
Hydrogels with embedded iron oxide NPs	In situ mineralization of iron ions in a hydrogel matrix	Dye removal	XRD, FTIR, TG-DSC, TEM	[373]
Corroded reinforced concrete	Iron corrosion in a laboratory corrosion chamber	Steel rebar corrosion studies	XRD, EDS	[350]
Porous hollow iron oxide NPs on carbon nanotubes	Etching of $\text{Fe}-\text{Fe}_x\text{O}_y$ intermediate with nitric acid aqueous solution and drying	Biomedicine, catalysis, separation	TEM, XRD	[374]
Iron oxide embedding of bacterial cells	Biomineralization by thermophilic iron-reducing bacteria	Biogenic iron mineral formation studies	XRD	[375]
Activated carbon aerogel with iron oxide inclusions	Hydrothermal synthesis from ferrous sulfate with ammonia	Catalytic oxidation of pesticides	XRD, FTIR, XPS, TEM	[376]
Polyglycerol-grafted iron oxide NPs	Thermal decomposition of iron(III) acetylacetone in triethylene glycol	Biomedicine	TEM, TG-DSC, FTIR, ICP-AES	[377]

3.4. The Structures Containing Three or More Co-Existing Iron Oxide Phases

The co-existence of three or more iron oxide compounds in a single heterogeneous composition makes it useless to try to precisely distinguish every standalone phase. Thus, studies devoted to such a case are considered in this section and listed in Table 12. Iron oxide NPs and the surface oxide layer on metal surfaces are the largest groups of papers on the structures containing mixed iron oxide phases. Synthesis techniques for obtaining mixed iron oxide NPs include physical ones (flame synthesis [378], thermal oxidation [379] and laser ignited combustion [376]) and chemical ones (thermal decomposition [82,380] and precipitation [341], including “green” process [381]). The main application of such NPs is in biomedicine [82,378–380].

Table 12. Data on the structures containing mixed iron oxide crystal phases [42,79,380–407].

Composition	Main Mechanisms of Iron Oxide Formation	Declared Applications	Phase Verification Techniques	Refs.
Iron oxide NPs	Thermal decomposition of an iron oleate in the presence of oleic acid, flame synthesis from $\text{Fe}(\text{CO})_5$, precipitation from ferric chloride in a natural leaf extract, thermal oxidation of polycrystalline Fe foils	Biomedicine, ferrofluids, electronics, immobilization of Cd in soils, catalysis, metal fuel	PMS, TEM, EDS, TG-DSC, SAED, XRD, XPS, FTIR, UV-Vis, EELS	[79,380–384]
Surface iron oxide layer on metal	Carbon steel corrosion at room temperature, iron carboxylate transformation to iron oxides, electrochemical anodization of metal in simulated acid rain solution	Corrosion resistance studies, railway industry, fireside corrosion studies	EDS, XRD, XRF, RS, XPS, FTIR, TG-DSC	[385–389]
Powder containing iron oxide microparticles	Carbothermal reduction of red mud by heating in a microwave furnace	Alumina production by-product recycling	XRD, EDS, XRF, TG-DSC	[400]
Iron oxide microfibers arranged in a complex hierarchical structure	Thermal decomposition of $\text{Fe}(\text{CO})_5$ and silicone oil and microwave vaporization	Environmental safety, biomedicine, sensors	EDS, XRD	[396]
Fe-based nanocomposite catalysts containing agglomerates of the two types	Melting of iron, aluminum and copper salts and reduction	Low-temperature catalytic oxidation of CO	XRD, TEM, XAS, EDS	[393]
Iron oxide powders containing hematite, magnetite and maghemite	Chemical precipitation from ferric nitrate and ferrous sulfate and heating	Inositol phosphate selective retention in soil	XRD	[399]
Silica–iron oxide nanocomposite with hematite, magnetite and wüstite	Silica promotion upon the reduction of amorphous iron oxide in hydrogen	Catalysis	XRD, TEM, EELS, STEM, SAED	[394]
Iron(II) and (III) oxides inclusions in char composites	Microwave pyrolysis of Moso bamboo samples with ferric chloride	Syngas production	XRD	[401]
Ultra-thin magnetic iron oxide films containing Fe_3O_4 , $\gamma\text{-Fe}_2\text{O}_3$ and FeO	Thermally induced phase transformation of ultra-thin iron oxide films	All oxide heterostructures	XRD, XPS	[402]
Surface iron(II) and (III) oxide layer on iron granules	Atomization of the molten semi-steel with a rotary cup atomizer	Iron powder production	TG-DSC, XRD	[403]
Iron oxide (Fe_3O_4 , $\gamma\text{-Fe}_2\text{O}_3$ and $\alpha\text{-Fe}_2\text{O}_3$) inclusions in fly ash samples	Coal combustion and flue gas cooling at various temperatures	Selenium adsorption by iron minerals	XRF, MSP, XPS	[404]
High-pressure metastable phases $m\text{FeO}\text{-}n\text{Fe}_2\text{O}_3$	Formation of complex iron oxide crystals under high-pressure conditions	Earth and planetary deep interior studies	–	[24]
Iron(III) oxide submicron inclusions in a biofilm on a basalt surface	Microbial direct or non-direct biomineratization	Biovermiculation studies	EDS	[388]
Inclusions of poorly crystalline iron(III) oxides in ore samples	Microbial biomineratization	Mine remediation, waste stabilization	SIMS	[390]
Iron oxide (Fe_3O_4 , $\gamma\text{-Fe}_2\text{O}_3$ and $\alpha\text{-Fe}_2\text{O}_3$)/iron composite	Reactive spark plasma sintering of mechanically activated Fe powders	Magnetic material development	XRD, TG-DSC	[405]

Table 12. *Cont.*

Composition	Main Mechanisms of Iron Oxide Formation	Declared Applications	Phase Verification Techniques	Refs.
Core–shell Fe@Fe ₂ O ₃ nanowires containing Fe(II) and Fe (III) oxides	Ferric chloride reduction with sodium borohydride and surface oxidation	Cr(VI) removal	XRD, UV-Vis, TEM, XPS	[406]
Iron oxide submicron particles accumulated in the cytoplasm of cells	Intracellular or extracellular microbial biomineralization	Hydrothermal vent field studies	XRD, TEM, SAED, EDS	[389]
Deposit samples with inclusions of iron(II) and (III) oxides	Anoxygenic photosynthesis by a photoferrotrophic bacterium	Banded iron formation studies	—	[391]
Bovine serum albumin–iron oxide suspensions	Precipitation from ferric nitrate with NaOH in N ₂ atmosphere	Boreal forest studies	FTIR	[398]
Iron oxide (Fe ₃ O ₄ , γ-Fe ₂ O ₃ and α-Fe ₂ O ₃) magnetic short nanotubes	Anion-assisted hydrothermal route by using phosphate and sulfate ions	Biomedicine, ferrofluids, electronics, spintronics	TEM, SAED, XRD	[407]
Fe-biochar composites containing iron(II) and (III) oxides	Pyrolysis of ferric chloride in a biochar matrix at various temperatures	Arsenic removal, environmental remediation	XRD, XPS, RS, FTIR	[397]
Fe _x O _y @C spheres embedded with highly dispersed iron oxide NPs	One-pot hydrothermal cohydrolysis-carbonization using iron	Catalysis	TEM, EDS, XAS, XRD, MSP	[395]
Powder with inclusions of submicron iron oxide particles	Reduction of solid ferric hydroxide by iron-reducing bacteria	Microbial iron reduction studies	EDS, RS	[392]

An iron oxide layer on the metal surface is the second commonly considered structure, which plays an important role in corrosion studies [383–385] and can be formed both naturally (e.g., iron carboxylate transformation in a leaf contamination on rails [386] or fireside corrosion of steel in the furnace walls in boilers [384]) and synthetically (e.g., in situ oxidation of the surface of a steel sample in a controlled atmosphere [387] or electrochemical anodization of metal in a simulated acid rain solution [385]).

Compositions with mixed iron oxides can originate via a biogenic route, including microbial direct or non-direct biomimetic mineralization [388–390], anoxygenic photosynthesis by a photoferrotrophic bacterium [391] and the reduction of solid ferric hydroxide by iron-reducing bacteria [392]. Biogenic iron oxide structures can be used in microbial iron reduction studies [392], banded iron formations [391] or hydrothermal vent field studies [389] and waste remediation [390].

Similarly to the above mentioned iron oxide structures, various compositions containing mixed iron oxide phases can be applied for catalytic purposes. These compositions include iron oxide NPs [379], Fe-based nanocomposites [393], silica–iron oxide nanocomposites [394] and Fe_xO_y@C spheres [395] and can be obtained with the use of chemical [394,395] or physical [379,393] synthesis.

Finally, in some cases, such structures are used for various environmental tasks, including environmental safety [396], environmental remediation [397], boreal forest studies [398], inositol phosphate selective retention in soil [399], biovermiculation studies [388] and the Earth and planetary deep interior studies [24].

3.5. The Main Characterization Techniques Used to Verify Phase Composition

From analyzing Tables 2–12, the most frequently used characterization techniques can be revealed. These techniques include X-ray powder diffraction (XRD), energy-dispersive X-ray spectroscopy (EDS), transmission electron microscopy (TEM), Fourier-transform infrared spectroscopy (FTIR), X-ray photoelectron spectroscopy (XPS), UV-visible(-NIR) spectroscopy (UV-Vis), selected area electron diffraction (SAED), Raman spectroscopy (RS), thermogravimetry/differential scanning calorimetry (TG-DSC), X-ray absorption spectroscopy (XAS), Mössbauer spectroscopy (MSP) and X-ray fluorescence (XRF). The diagram showing the partial distribution between these techniques is presented in Figure 5.

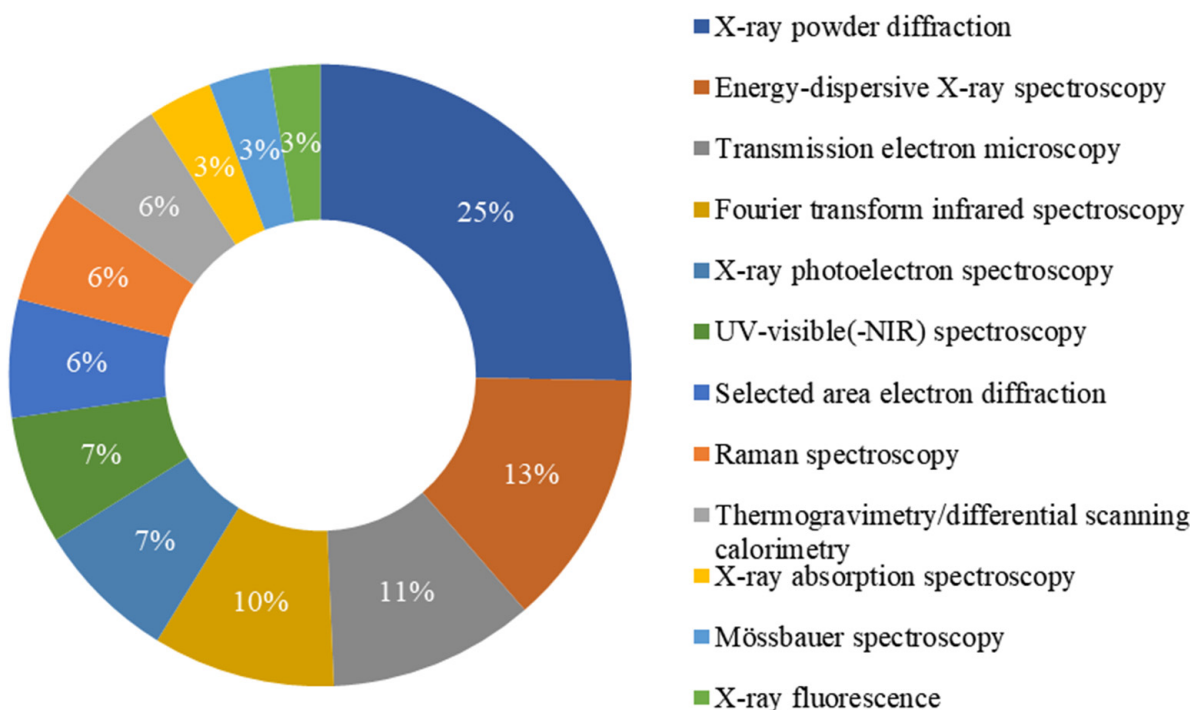


Figure 5. Main characterization techniques used to verify phase composition.

In some cases, while the crystal structure of the co-existing iron oxide compounds differs significantly (e.g., for hematite and magnetite), the most common and available techniques are suitable for phase composition verification, including XRD and XRF. For instance, XRF and XRD techniques were used to determine the chemical and crystalline phase composition, accordingly, of clay samples containing iron oxides [324]. Another possible example is $\varepsilon\text{-Fe}_2\text{O}_3$, a crystal structure that is also quite distant from the other iron(III) oxide polymorphs and can be distinguished with the use of RS and XAS [258], or even with the use of a standalone XRD technique [37]. Contrary to the above, the simultaneous existence of magnetite and maghemite crystal phases cannot be adequately analyzed with XRD, SAED or some other techniques due to the similar crystal structure of these compounds and non-stoichiometry of synthetic [38] or natural [6,295] magnetite. In this case, the MSP technique can give additional information on the crystal structure, including magnetite to maghemite partial transition or the superparamagnetic state of NPs [38]. MSP can be applied to characterize samples composed of homogeneously sized iron oxide NPs above the blocking temperature in a superparamagnetic regime [368]. Mössbauer measurements were performed to investigate detailed iron mineralogy compositions in magnetic fractions of fly ashes [405]. Perecin et al. showed that although Mössbauer spectra with two sextets were expected for pure magnetite, an extra sextet suggested the maghemite phase's presence in the sample, in agreement with the FTIR results [89]. The high oxidation degree of magnetite can be confirmed by low isomer shift values [342]. MSP results can show a shift of the Morin transition in hematite upon increasing Ru^{3+} -to- Fe^{3+} substitution, similar to the shift in the Morin transitions occurring in temperature-dependent magnetization measurements [224].

3.6. The Analysis of the Distribution of Iron Oxide Compounds by their Frequency of Mention

Based on the data provided in Tables 2–12 (in total, more than 300 research articles were analyzed), a histogram was built (Figure 6). Compositions containing magnetite are the most frequently considered in scientific articles. This can be explained by taking into account the highest saturation magnetization of this iron oxide compound among others and also because of the wide biomedical application of magnetite NPs. The second most commonly described compound is hematite, presumably due to its use in photocatalysis

and its abundance (the same for magnetite ores) in nature. The third important iron oxide compound is maghemite, since $\gamma\text{-Fe}_2\text{O}_3$ NPs are often used instead of magnetite NPs due to the high oxidation instability of Fe_3O_4 in air atmospheres and, therefore, difficulties in its preservation without an inert atmosphere or a protective shell. Other iron oxide compounds, including FeO , $\beta\text{-Fe}_2\text{O}_3$ and $\varepsilon\text{-Fe}_2\text{O}_3$, are metastable and/or their synthesis procedure is too complex, therefore scientific studies on them are relatively rare.

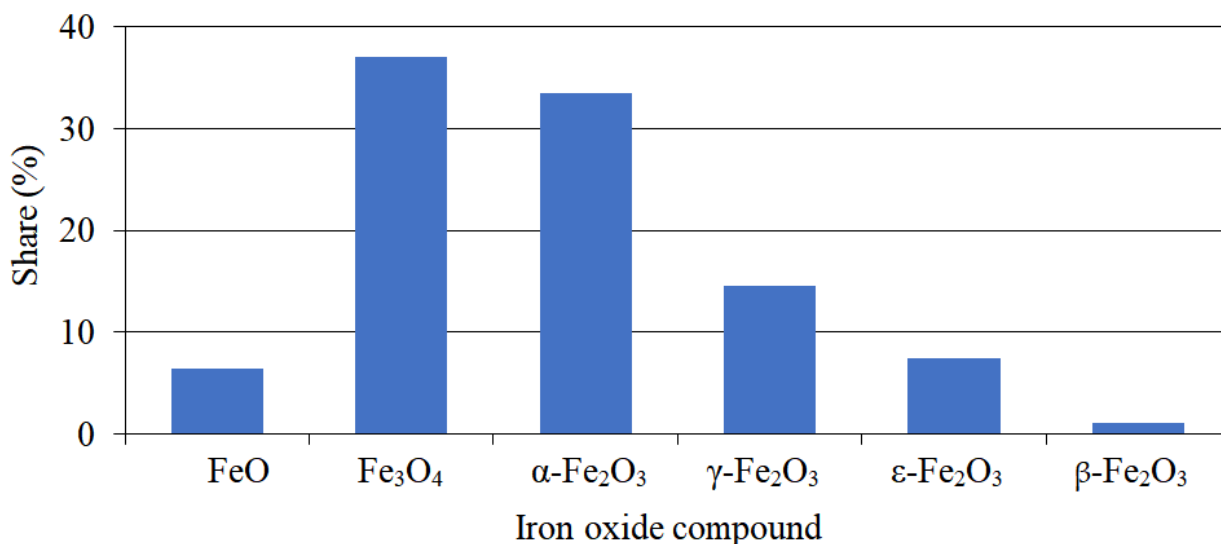


Figure 6. Distribution of iron oxide compounds by their frequency of mention (based on the analyzed research articles mentioned in Tables 2–12).

3.7. The Main Mechanisms of Iron Oxide Formation

Using the information given in Tables 2–12, the generalized scheme illustrating some widely considered mechanisms of iron oxide formation was drawn (Figure 7). Terrigenous formation implies abiotic mineralization [100,102,206,219,292,324]. Extraterrestrial formation including samples from Mars [113] originated from precipitation from oxygenated iron-rich water [198] and abiotic formation in an aqueous environment of deposition [124].

Biomineralization implies bacterial magnetosome formation [94,96–98], formation by dissimilatory iron-reducing bacteria [95], bacterial reduction of iron hydroxide [122,166,392], biomineralization by anoxygenic photoferrotrophy [210], biomineralization inside the ferritin shell [276,277], biogeneration of magnetite with a use of the amyloid peptide A β ₄₂ in the case of brain diseases [160], etc.

Iron and iron alloy corrosion include chemical [106,109,238,350] and electrochemical [86,349,385] processes, either natural or intended. Ceramics firing implies the calcination of a milled mix at a high temperature in an oxidizing atmosphere [229], high-temperature firing of local iron-rich area on a ceramic glaze [140] and surface iron enrichment and firing of wares under reducing conditions [132]. Biomimetic synthesis refers to a process using natural plant extracts [91], iron oxide NP formation on biogenic silica [316], nucleation of Fe_3O_4 NPs mediated by the iron-binding protein Mms6 [92] and protein-promoted conversion of Fe(II) into insoluble ferric iron oxides [284].

Chemical precipitation includes co-precipitation by sodium hydroxide from an iron chloride solution [82], precipitation from Fe^{3+} and Fe^{2+} ions by urea with chitosan [149], precipitation from iron(II) sulfate heptahydrate with NaOH [158] and precipitation from iron(III) ethoxide with ethanol in the surfactant solution [179]. Physical deposition implies electron-beam deposition [142], liquid-phase atomic layer deposition [232], pulsed laser deposition on the Ga-terminated surface of a GaN (0001) [260] and chemical vapor deposition from an Fe organic liquid source [258]. Finally, mechanochemical synthesis includes mechanical mixing and thermal treatment under a N_2 atmosphere [301], reactive spark plasma sintering of mechanically activated Fe powders [405] and milled zerovalent

iron corrosion in anaerobic synthetic groundwater [348]. All the listed routes of iron oxide formation can be either intended (controlled) or natural (uncontrolled).

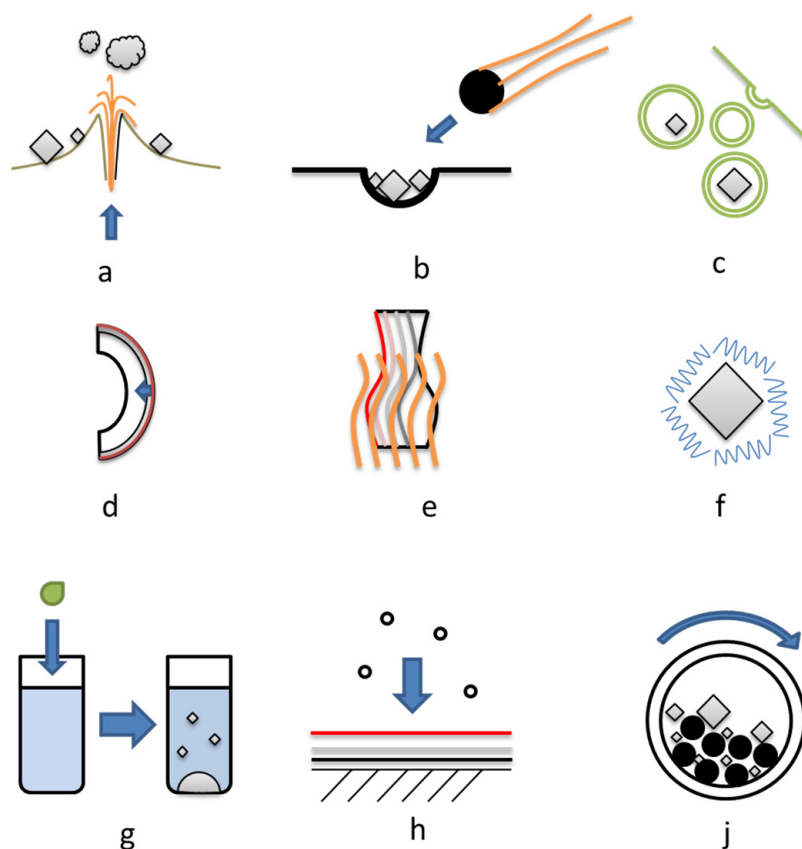


Figure 7. Mechanisms of iron oxide formation: (a)—Terrigenous formation; (b)—Extraterrestrial formation; (c)—Biomimetic synthesis; (d)—Iron and iron alloy corrosion; (e)—Ceramics firing; (f)—Biomimetic synthesis; (g)—Chemical precipitation; (h)—Physical deposition; (j)—Mechanochemical synthesis.

4. The Main Applications of the Structures Containing Iron Oxides

The largest amount of scientific papers being analyzed describes various biomedical applications of iron oxides, mainly magnetite/maghemit NPs. Photocatalytic oxidation and other applications in catalysis are the second major practical use of iron oxides, with a predominance of compositions with hematite. The third important field of use is electronics, including spintronics, data storage development and optoelectronics, mainly for thin ferrimagnetic or antiferromagnetic iron oxide films. Corrosion science is a quite obvious, but still very important area of application, since iron oxide passivation can provide a better reliability of steel pipelines, safety of ancient artifacts for heritage science, etc. Waste remediation is generally based on the possibility of iron oxidation from iron(II) to iron(III) and to absorb or bind inorganic and organic pollutants. Finally, serious attempts in geosciences with the use of various iron oxide compositions are still being made, despite a long history of research. Studies of natural iron ores can give much information about Earth's evolution, including Precambrian research.

Biomedical applications of iron oxides include T_2 magnetic resonance imaging (MRI). MRI contrast agents are based on superparamagnetic NPs; their nanocluster formation increases the magnetic signal and subsequently enhances imaging sensitivity or cell labeling efficiency [29]. Magnetic hyperthermia with alternating magnetic fields requires magnetic NPs having an effective heating rate to enable therapeutic applications [11]. There are diverse bioinspired approaches for the synthesis of magnetic nanochains with optimal properties for biomedical applications, including magnetically guided drug delivery [13].

The integration of magnetic NPs and organic dyes into single platforms demonstrated their use as bimodal imaging agents for both *in vitro* and *in vivo* imaging and in multifunctional platforms that perform several tasks in parallel (e.g., dual-mode imaging and photodynamic therapy or drug delivery) [14].

Iron oxide formation mechanisms are important for understanding formation processes of iron-relevant minerals in Precambrian banded iron formations, granular iron formations and associated iron-poor strata [4,33]. This understanding also includes the origin of probably the first protosensory system evolved on Earth, i.e., magnetotaxis, while the precise mechanism of biogenic magnetite mineralization on early Earth is still unknown [8]. Well-known processes of the biomineratization of iron can help in better understanding human body iron metabolism and in curing diseases linked with iron-damaged regulation [10]. Today, by far the single most important use (by volume) of iron oxides is as a source of Fe, which is subsequently processed to make steel [3]. Another important iron oxide industrial application is photoelectrochemical water splitting. It is a leading strategy for producing a promising renewable store of energy—hydrogen [12]. Iron oxides, including magnetite, maghemite and hematite, are widely used in heterogeneous catalysis processes and have been attractive alternatives for the remediation of polluted soil, groundwater and wastewater based on a heterogeneous Fenton reaction (a combination of a solid Fe-based catalyst and H₂O₂) [25,26]. Partially oxidized zerovalent iron NPs with a core-shell structure can be used to remediate groundwater and wastewater contaminated by chlorinated organic compounds, heavy metals, dyes and phenols [27].

Rare iron(III) oxide polymorphs can also be practically used. Thus, β -Fe₂O₃ has found a few applications in an electro-catalyst for the reduction of hydrogen peroxide, in optoelectronics and in red ferric pigments [19]. A very high room-temperature coercive field makes ε -Fe₂O₃ suitable for use in recording media; its magnetoelectric coupling and millimeter-wave ferromagnetic resonance are useful in electric/magnetic field tunable devices and for millimeter wave absorption on the walls of an interior room or on the body of a car, train or airplane [36]. In some cases, e.g., in catalysts, amorphous Fe₂O₃ NPs can be more active than nanocrystalline polymorphs or particles of metallic iron of the same diameter [39]. The structures of iron oxides are common to many binary systems and complex solid solutions; therefore, a rich set of isostructural compounds and solid solutions with tunable properties may be synthesized [23].

Ceramics, including composites containing inclusions of amorphous iron oxides, are suitable for various industrial applications. The process of transforming iron oxides from a glass network into a crystal nucleus was studied for the novel field of glass ceramics based on waste glass [408]. Prim et al. showed that iron oxide from a metal sheet treatment process may be used as a ceramic pigment by encapsulation in a crystalline and amorphous silica matrix [409]. Intended for hazardous waste incineration, glass ceramics containing hematite exhibited a superior compressive strength, volume density and water absorption [410]. Alumina-zirconia-titania ceramic membranes coated with a nanosized hematite layer can be applied in a combined ozonation-membrane filtration process [411]. The formation of solid solutions between mullite and transition metal cations, including iron, affects the thermal expansion of mullite ceramics through the distortion of the Al-O octahedral [412].

Less than 20 a wt% addition of iron oxide significantly lowered the softening and melting temperatures of CaO-Al₂O₃-MgO-SiO₂-based glass ceramics [413]. The lower melting temperature leads to a significant decrease in the price of the vitrification procedure and to the suppression of heavy metal evaporation during glass melting [414]. Such a class of glass ceramics possessing excellent mechanical characteristics (bending strength of 120 MPa, hardness of 9 GPa and fracture toughness of 1.6 MPa·m^{1/2}) was discussed, together with the remarkable effect of their vitrification on heavy metal immobilization [415]. One of the most low-temperature techniques, the sol-gel method, which involves the hydrolysis of the precursors of constituent oxides followed by their gelation, has the potential to yield magnetic ceramics, including bioceramics, with a more flexible composition range, better homogeneity, better bioactivity and controllable porous structure [416]. Nanostructured

catalyst-modified composite cathodes can be obtained by infiltrating a metal ion solution into a ceramic scaffold, followed by heating at a high temperature. A 3D heterostructured electrode decorated by amorphous iron oxide that works stably at 650 °C with an oxygen reduction reactivity comparable to that of a Pt-decorated one was obtained [417].

A wide range of metals such as gold, silver, copper, zinc, iron, platinum and palladium are fabricated in the form of NPs using algae and cyanobacteria and can be applied for infection control, diagnosis, drug delivery, biosensing and bioremediation [418]. An approach for the synthesis of highly pure, crystalline and biocompatible hematite NPs through the sole use of *Psidium guajava* leaf extract was proposed. The antibacterial efficacy of the obtained hematite NPs against Gram-positive as well as Gram-negative bacteria was established [419]. Both plants and microbes offer various ways to synthesize magnetite and maghemite NPs for potential dye degradation from industrial effluents from a variety of routes due to their vast genetic diversity and presence of various enzymes, respectively [420]. Co-substituted magnetite NPs were produced during the enzymatic reduction of a synthetic co-ferrihydrite using *Geobacter sulfurreducens* as an analogue to bioreduction processes in the natural environment to understand the natural biogeochemical cycling of cobalt in Fe-rich environments undergoing microbially mediated redox transformations [421]. Natural biogenic iron oxide extracted from banded iron formations showed high removal potential with the maximum sorption efficiency of 88.65% at a 30 g/L adsorbent dose [422].

Amorphous iron oxides are the promising material for various energetic and catalytic applications, including biomedicine. Compared to well crystalline Fe_2O_3 , amorphous Fe_2O_3 /graphene composite nanosheets exhibited superior sodium storage properties such as high electrochemical activity, a high initial Coulombic efficiency of 81.2% and a good rate of performance for sodium-ion batteries [423]. Efficient water oxidation catalysts have nominally amorphous mixed-metal oxide phases on their surface which are responsible for catalytic activity [424]. Amorphous iron oxide-packaged oxaliplatin prodrugs can be effective for cancer treatment, since the $\text{Fe}^{2+}/\text{Fe}^{3+}$ ions released by the amorphous iron oxide NPs produce a large amount of reactive oxygen species through Fenton's reaction [425]. Nanosized amorphous iron oxide showed higher catalytic activity with lower oxidant consumption in comparison to Fe_3O_4 - and Fe_2O_3 -based clay composites [426]. Amorphous Fe_2O_3 nanoflakes were biosynthesized by a novel sol-gel method using *Aloe vera* leaf extract, and their catalytic effect on the thermal decomposition of ammonium perchlorate was investigated [427]. Amorphous Fe_2O_3 NPs can act as efficient and robust photocatalysts for solar H_2 evolution without any cocatalysts [428]. Amorphous Fe_2O_3 /reduced graphene oxide/carbon nanofiber films were tested as flexible and freestanding anodes for lithium-ion batteries [429].

Corrosion resistance studies involving iron oxides are also important. Thus, potassium and chlorine may interplay to accelerate the corrosion of Fe-rich oxide scales, and an understanding of this process may open up new ideas for ways to decrease corrosion in highly corrosive environments [430]. Wheat straw fiber-reinforced polyvinyl chloride composites pigmented with iron oxide pigment have better seawater corrosion resistance, including better fiber/matrix interfacial interaction, lower total discoloration and higher surface hydrophobicity, mechanical properties and thermal stability [431]. Hydroxyapatite-bioglass- Fe_3O_4 -chitosan coatings showed an effective improvement of the surface properties, hemocompatibility and in vitro corrosion rate of a biodegradable magnesium alloy [432]. The corrosion resistance of the epoxy coating was experimentally improved using micaceous iron oxide and Al pigments [433]. In the case of stainless steel, iron oxide formation corresponds to a low pitting potential and corrosion resistance and leads to the degraded protective property of the oxide film [434].

Based on the data in Tables 2–12, a diagram illustrating the main declared applications of various compositions with iron oxides was built (Figure 8).

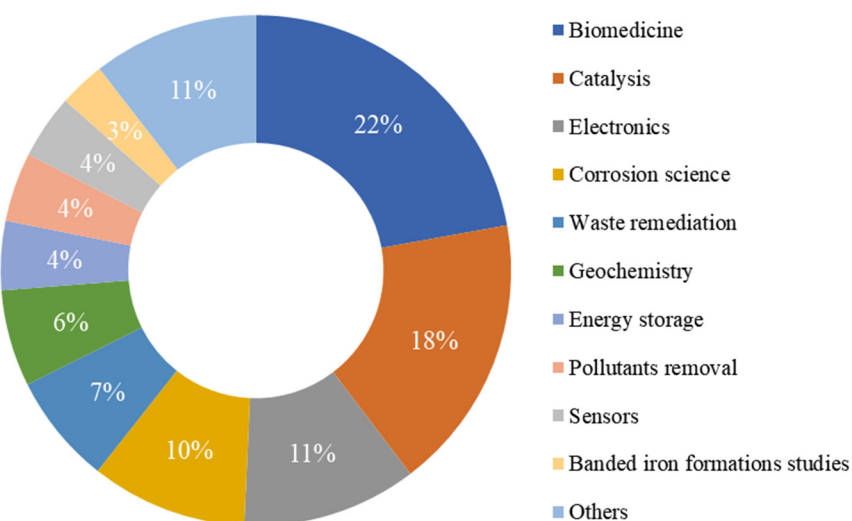


Figure 8. Main applications of iron oxides.

5. Summary and Perspectives

Iron oxide compounds are widely presented in various scientific and industrial areas due to their abundance on Earth. The possibility of changing the iron oxidation state between Fe^{2+} and Fe^{3+} lies in the basement of the biogenic iron cycle, which results in band iron formation accumulations and the deposition of fossilized magnetotactic bacteria, called magnetofossils [435]. The mass production of metallurgy and large iron deposits, e.g., the Kovdor deposit [6], provides a low cost of iron oxides compositions and their applicability for different technical purposes. High biocompatibility and modern synthesis techniques, including continuous-flow, biomimetic and biogenic processes, make it possible to translate academic research to clinical practice [435–437].

Integrating magnetic NPs with polymers allows for the fabrication of multifunctional systems for chemotherapy and magnetic hyperthermia therapy, which can also be simultaneously monitored by utilizing the magnetic resonance imaging capabilities of magnetic nanoparticle–polymer conjugates [14]. Such systems, e.g., iron-loaded crosslinked magnetic chitosan/graphene oxide, can also be widely applied for the practical environmental remediation of wastewater effluents containing organic pollutants [174]. The novel iron oxide-based materials can be used to improve solar fuel production [110]. The use of ferritin protein as a carrier of iron oxide NPs renders it more suitable for cancer diagnosis as an effective T_2 contrast agent with an expected reduced toxicity due to the prevention of NP interaction with the environment [367]. Two-phase iron oxide NPs (e.g., magnetite/maghemite core-shell structures) are promising for applications implying an intrinsic exchange bias effect [368].

As paleoenvironmental proxies, the iron abundance, speciation and isotopic composition recorded for an Archean ocean analogue in the future can assist in understanding the iron biogeochemistry in the water column and explain the information recorded in sedimentary rocks of the Precambrian ocean [104]. More empirical and experimental research is needed to quantify controlling factors of fractionation that occur with iron oxide crystallization in hydrothermal mineral systems [303]. Future work that reconstructs Archean seawater iron and Si concentrations will be crucial in evaluating the extent to which ferrous hydroxide auto-oxidation controlled the Archean iron cycle and the oxidation of the young Earth [103]. The crystal structure of iron oxides synthesized under high pressures, their bonding nature and build-up structural motifs may guide us in discovering novel iron oxide phases and will be useful in revealing the chemistry and physics of Earth and planetary deep interiors [24].

Despite the long history of iron oxide research, they continue to attract the high attention of scientists all over the world; therefore we can suppose the future fundamental and

applied discoveries in this field. The main possible tendencies, which can be predicted from the current state of the research, include the further integration of various scientific analytical approaches, e.g., well-developed in geosciences and nanotechnologies [37,38,294,438], a wider implementation of “green” and biomimetic technologies [439] and a combined use of natural iron oxides and synthetic components in a single structure [6].

Funding: This work was funded by the Russian Science Foundation (Grant No. 21-19-00719).

Institutional Review Board Statement: Not applicable.

Informed Consent Statement: Not applicable.

Data Availability Statement: Not applicable.

Conflicts of Interest: The author declares no conflict of interest.

References

1. Jolivet, J.P.; Chanéac, C.; Tronc, E. Iron oxide chemistry. From molecular clusters to extended solid networks. *Chem. Commun.* **2004**, *5*, 477–483. [[CrossRef](#)] [[PubMed](#)]
2. Guo, H.; Barnard, A.S. Naturally occurring iron oxide nanoparticles: Morphology, surface chemistry and environmental stability. *J. Mater. Chem. A* **2013**, *1*, 27–42. [[CrossRef](#)]
3. Parkinson, G.S. Iron oxide surfaces. *Surf. Sci. Rep.* **2016**, *71*, 272–365. [[CrossRef](#)]
4. Simonson, B.M. Origin and evolution of large Precambrian iron formations. *Spec. Pap. Geol. Soc. Am.* **2003**, *370*, 231–244. [[CrossRef](#)]
5. Skirrow, R.G. Iron oxide copper-gold (IOCG) deposits—A review (part 1): Settings, mineralogy, ore geochemistry and classification. *Ore Geol. Rev.* **2022**, *140*, 104569. [[CrossRef](#)]
6. Kharitonskii, P.; Bobrov, N.; Gareev, K.; Kosterov, A.; Nikitin, A.; Ralin, A.; Sergienko, E.; Testov, O.; Ustinov, A.; Zolotov, N. Magnetic granulometry, frequency-dependent susceptibility and magnetic states of particles of magnetite ore from the Kovdor deposit. *J. Magn. Magn. Mater.* **2022**, *553*, 169279. [[CrossRef](#)]
7. Navrotsky, A.; Mazeina, L.; Majzlan, J. Size-driven structural and thermodynamic complexity in iron oxides. *Science* **2008**, *319*, 1635–1638. [[CrossRef](#)] [[PubMed](#)]
8. Strbak, O.; Dobrota, D. Archean Iron-Based Metabolism Analysis and the Photoferrotrophy-Driven Hypothesis of Microbial Magnetotaxis Origin. *Geomicrobiol. J.* **2019**, *36*, 278–290. [[CrossRef](#)]
9. Narayanan, S.; Shahbazian-Yassar, R.; Shokuhfar, T. Transmission electron microscopy of the iron oxide core in ferritin proteins: Current status and future directions. *J. Phys. D. Appl. Phys.* **2019**, *52*, 453001. [[CrossRef](#)]
10. Svobodova, H.; Kosnáč, D.; Tanila, H.; Wagner, A.; Trnka, M.; Vitovič, P.; Hlinkova, J.; Vavrinsky, E.; Ehrlich, H.; Polák, Š.; et al. Iron-oxide minerals in the human tissues. *Biometals* **2020**, *33*, 1–13. [[CrossRef](#)]
11. Grüttner, C.; Müller, K.; Teller, J.; Westphal, F. Synthesis and functionalisation of magnetic nanoparticles for hyperthermia applications. *Int. J. Hyperth.* **2013**, *29*, 777–789. [[CrossRef](#)] [[PubMed](#)]
12. Kment, Š.; Sivula, K.; Naldoni, A.; Sarmah, S.P.; Kmentová, H.; Kulkarni, M.; Rambabu, Y.; Schmuki, P.; Zbořil, R. FeO-based nanostructures and nanohybrids for photoelectrochemical water splitting. *Prog. Mater. Sci.* **2020**, *110*, 100632. [[CrossRef](#)]
13. Kralj, S.; Marchesan, S. Bioinspired Magnetic Nanochains for Medicine. *Pharmaceutics* **2021**, *13*, 1262. [[CrossRef](#)]
14. Tran, H.V.; Ngo, N.M.; Medhi, R.; Srinoi, P.; Liu, T.; Rittikulsittichai, S.; Lee, T.R. Multifunctional Iron Oxide Magnetic Nanoparticles for Biomedical Applications: A Review. *Materials* **2022**, *15*, 503. [[CrossRef](#)]
15. Lam, A.; Hyler, F.; Stagg, O.; Morris, K.; Shaw, S.; Velázquez, J.M.; Navrotsky, A. Synthesis and thermodynamics of uranium-incorporated α -Fe₂O₃ nanoparticles. *J. Nucl. Mater.* **2021**, *556*, 153172. [[CrossRef](#)]
16. Huber, S.E.; Mauracher, A.; Sukuba, I.; Urban, J.; Maihom, T.; Probst, M. Electron impact ionisation cross sections of iron oxides. *Eur. Phys. J. D* **2017**, *71*, 335. [[CrossRef](#)]
17. Fabrichnaya, O.; Saxena, S.K.; Richet, P.; Westrum, E.F. *Thermodynamic Data, Models, and Phase Diagrams in Multicomponent Oxide Systems: An Assessment for Materials and Planetary Scientists Based on Calorimetric, Volumetric and Phase Equilibrium Data*; Springer Science & Business Media: Berlin/Heidelberg, Germany, 2004; ISBN 978-3-642-08445-4.
18. Carter, C.B.; Norton, M.G. Equilibrium Phase Diagrams. In *Ceramic Materials*; Springer: New York, NY, USA, 2013; pp. 123–139. [[CrossRef](#)]
19. Machala, L.; Tuček, J.; Zbořil, R. Polymorphous transformations of nanometric iron(III) oxide: A review. *Chem. Mater.* **2011**, *23*, 3255–3272. [[CrossRef](#)]
20. Tuček, J.; Machala, L.; Ono, S.; Namai, A.; Yoshikiyo, M.; Imoto, K.; Tokoro, H.; Ohkoshi, S.I.; Zbořil, R. Zeta-Fe₂O₃—A new stable polymorph in iron(III) oxide family. *Sci. Rep.* **2015**, *5*, 15091. [[CrossRef](#)]
21. Kim, H.J. Short review on Fe₂O₃ polymorphs and ε -Fe₂O₃ thin films. *New Phys. Sae Mulli* **2018**, *68*, 819–828. [[CrossRef](#)]
22. Kerchich, S.; Boudjemaa, A.; Chebout, R.; Bachari, K.; Mameri, N. High performance of δ -Fe₂O₃ novel photo-catalyst supported on LDH structure. *J. Photochem. Photobiol. A Chem.* **2021**, *406*, 113001. [[CrossRef](#)]

23. Lavina, B.; Dera, P.; Kim, E.; Meng, Y.; Downs, R.T.; Weck, P.F.; Sutton, S.R.; Zhao, Y. Discovery of the recoverable high-pressure iron oxide Fe_4O_5 . *Proc. Natl. Acad. Sci. USA* **2011**, *108*, 17281–17285. [[CrossRef](#)]
24. Huang, S.; Hu, Q. Medium-range structure motifs of complex iron oxides. *J. Appl. Phys.* **2022**, *131*, 070902. [[CrossRef](#)]
25. Pereira, M.C.; Oliveira, L.C.A.; Murad, E. Iron oxide catalysts: Fenton and Fentonlike reactions—A review. *Clay Miner.* **2012**, *47*, 285–302. [[CrossRef](#)]
26. Pouran, S.R.R.; Raman, A.A.A.; Daud, W.M.A.W. Review on the application of modified iron oxides as heterogeneous catalysts in Fenton reactions. *J. Clean. Prod.* **2014**, *64*, 24–35. [[CrossRef](#)]
27. Mu, Y.; Jia, F.; Ai, Z.; Zhang, L. Iron oxide shell mediated environmental remediation properties of nano zero-valent iron. *Environ. Sci. Nano* **2017**, *4*, 27–45. [[CrossRef](#)]
28. Wu, Y.; Zhao, G.; Qi, H. Precipitation of magnetic iron oxide induced by *sporosarcina pasteurii* cells. *Microorganisms* **2021**, *9*, 331. [[CrossRef](#)]
29. Antone, A.J.; Sun, Z.; Bao, Y. Preparation and application of iron oxide nanoclusters. *Magnetochemistry* **2019**, *5*, 45. [[CrossRef](#)]
30. De Yoreo, J.J. In-situ liquid phase TEM observations of nucleation and growth processes. *Prog. Cryst. Growth Charact. Mater.* **2016**, *62*, 69–88. [[CrossRef](#)]
31. Faivre, D.; Godec, T.U. From bacteria to mollusks: The principles underlying the biomineralization of iron oxide materials. *Angew. Chem.-Int. Ed.* **2015**, *54*, 4728–4747. [[CrossRef](#)] [[PubMed](#)]
32. Fortin, D.; Langley, S. Formation and occurrence of biogenic iron-rich minerals. *Earth-Sci. Rev.* **2005**, *72*, 1–19. [[CrossRef](#)]
33. Obara, N.; Murao, R.; ShinOda, K.; Suzuki, S. Structural Changes of Minerals in Iron Ores via Aqueous Solution. *Tetsu-Hagane J. Iron Steel Inst. Jpn.* **2021**, *107*, 534–541. [[CrossRef](#)]
34. Fatimah, I.; Fadillah, G.; Yudha, S.P. Synthesis of iron-based magnetic nanocomposites: A review. *Arab. J. Chem.* **2021**, *14*, 103301. [[CrossRef](#)]
35. Ohkoshi, S.I.; Sakurai, S.; Jin, J.; Hashimoto, K. The addition effects of alkaline earth ions in the chemical synthesis of ε - Fe_2O_3 nanocrystals that exhibit a huge coercive field. *J. Appl. Phys.* **2005**, *97*, 10K312. [[CrossRef](#)]
36. Ohkoshi, S.I.; Tokoro, H. Hard magnetic ferrite: ε - Fe_2O_3 . *Bull. Chem. Soc. Jpn.* **2013**, *86*, 897–907. [[CrossRef](#)]
37. Testov, D.O.; Gareev, K.G.; Khmelnitskiy, I.K.; Kosterov, A.; Surovitskii, L.; Luchinin, V.V. Influence of the Preparation Technique on the Magnetic Characteristics of ε - Fe_2O_3 -Based Composites. *Magnetochemistry* **2023**, *9*, 10. [[CrossRef](#)]
38. Kharitonskii, P.; Kamzin, A.; Gareev, K.; Valiullin, A.; Vezo, O.; Sergienko, E.; Korolev, D.; Kosterov, A.; Lebedev, S.; Gurylev, A.; et al. Magnetic granulometry and Mössbauer spectroscopy of $\text{Fe}_m\text{O}_n\text{-SiO}_2$ colloidal nanoparticles. *J. Magn. Magn. Mater.* **2018**, *461*, 30–36. [[CrossRef](#)]
39. Machala, L.; Zboril, R.; Gedanken, A. Amorphous iron(III) oxide—A review. *J. Phys. Chem. B* **2007**, *111*, 4003–4018. [[CrossRef](#)] [[PubMed](#)]
40. Liu, H.; Han, W.; Huo, C.; Cen, Y. Development and application of wüstite-based ammonia synthesis catalysts. *Catal. Today* **2020**, *355*, 110–127. [[CrossRef](#)]
41. Sakurai, S.; Namai, A.; Hashimoto, K.; Ohkoshi, S. First Observation of Phase Transformation of All Four Fe_2O_3 Phases ($\gamma \rightarrow \varepsilon \rightarrow \beta \rightarrow \alpha$ -Phase). *J. Am. Chem. Soc.* **2009**, *131*, 18299–18303. [[CrossRef](#)] [[PubMed](#)]
42. Yin, M.; Chen, Z.; Deegan, B.; O'Brien, S. Wüstite nanocrystals: Synthesis, structure and superlattice formation. *J. Mater. Res.* **2007**, *22*, 1987–1995. [[CrossRef](#)]
43. Zhang, Z.; Satpathy, S. Electron states, magnetism, and the Verwey transition in magnetite. *Phys. Rev. B* **1991**, *44*, 13319–13331. [[CrossRef](#)]
44. Yadav, A.A.; Deshmukh, T.B.; Deshmukh, R.V.; Patil, D.D.; Chavan, U.J. Electrochemical supercapacitive performance of Hematite α - Fe_2O_3 thin films prepared by spray pyrolysis from non-aqueous medium. *Thin Solid Films* **2016**, *616*, 351–358. [[CrossRef](#)]
45. Roca, A.G.; Marco, J.F.; Del Puerto Morales, M.; Serna, C.J. Effect of nature and particle size on properties of uniform magnetite and maghemite nanoparticles. *J. Phys. Chem. C* **2007**, *111*, 18577–18584. [[CrossRef](#)]
46. Jin, J.; Ohkoshi, S.I.; Hashimoto, K. Giant Coercive Field of Nanometer-Sized Iron Oxide. *Adv. Mater.* **2004**, *16*, 48–51. [[CrossRef](#)]
47. Schrettle, F.; Kant, C.; Lunkenheimer, P.; Mayr, F.; Deisenhofer, J.; Loidl, A. Wüstite: Electric, thermodynamic and optical properties of FeO . *Eur. Phys. J. B* **2012**, *85*, 164. [[CrossRef](#)]
48. Faure, B.; Salazar-Alvarez, G.; Bergström, L. Hamaker constants of iron oxide nanoparticles. *Langmuir* **2011**, *27*, 8659–8664. [[CrossRef](#)] [[PubMed](#)]
49. Gomaa, M.M. Forward and inverse modelling of the electrical properties of magnetite intruded by magma, Egypt. *Geophys. J. Int.* **2013**, *194*, 1527–1540. [[CrossRef](#)]
50. Lunt, R.A.; Jackson, A.J.; Walsh, A. Dielectric response of Fe_2O_3 crystals and thin films. *Chem. Phys. Lett.* **2013**, *586*, 67–69. [[CrossRef](#)]
51. Ghigna, T.; Zannoni, M.; Jones, M.E.; Simonetto, A. Permittivity and permeability of epoxy-magnetite powder composites at microwave frequencies. *J. Appl. Phys.* **2020**, *127*, 045102. [[CrossRef](#)]
52. Bhavani, P.; Reddy, N.R.; Reddy, I.V.S. Synthesis and physical characterization of γ - Fe_2O_3 and $(\alpha + \gamma)$ - Fe_2O_3 nanoparticles. *J. Korean Phys. Soc.* **2017**, *70*, 150–154. [[CrossRef](#)]
53. Gich, M.; Frontera, C.; Roig, A.; Fontcuberta, J.; Molins, E.; Bellido, N.; Simon, C.; Fleta, C. Magnetoelectric coupling in ε - Fe_2O_3 nanoparticles. *Nanotechnology* **2006**, *17*, 687. [[CrossRef](#)]

54. Dubrovskiy, A.A.; Balaev, D.A.; Krasikov, A.A.; Yakushhkin, S.S.; Kirillov, V.L.; Martyanov, O.N. Magnetodielectric effect in a metamaterial consisting of xerogel with embedded ϵ -Fe₂O₃ iron oxide nanoparticles. *Solid State Commun.* **2019**, *289*, 27–29. [[CrossRef](#)]
55. Gheisari, M.; Mozaffari, M.; Acet, M.; Amighian, J. Preparation and investigation of magnetic properties of wüstite nanoparticles. *J. Magn. Magn. Mater.* **2008**, *320*, 2618–2621. [[CrossRef](#)]
56. Chen, C.J.; Chiang, R.K.; Lai, H.Y.; Lin, C.R. Characterization of monodisperse wüstite nanoparticles following partial oxidation. *J. Phys. Chem. C* **2010**, *114*, 4258–4263. [[CrossRef](#)]
57. Özdemir, Ö. Coercive force of single crystals of magnetite at low temperatures. *Geophys. J. Int.* **2000**, *141*, 351–356. [[CrossRef](#)]
58. Tadic, M.; Panjan, M.; Tadic, B.V.; Lazovic, J.; Damnjanovic, V.; Kopani, M.; Kopanja, L. Magnetic properties of hematite (α -Fe₂O₃) nanoparticles synthesized by sol-gel synthesis method: The influence of particle size and particle size distribution. *J. Electr. Eng.* **2019**, *70*, 71–76. [[CrossRef](#)]
59. Araujo, R.N.; Nascimento, E.P.; Raimundo, R.A.; Macedo, D.A.; Mastelaro, V.R.; Neves, G.A.; Morales, M.A.; Menezes, R.R. Hybrid hematite/calcium ferrite fibers by solution blow spinning: Microstructural, optical and magnetic characterization. *Ceram. Int.* **2021**, *47*, 33363–33372. [[CrossRef](#)]
60. Mirza, I.M.; Ali, K.; Sarfraz, A.K.; Ali, A.; Haq, A.U. A study of dielectric, optical and magnetic characteristics of maghemite nanocrystallites. *Mater. Chem. Phys.* **2015**, *164*, 183–187. [[CrossRef](#)]
61. Shokrollahi, H. A review of the magnetic properties, synthesis methods and applications of maghemite. *J. Magn. Magn. Mater.* **2017**, *426*, 74–81. [[CrossRef](#)]
62. Danno, T.; Nakatsuka, D.; Kusano, Y.; Asaoka, H.; Nakanishi, M.; Fujii, T.; Ikeda, Y.; Takada, J. Crystal structure of β -Fe₂O₃ and topotactic phase transformation to α -Fe₂O₃. *Cryst. Growth Des.* **2013**, *13*, 770–774. [[CrossRef](#)]
63. Kumar, A.; Singhal, A. Synthesis of colloidal β -Fe₂O₃ nanostructures—Influence of addition of Co²⁺ on their morphology and magnetic behavior. *Nanotechnology* **2007**, *18*, 475703. [[CrossRef](#)]
64. Malina, O.; Tuček, J.; Jakubec, P.; Kašlík, J.; Medřík, I.; Tokoro, H.; Yoshiakiyo, M.; Namai, A.; Ohkoshi, S.I.; Zbořil, R. Magnetic ground state of nanosized β -Fe₂O₃ and its remarkable electronic features. *RSC Adv.* **2015**, *5*, 49719–49727. [[CrossRef](#)]
65. Zhang, N.; Wang, X.; Feng, J.; Huang, H.; Guo, Y.; Li, Z.; Zou, Z. Paving the road toward the use of β -Fe₂O₃ in solar water splitting: Raman identification, phase transformation and strategies for phase stabilization. *Natl. Sci. Rev.* **2020**, *7*, 1059–1067. [[CrossRef](#)]
66. Levy, D.; Giustetto, R.; Hoser, A. Structure of magnetite (Fe₃O₄) above the Curie temperature: A cation ordering study. *Phys. Chem. Miner.* **2012**, *39*, 169–176. [[CrossRef](#)]
67. Özdemir, Ö.; Banerjee, S.K. High temperature stability of maghemite (γ -Fe₂O₃). *Geophys. Res. Lett.* **1984**, *11*, 161–164. [[CrossRef](#)]
68. Jordan, K.; Cazacu, A.; Manai, G.; Ceballos, S.F.; Murphy, S.; Shvets, I.V. Scanning tunneling spectroscopy study of the electronic structure of Fe₃O₄ surfaces. *Phys. Rev. B—Condens. Matter Mater. Phys.* **2006**, *74*, 085416. [[CrossRef](#)]
69. Liu, H.; Di Valentin, C. Band Gap in Magnetite above Verwey Temperature Induced by Symmetry Breaking. *J. Phys. Chem. C* **2017**, *121*, 25736–25742. [[CrossRef](#)]
70. Bowker, M.; Hutchings, G.; Davies, P.R.; Edwards, D.; Davies, R.; Shaikhutdinov, S.; Freund, H.J. Surface structure of γ -Fe₂O₃(111). *Surf. Sci.* **2012**, *606*, 1594–1599. [[CrossRef](#)]
71. Silva, M.F.; De Oliveira, L.A.S.; Ciciliati, M.A.; Silva, L.T.; Pereira, B.S.; Hechenleitner, A.A.W.; Oliveira, D.M.F.; Pirota, K.R.; Ivashita, F.F.; Paesano, A.; et al. Nanometric particle size and phase controlled synthesis and characterization of γ -Fe₂O₃ or (α + γ)-Fe₂O₃ by a modified sol-gel method. *J. Appl. Phys.* **2013**, *114*, 104311. [[CrossRef](#)]
72. Elouafi, A.; Moubah, R.; Tiziouine, A.; Derkaoui, S.; Omari, L.H.; Lassri, H. Effects of Ru doping and of oxygen vacancies on the optical properties in α -Fe₂O₃ powders. *Appl. Phys. A Mater. Sci. Process.* **2020**, *126*, 228. [[CrossRef](#)]
73. Nasu, T.; Yoshiakiyo, M.; Tokoro, H.; Namai, A.; Ohkoshi, S.I. First-Principles Calculations and Optical Absorption Spectrum of a Light-Colored Aluminum-Substituted ϵ -Iron Oxide Magnet. *Eur. J. Inorg. Chem.* **2017**, *2017*, 531–534. [[CrossRef](#)]
74. Dadashi, S.; Poursalehi, R.; Delavari, H. Structural and Optical Properties of Pure Iron and Iron Oxide Nanoparticles Prepared via Pulsed Nd:YAG Laser Ablation in Liquid. *Procedia Mater. Sci.* **2015**, *11*, 722–726. [[CrossRef](#)]
75. Feld, A.; Weimer, A.; Kornowski, A.; Winckelmans, N.; Merkl, J.P.; Kloust, H.; Zierold, R.; Schmidtke, C.; Schotten, T.; Riedner, M.; et al. Chemistry of Shape-Controlled Iron Oxide Nanocrystal Formation. *ACS Nano* **2019**, *13*, 152–162. [[CrossRef](#)] [[PubMed](#)]
76. Kampferbeck, M.; Klauke, L.R.; Weller, H.; Vossmeyer, T. Little Adjustments Significantly Simplify the Gram-Scale Synthesis of High-Quality Iron Oxide Nanocubes. *Langmuir* **2021**, *37*, 9851–9857. [[CrossRef](#)] [[PubMed](#)]
77. Marinca, T.F.; Chicinaş, H.F.; Neamtu, B.V.; Isnard, O.; Pascuta, P.; Lupu, N.; Stoian, G.; Chicinaş, I. Mechanosynthesis, structural, thermal and magnetic characteristics of oleic acid coated Fe₃O₄ nanoparticles. *Mater. Chem. Phys.* **2016**, *171*, 336–345. [[CrossRef](#)]
78. Leszczyński, B.; Hadjipanayis, G.C.; El-Gendy, A.A.; Załęski, K.; Śniadecki, Z.; Musiał, A.; Jarek, M.; Jurga, S.; Skumiel, A. The influence of oxidation process on exchange bias in egg-shaped FeO/Fe₃O₄ core/shell nanoparticles. *J. Magn. Magn. Mater.* **2016**, *416*, 269–274. [[CrossRef](#)]
79. Narnaware, P.K.; Ravikumar, C. Mechanistic Insights into the Formation and Growth of Anisotropic-Shaped Wüstite-Spinel Core-Shell Iron Oxide Nanoparticles in a Coordinating Solvent. *J. Phys. Chem. C* **2020**, *124*, 25010–25027. [[CrossRef](#)]
80. Kluge, S.; Deng, L.; Feroughi, O.; Schneider, F.; Poliak, M.; Fomin, A.; Tsionsky, V.; Cheskis, S.; Wlokas, I.; Rahinov, I.; et al. Initial reaction steps during flame synthesis of iron-oxide nanoparticles. *CrystEngComm* **2015**, *17*, 6930–6939. [[CrossRef](#)]

81. Ahn, T.; Kim, J.H.; Yang, H.M.; Lee, J.W.; Kim, J.D. Formation pathways of magnetite nanoparticles by coprecipitation method. *J. Phys. Chem. C* **2012**, *116*, 6069–6076. [[CrossRef](#)]
82. Besenhard, M.O.; LaGrow, A.P.; Hodzic, A.; Kriechbaum, M.; Panariello, L.; Bais, G.; Loizou, K.; Damilos, S.; Cruz, M.M.; Thanh, N.T.K.; et al. Co-precipitation synthesis of stable iron oxide nanoparticles with NaOH: New insights and continuous production via flow chemistry. *Chem. Eng. J.* **2020**, *399*, 125740. [[CrossRef](#)]
83. Chen, Y.; Zhang, J.; Wang, Z.; Zhou, Z. Solvothermal synthesis of size-controlled monodispersed superparamagnetic iron oxide nanoparticles. *Appl. Sci.* **2019**, *9*, 5157. [[CrossRef](#)]
84. Grabs, I.M.; Bradtmöller, C.; Menzel, D.; Garnweitner, G. Formation mechanisms of iron oxide nanoparticles in different nonaqueous media. *Cryst. Growth Des.* **2012**, *12*, 1469–1475. [[CrossRef](#)]
85. Kozakova, Z.; Kuritka, I.; Kazantseva, N.E.; Babayan, V.; Pastorek, M.; Machovsky, M.; Bazant, P.; Saha, P. The formation mechanism of iron oxide nanoparticles within the microwave-assisted solvothermal synthesis and its correlation with the structural and magnetic properties. *Dalton Trans.* **2015**, *44*, 21099–21108. [[CrossRef](#)]
86. Lozano, I.; Casillas, N.; de León, C.P.; Walsh, F.C.; Herrasti, P. New Insights into the Electrochemical Formation of Magnetite Nanoparticles. *J. Electrochem. Soc.* **2017**, *164*, D184–D191. [[CrossRef](#)]
87. Kertmen, A.; Torruella, P.; Coy, E.; Yate, L.; Nowaczyk, G.; Gapiński, J.; Vogt, C.; Toprak, M.; Estradé, S.; Peiró, F.; et al. Acetate-Induced Disassembly of Spherical Iron Oxide Nanoparticle Clusters into Monodispersed Core-Shell Structures upon Nanoemulsion Fusion. *Langmuir* **2017**, *33*, 10351–10365. [[CrossRef](#)]
88. Nene, A.; Takahashi, M.; Somani, P.R. Fe_3O_4 and Fe Nanoparticles by Chemical Reduction of $\text{Fe}(\text{acac})_3$ by Ascorbic Acid: Role of Water. *World J. Nano Sci. Eng.* **2016**, *6*, 20–28. [[CrossRef](#)]
89. Perecin, C.J.; Tirich, B.M.; Nagamine, L.C.C.M.; Porto, G.; Rocha, F.V.; Cerize, N.N.P.; Varanda, L.C. Aqueous synthesis of magnetite nanoparticles for magnetic hyperthermia: Formation mechanism approach, high water-dispersity and stability. *Colloids Surf. A Physicochem. Eng. Asp.* **2021**, *627*, 127169. [[CrossRef](#)]
90. Tahir, A.; Saeed, A.; Ramzan, I.; Hayat, S.S.; Ahmad, W.; Naeem, S.; Afzal, M.; Mukhtar, A.; Mehmood, T.; Khan, B.S. Mechanism for the formation of magnetite iron oxide nanostructures by *Ficus carica* dried fruit extract using green synthesis method. *Appl. Nanosci.* **2021**, *11*, 1857–1865. [[CrossRef](#)]
91. Gan, L.; Lu, Z.; Cao, D.; Chen, Z. Effects of cetyltrimethylammonium bromide on the morphology of green synthesized Fe_3O_4 nanoparticles used to remove phosphate. *Mater. Sci. Eng. C* **2018**, *82*, 41–45. [[CrossRef](#)]
92. Kashyap, S.; Woehl, T.J.; Liu, X.; Mallapragada, S.K.; Prozorov, T. Nucleation of iron oxide nanoparticles mediated by mms6 protein in situ. *ACS Nano* **2014**, *8*, 9097–9106. [[CrossRef](#)]
93. Baaziz, W.; Ghica, C.; Cypriano, J.; Abreu, F.; Anselme, K.; Ersen, O.; Farina, M.; Werckmann, J. New phenotype and mineralization of biogenic iron oxide in magnetotactic bacteria. *Nanomaterials* **2021**, *11*, 3189. [[CrossRef](#)] [[PubMed](#)]
94. Ben-Shimon, S.; Stein, D.; Zarivach, R. Current view of iron biomineralization in magnetotactic bacteria. *J. Struct. Biol. X* **2021**, *5*, 100052. [[CrossRef](#)]
95. Lovley, D.R.; Stoltz, J.F.; Nord, G.L.; Phillips, E.J.P. Anaerobic production of magnetite by a dissimilatory iron-reducing microorganism. *Nature* **1987**, *330*, 252–254. [[CrossRef](#)]
96. Garber, A.I.; Cohen, A.B.; Nealson, K.H.; Ramírez, G.A.; Barco, R.A.; Enzingmüller-Bleyl, T.C.; Gehringer, M.M.; Merino, N. Metagenomic Insights into the Microbial Iron Cycle of Subseafloor Habitats. *Front. Microbiol.* **2021**, *12*, 667944. [[CrossRef](#)] [[PubMed](#)]
97. Staniland, S.; Ward, B.; Harrison, A.; Van Der Laan, G.; Telling, N. Rapid magnetosome formation shown by real-time X-ray magnetic circular dichroism. *Proc. Natl. Acad. Sci. USA* **2007**, *104*, 19524–19528. [[CrossRef](#)] [[PubMed](#)]
98. Rahn-Lee, L.; Komeili, A. The magnetosome model: Insights into the mechanisms of bacterial biomineratization. *Front. Microbiol.* **2013**, *4*, 352. [[CrossRef](#)]
99. Hu, X.; Chen, H.; Beaudoin, G.; Zhang, Y. Textural and compositional evolution of iron oxides at Mina Justa (Peru): Implications for mushketovite and formation of IOCG deposits. *Am. Mineral.* **2020**, *105*, 397–408. [[CrossRef](#)]
100. Hua, X.; Zheng, Y.; Xu, Q.; Lu, X.; Cheng, H.; Zou, X.; Song, Q.; Ning, Z. Interfacial reactions of chalcopyrite in ammonia-ammonium chloride solution. *Trans. Nonferrous Met. Soc. China Engl. Ed.* **2018**, *28*, 556–566. [[CrossRef](#)]
101. Velasco, F.; Tornos, F.; Hanchar, J.M. Immiscible iron- and silica-rich melts and magnetite geochemistry at the El Laco volcano (northern Chile): Evidence for a magmatic origin for the magnetite deposits. *Ore Geol. Rev.* **2016**, *79*, 346–366. [[CrossRef](#)]
102. Warrier, A.K.; Sebastian, J.G.; Amrutha, K.; Sali, A.S.Y.; Mahesh, B.S.; Mohan, R. Magnetic properties of surface sediments in Schirmacher Oasis, East Antarctica: Spatial distribution and controlling factors. *J. Soils Sediments* **2021**, *21*, 1206–1221. [[CrossRef](#)]
103. Dodd, M.S.; Wang, H.; Li, C.; Towner, M.; Thomson, A.R.; Slack, J.F.; Wan, Y.S.; Pirajno, F.; Manikyamba, C.; Wang, Q.; et al. Abiotic anoxic iron oxidation, formation of Archean banded iron formations, and the oxidation of early Earth. *Earth Planet. Sci. Lett.* **2022**, *584*, 117469. [[CrossRef](#)]
104. Yang, X.; Guo, Q.; Boyko, V.; Avetisyan, K.; Findlay, A.J.; Huang, F.; Wang, Z.; Chen, Z. Isotopic reconstruction of iron oxidation-reduction process based on an Archean Ocean analogue. *Sci. Total Environ.* **2022**, *817*, 152609. [[CrossRef](#)]
105. Xiong, X.; Liu, X.; Tan, H.; Deng, S. Investigation on high temperature corrosion of water-cooled wall tubes at a 300 MW boiler. *J. Energy Inst.* **2020**, *93*, 377–386. [[CrossRef](#)]
106. Martinelli, L.; Balbaud-Célérier, F.; Terlain, A.; Bosonnet, S.; Picard, G.; Santarini, G. Oxidation mechanism of an Fe-9Cr-1Mo steel by liquid Pb-Bi eutectic alloy at 470 °C (Part II). *Corros. Sci.* **2008**, *50*, 2537–2548. [[CrossRef](#)]

107. Misawa, T.; Hashimoto, K.; Shimodaira, S. The mechanism of formation of iron oxide and oxyhydroxides in aqueous solutions at room temperature. *Corros. Sci.* **1974**, *14*, 131–149. [\[CrossRef\]](#)
108. Odziemkowski, M.S.; Schuhmacher, T.T.; Gillham, R.W.; Reardon, E.J. Mechanism of oxide film formation on iron in simulating groundwater solutions: Raman spectroscopic studies. *Corros. Sci.* **1998**, *40*, 371–389. [\[CrossRef\]](#)
109. Liu, M.; Cheng, X.; Li, X.; Pan, Y.; Li, J. Effect of Cr on the passive film formation mechanism of steel rebar in saturated calcium hydroxide solution. *Appl. Surf. Sci.* **2016**, *389*, 1182–1191. [\[CrossRef\]](#)
110. Castro-Ocampo, O.; Celaya, C.A.; González-Reyes, L.; Hernández-Pérez, I.; Garibay-Febles, V.; Jaramillo-Quintero, O.A.; Lara-García, H.A.; Muñiz, J.; Suárez-Parra, R. Understanding hydroxyl radicals addition to CO₂ on α -Fe₂O₃(1 1 0) surface photocatalyst for organic compounds production. *Fuel* **2022**, *310*, 122465. [\[CrossRef\]](#)
111. Kusior, A.; Michalec, K.; Jelen, P.; Radecka, M. Shaped Fe₂O₃ nanoparticles-synthesis and enhanced photocatalytic degradation towards RhB. *Appl. Surf. Sci.* **2019**, *476*, 342–352. [\[CrossRef\]](#)
112. Sivarajani, R.; Thayumanavan, A.; Sriram, S. Photocatalytic activity of Zn-doped Fe₂O₃ nanoparticles: A combined experimental and theoretical study. *Bull. Mater. Sci.* **2019**, *42*, 185. [\[CrossRef\]](#)
113. Shkrob, I.A.; Chemerisov, S.D.; Marin, T.W. Photocatalytic decomposition of carboxylated molecules on light-exposed martian regolith and its relation to methane production on mars. *Astrobiology* **2010**, *10*, 425–436. [\[CrossRef\]](#) [\[PubMed\]](#)
114. Bolanz, R.M.; Bläss, U.; Ackermann, S.; Ciobotă, V.; Rösch, P.; Tarcea, N.; Popp, J.; Majzlan, J. The effect of antimonate, arsenate, and phosphate on the transformation of ferrihydrite to goethite, hematite, feroxyhyte, and tripuhyite. *Clays Clay Miner.* **2013**, *61*, 11–25. [\[CrossRef\]](#)
115. Börsig, N.; Scheinost, A.C.; Shaw, S.; Schild, D.; Neumann, T. Uptake mechanisms of selenium oxyanions during the ferrihydrite-hematite recrystallization. *Geochim. Cosmochim. Acta* **2017**, *206*, 236–253. [\[CrossRef\]](#)
116. Brandt, F.; Schäfer, T.; Claret, F.; Bosbach, D. Heterogeneous formation of ferric oxide nanoparticles on chlorite surfaces studied by X-ray absorption spectromicroscopy (STXM). *Chem. Geol.* **2012**, *329*, 42–52. [\[CrossRef\]](#)
117. Chan, M.A.; Johnson, C.M.; Beard, B.L.; Bowman, J.R.; Parry, W.T. Iron isotopes constrain the pathways and formation mechanisms of terrestrial oxide concretions: A tool for tracing iron cycling on Mars? *Geosphere* **2006**, *2*, 324–332. [\[CrossRef\]](#)
118. Chan, M.A.; Ormö, J.; Park, A.J.; Stich, M.; Souza-Egipsy, V.; Komatsu, G. Models of iron oxide concretion formation: Field, numerical, and laboratory comparisons. *Geofluids* **2007**, *7*, 356–368. [\[CrossRef\]](#)
119. Gao, B.F.; Wu, C.Z.; Yang, T.; Santosh, M.; Dong, L.H.; Zhao, T.Y.; Ye, H.; Lei, R.X.; Li, W. The Neoproterozoic “Blood Falls” in Tarim Craton and Their Possible Connection With Snowball Earth. *J. Geophys. Res. Earth Surf.* **2019**, *124*, 229–244. [\[CrossRef\]](#)
120. Magnol, R.V.; Macedo, M.Q.; de Macêdo, M.C.S.; Scandian, C. Tribological characterization of jaspilite by linear scratch test. *Wear* **2019**, *426–427*, 142–150. [\[CrossRef\]](#)
121. Rasmussen, B.; Muhling, J.R. Development of a greenalite–silica shuttle during incursions of hydrothermal vent plumes onto Neoarchean shelf, Hamersley region, Australia. *Precambrian Res.* **2021**, *353*, 106003. [\[CrossRef\]](#)
122. Parker, C.W.; Wolf, J.A.; Auler, A.S.; Barton, H.A.; Senko, J.M. Microbial reducibility of Fe(III) phases associated with the genesis of iron ore caves in the Iron Quadrangle, Minas Gerais, Brazil. *Minerals* **2013**, *3*, 395–411. [\[CrossRef\]](#)
123. Wu, Z.; Yuan, L.; Jia, N.; Wang, Y.; Sun, L. Microbial biomineralization of iron seepage water: Implication for the iron ores formation in intertidal zone of Zhoushan Archipelago, East China Sea. *Geochem. J.* **2009**, *43*, 167–177. [\[CrossRef\]](#)
124. Singh, M.; Singhal, J.; Prasad, K.A.; Rajesh, V.J.; Ray, D.; Sahoo, P. Spectral characteristics of banded iron formations in Singhbhum craton, eastern India: Implications for hematite deposits on Mars. *Geosci. Front.* **2016**, *7*, 927–936. [\[CrossRef\]](#)
125. Bandi, S.; Srivastav, A.K. Understanding the Growth Mechanism of Hematite Nanoparticles: The Role of Maghemite as an Intermediate Phase. *Cryst. Growth Des.* **2021**, *21*, 16–22. [\[CrossRef\]](#)
126. Gallo-Cordova, A.; Ovejero, J.G.; Pablo-Sainz-Ezquerro, A.M.; Cuya, J.; Jeyadevan, B.; Veintemillas-Verdaguer, S.; Tartaj, P.; Morales, M.D.P. Unravelling an amine-regulated crystallization crossover to prove single/multicore effects on the biomedical and environmental catalytic activity of magnetic iron oxide colloids. *J. Colloid Interface Sci.* **2022**, *608*, 1585–1597. [\[CrossRef\]](#) [\[PubMed\]](#)
127. Gavilán, H.; Sánchez, E.H.; Brollo, M.E.F.; Asín, L.; Moerner, K.K.; Frandsen, C.; Lázaro, F.J.; Serna, C.J.; Veintemillas-Verdaguer, S.; Morales, M.P.; et al. Formation Mechanism of Maghemite Nanoflowers Synthesized by a Polyol-Mediated Process. *ACS Omega* **2017**, *2*, 7172–7184. [\[CrossRef\]](#)
128. Jensen, K.M.Ø.; Andersen, H.L.; Tyrsted, C.; Bøjesen, E.D.; Dippel, A.C.; Lock, N.; Billinge, S.J.L.; Iversen, B.B.; Christensen, M. Mechanisms for iron oxide formation under hydrothermal conditions: An in situ total scattering study. *ACS Nano* **2014**, *8*, 10704–10714. [\[CrossRef\]](#)
129. Kabelitz, A.; Guilherme, A.; Joester, M.; Reinholz, U.; Radtke, M.; Bienert, R.; Schulz, K.; Schmack, R.; Krahnert, R.; Emmerling, F. Time-resolved in situ studies on the formation mechanism of iron oxide nanoparticles using combined fast-XANES and SAXS. *CrystEngComm* **2015**, *17*, 8463–8470. [\[CrossRef\]](#)
130. Bhattacharya, S.; Roychowdhury, A.; Das, D.; Nayar, S. Multi-functional biomimetic graphene induced transformation of Fe₃O₄ to ϵ -Fe₂O₃ at room temperature. *RSC Adv.* **2015**, *5*, 89488–89497. [\[CrossRef\]](#)
131. Královec, K.; Havelek, R.; Koutová, D.; Veverka, P.; Kubíčková, L.; Brázda, P.; Kohout, J.; Herynek, V.; Vosmanská, M.; Kaman, O. Magnetic nanoparticles of Ga-substituted ϵ -Fe₂O₃ for biomedical applications: Magnetic properties, transverse relaxivity, and effects of silica-coated particles on cytoskeletal networks. *J. Biomed. Mater. Res.—Part A* **2020**, *108*, 1563–1578. [\[CrossRef\]](#) [\[PubMed\]](#)

132. Dejoie, C.; Sciau, P.; Li, W.; Noé, L.; Mehta, A.; Chen, K.; Luo, H.; Kunz, M.; Tamura, N.; Liu, Z. Learning from the past: Rare ϵ - Fe_2O_3 in the ancient black-glazed Jian (Tenmoku) wares. *Sci. Rep.* **2014**, *4*, 4941. [[CrossRef](#)]
133. Ma, J.; Wang, Y.; Chen, K. Refining single-crystalline epsilon iron oxide nanorods via low-temperature aging. *Adv. Powder Technol.* **2019**, *30*, 3021–3027. [[CrossRef](#)]
134. Gurylev, A.; Kharitonskii, P.; Kosterov, A.; Berestnev, I.; Sergienko, E. Magnetic properties of fired clay (bricks) possibly containing epsilon iron (III) oxide. In *Journal of Physics: Conference Series*; IOP Publishing: Bristol, UK, 2019; Volume 1347. [[CrossRef](#)]
135. López-Sánchez, J.; Palencia-Ortas, A.; del Campo, A.; McIntosh, G.; Kovacheva, M.; Martín-Hernández, F.; Carmona, N.; de la Fuente, O.R.; Marín, P.; Molina-Cardín, A.; et al. Further progress in the study of epsilon iron oxide in archaeological baked clays. *Phys. Earth Planet. Inter.* **2020**, *307*, 106554. [[CrossRef](#)]
136. Corbellini, L.; Lacroix, C.; Harnagea, C.; Korinek, A.; Botton, G.A.; Ménard, D.; Pignolet, A. Epitaxially stabilized thin films of ϵ - Fe_2O_3 (001) grown on YSZ (100). *Sci. Rep.* **2017**, *7*, 3712. [[CrossRef](#)] [[PubMed](#)]
137. Kiyokawa, T.; Ikenaga, N. Oxidative dehydrogenation of n-butene to buta-1,3-diene with novel iron oxide-based catalyst: Effect of iron oxide crystalline structure. *Mol. Catal.* **2021**, *507*, 111560. [[CrossRef](#)]
138. López-Sánchez, J.; McIntosh, G.; Osete, M.L.; del Campo, A.; Villalaín, J.J.; Pérez, L.; Kovacheva, M.; de la Fuente, O.R. Epsilon iron oxide: Origin of the high coercivity stable low Curie temperature magnetic phase found in heated archeological materials. *Geochem. Geophys. Geosystems* **2017**, *18*, 2646–2656. [[CrossRef](#)]
139. Kosterov, A.; Kovacheva, M.; Kostadinova-Avramova, M.; Minaev, P.; Salnaia, N.; Surovitskii, L.; Yanson, S.; Sergienko, E.; Kharitonskii, P. High-coercivity magnetic minerals in archaeological baked clay and bricks. *Geophys. J. Int.* **2021**, *224*, 1256–1271. [[CrossRef](#)]
140. Tao, S.; Liu, S.; Yuan, Y.; Dong, J.; Li, Q. A Microstructural and Compositional Study of ϵ - Fe_2O_3 Crystals in the Hare's Fur Jian Ware. *Crystals* **2022**, *12*, 367. [[CrossRef](#)]
141. Jeon, B.; Van Overmeere, Q.; Van Duin, A.C.T.; Ramanathan, S. Nanoscale oxidation and complex oxide growth on single crystal iron surfaces and external electric field effects. *Phys. Chem. Chem. Phys.* **2013**, *15*, 1821–1830. [[CrossRef](#)]
142. Jiang, Y.; Bu, S.; Zhou, D.; Shi, X.; Pan, F.; Ji, Q.; Niu, T. Two-Dimensional Iron Oxide on Au(111): Growth Mechanism and Interfacial Properties. *J. Phys. Chem. C* **2021**, *125*, 24755–24763. [[CrossRef](#)]
143. Menecier, S.; Valette, S.; Denoirjean, P.; Lefort, P. Invar oxidation in CO₂:Kinetics and mechanism of formation of a wustite layer. *J. Therm. Anal. Calorim.* **2012**, *107*, 607–616. [[CrossRef](#)]
144. Prabowo, S.W.; Longbottom, R.J.; Monaghan, B.J.; del Puerto, D.; Ryan, M.J.; Bumby, C.W. Phase transformations during fluidized bed reduction of New Zealand titanomagnetite ironsand in hydrogen gas. *Powder Technol.* **2022**, *398*, 117032. [[CrossRef](#)]
145. Tanaka, R.; Sakamaki, T.; Ohtani, E.; Fukui, H.; Kamada, S.; Suzuki, A.; Tsutsui, S.; Uchiyama, H.; Baron, A.Q.R. The sound velocity of wüstite at high pressures: Implications for low-velocity anomalies at the base of the lower mantle. *Prog. Earth Planet. Sci.* **2020**, *7*, 23. [[CrossRef](#)]
146. Wang, M.; Kobayashi, Y.; Endo, R.; Susa, M. Formation kinetics of iron oxide in mould flux during continuous casting. *ISIJ Int.* **2013**, *53*, 56–61. [[CrossRef](#)]
147. Wei, Z.; Zhang, J.; Qin, B.; Dong, Y.; Lu, Y.; Li, Y.; Hao, W.; Zhang, Y. Reduction kinetics of hematite ore fines with H₂ in a rotary drum reactor. *Powder Technol.* **2018**, *332*, 18–26. [[CrossRef](#)]
148. Chen, Z.; Chou, K.C.; Morita, K. Mechanism of metastable Wüstite formation in the reduction process of iron oxide below 570 °C. *Mater. Trans.* **2016**, *57*, 1660–1663. [[CrossRef](#)]
149. Vasylkiv, O.; Bezidorozhev, O.; Sakka, Y. Synthesis of iron oxide nanoparticles with different morphologies by precipitation method with and without chitosan addition. *J. Ceram. Soc. Jpn.* **2016**, *124*, 489–494. [[CrossRef](#)]
150. Manikandan, A.; Vijaya, J.J.; Mary, J.A.; Kennedy, L.J.; Dinesh, A. Structural, optical and magnetic properties of Fe₃O₄ nanoparticles prepared by a facile microwave combustion method. *J. Ind. Eng. Chem.* **2014**, *20*, 2077–2085. [[CrossRef](#)]
151. Cabrera, L.; Gutierrez, S.; Menendez, N.; Morales, M.P.; Herrasti, P. Magnetite nanoparticles: Electrochemical synthesis and characterization. *Electrochim. Acta* **2008**, *53*, 3436–3441. [[CrossRef](#)]
152. Kim, D.W.; Kim, T.H.; Choi, S.; Kim, K.S.; Park, D.W. Preparation of silica coated iron oxide nanoparticles using non-transferred arc plasma. *Adv. Powder Technol.* **2012**, *23*, 701–707. [[CrossRef](#)]
153. Kamura, A.; Idota, N.; Sugahara, Y. Nonaqueous synthesis of magnetite nanoparticles via oxidation of tetrachloroferrate anions by pyridine-N-oxide. *Solid State Sci.* **2019**, *92*, 81–88. [[CrossRef](#)]
154. Pedrosa, J.; Costa, B.F.O.; Portugal, A.; Durães, L. Controlled phase formation of nanocrystalline iron oxides/hydroxides in solution—An insight on the phase transformation mechanisms. *Mater. Chem. Phys.* **2015**, *163*, 88–98. [[CrossRef](#)]
155. Samulewski, R.B.; Gonçalves, J.M.; Urbano, A.; Da Costa, A.C.S.; Ivashita, F.F.; Paesano, A.; Zaia, D.A.M. Magnetite synthesis in the presence of cyanide or thiocyanate under prebiotic chemistry conditions. *Life* **2020**, *10*, 34. [[CrossRef](#)]
156. Shen, L.; Qiao, Y.; Guo, Y.; Tan, J. Preparation and formation mechanism of nano-iron oxide black pigment from blast furnace flue dust. *Ceram. Int.* **2013**, *39*, 737–744. [[CrossRef](#)]
157. Sun, S.; Gebauer, D.; Cölfen, H. Alignment of Amorphous Iron Oxide Clusters: A Non-Classical Mechanism for Magnetite Formation. *Angew. Chem.-Int. Ed.* **2017**, *56*, 4042–4046. [[CrossRef](#)] [[PubMed](#)]
158. Suppiah, D.D.; Abd Hamid, S.B. One step facile synthesis of ferromagnetic magnetite nanoparticles. *J. Magn. Magn. Mater.* **2016**, *414*, 204–208. [[CrossRef](#)]

159. Demirbas, A.; Kislakci, E.; Karaagac, Z.; Onal, I.; Ildiz, N.; Ocsoy, I. Preparation of biocompatible and stable iron oxide nanoparticles using anthocyanin integrated hydrothermal method and their antimicrobial and antioxidant properties. *Mater. Res. Express* **2019**, *6*, 125011. [[CrossRef](#)]
160. Tahirbegi, I.B.; Pardo, W.A.; Alvira, M.; Mir, M.; Samitier, J. Amyloid $\text{A}\beta_{42}$, a promoter of magnetite nanoparticle formation in Alzheimer's disease. *Nanotechnology* **2016**, *27*, 465102. [[CrossRef](#)]
161. Baumgartner, J.; Morin, G.; Menguy, N.; Gonzalez, T.P.; Widdrat, M.; Cosmidis, J.; Faivre, D. Magnetotactic bacteria form magnetite from a phosphate-rich ferric hydroxide via nanometric ferric (oxyhydr)oxide intermediates. *Proc. Natl. Acad. Sci. USA* **2013**, *110*, 14883–14888. [[CrossRef](#)] [[PubMed](#)]
162. Sugimoto, T.; Matijević, E. Formation of uniform spherical magnetite particles by crystallization from ferrous hydroxide gels. *J. Colloid Interface Sci.* **1980**, *74*, 227–243. [[CrossRef](#)]
163. Brunner, J.; Baburin, I.A.; Sturm, S.; Kvashnina, K.; Rossberg, A.; Pietsch, T.; Andreev, S.; Sturm, E.; Cölfen, H. Self-Assembled Magnetite Mesocrystalline Films: Toward Structural Evolution from 2D to 3D Superlattices. *Adv. Mater. Interfaces* **2017**, *4*, 1600431. [[CrossRef](#)]
164. Costa, R.C.C.; Moura, F.C.C.; Ardisson, J.D.; Fabris, J.D.; Lago, R.M. Highly active heterogeneous Fenton-like systems based on $\text{Fe}_0/\text{Fe}_3\text{O}_4$ composites prepared by controlled reduction of iron oxides. *Appl. Catal. B Environ.* **2008**, *83*, 131–139. [[CrossRef](#)]
165. Crowley, T.A.; Ziegler, K.J.; Lyons, D.M.; Erts, D.; Olin, H.; Morris, M.A.; Holmes, J.D. Synthesis of metal and metal oxide nanowire and nanotube arrays within a mesoporous silica template. *Chem. Mater.* **2003**, *15*, 3518–3522. [[CrossRef](#)]
166. Fredrickson, J.K.; Zachara, J.M.; Kennedy, D.W.; Dong, H.; Onstott, T.C.; Hinman, N.W.; Li, S.M. Biogenic iron mineralization accompanying the dissimilatory reduction of hydrous ferric oxide by a groundwater bacterium. *Geochim. Cosmochim. Acta* **1998**, *62*, 3239–3257. [[CrossRef](#)]
167. Fujioka, N.; Suzuki, M.; Kurosu, S.; Kawase, Y. Linkage of iron elution and dissolved oxygen consumption with removal of organic pollutants by nanoscale zero-valent iron: Effects of pH on iron dissolution and formation of iron oxide/hydroxide layer. *Chemosphere* **2016**, *144*, 1738–1746. [[CrossRef](#)] [[PubMed](#)]
168. Atta, A.M.; El-Saeed, A.M.; El-Mahdy, G.M.; Al-Lohedan, H.A. Application of magnetite nano-hybrid epoxy as protective marine coatings for steel. *RSC Adv.* **2015**, *5*, 101923–101931. [[CrossRef](#)]
169. Bardajee, G.R.; Hooshyar, Z.; Asli, M.J.; Shahidi, F.E.; Dianatnejad, N. Synthesis of a novel supermagnetic iron oxide nanocomposite hydrogel based on graft copolymerization of poly((2-dimethylamino)ethyl methacrylate) onto salep for controlled release of drug. *Mater. Sci. Eng. C* **2014**, *36*, 277–286. [[CrossRef](#)]
170. Jubb, A.M.; Eskelsen, J.R.; Yin, X.; Zheng, J.; Philben, M.J.; Pierce, E.M.; Graham, D.E.; Wullschleger, S.D.; Gu, B. Characterization of iron oxide nanoparticle films at the air–water interface in Arctic tundra waters. *Sci. Total Environ.* **2018**, *633*, 1460–1468. [[CrossRef](#)]
171. Kurtdabar, M.; Koutenaee, R.N.; Bardajee, G.R. Synthesis and characterization of a novel pH-responsive nanocomposite hydrogel based on chitosan for targeted drug release. *J. Polym. Res.* **2018**, *25*, 119. [[CrossRef](#)]
172. Liang, S.; Shi, S.; Zhang, H.; Qiu, J.; Yu, W.; Li, M.; Gan, Q.; Yu, W.; Xiao, K.; Liu, B.; et al. One-pot solvothermal synthesis of magnetic biochar from waste biomass: Formation mechanism and efficient adsorption of Cr(VI) in an aqueous solution. *Sci. Total Environ.* **2019**, *695*, 133886. [[CrossRef](#)]
173. Liu, H.; Li, J.C.; Sun, F.; Hu, J. Characterization and effect of pre-oxidation on D.C. plasma nitriding for AISI4140 steel. *Vacuum* **2014**, *109*, 170–174. [[CrossRef](#)]
174. Liu, M.; Liu, Q.; Zang, Z.; Han, R. Adsorptive removal of sulfosalicylic acid from aqueous medium by iron(III)-loaded magnetic chitosan/graphene oxide. *J. Colloid Interface Sci.* **2022**, *606*, 1249–1260. [[CrossRef](#)]
175. Mo, J.; Steen, S.M.; Zhang, F.Y.; Toops, T.J.; Brady, M.P.; Green, J.B. Electrochemical investigation of stainless steel corrosion in a proton exchange membrane electrolyzer cell. *Int. J. Hydrogen Energy* **2015**, *40*, 12506–12511. [[CrossRef](#)]
176. Brunner, J.J.S.N.; Maier, B.; Kirner, F.; Sturm, S.; Cölfen, H.; Sturm, E.V. Self-Assembled Faceted Mesocrystals: Advances in Optimization of Growth Conditions. *Cryst. Growth Des.* **2021**, *21*, 5490–5495. [[CrossRef](#)]
177. Shimojo, M.; Takeguchi, M.; Mitsuishi, K.; Tanaka, M.; Furuya, K. Mechanisms of crystalline iron oxide formation in electron beam-induced deposition. *Jpn. J. Appl. Phys. Part 1 Regul. Pap. Short Notes Rev. Pap.* **2007**, *46*, 6247–6249. [[CrossRef](#)]
178. Touqueer, T.; Mumtaz, M.W.; Mukhtar, H.; Irfan, A.; Akram, S.; Shabbir, A.; Rashid, U.; Nehdi, I.A.; Choong, T.S.Y. Fe_3O_4 -PDA-lipase as surface functionalized nano biocatalyst for the production of biodiesel using waste cooking oil as feedstock: Characterization and process optimization. *Energies* **2020**, *13*, 177. [[CrossRef](#)]
179. Yu, B.Y.; Kwak, S.Y. Assembly of magnetite nanocrystals into spherical mesoporous aggregates with a 3-D wormhole-like pore structure. *J. Mater. Chem.* **2010**, *20*, 8320–8328. [[CrossRef](#)]
180. Zhu, Z.; Zhang, M.; Zhu, Y.; Huang, F.; Si, T.; Xu, R.X. Perfluorocarbon-Loaded Hydrogel Microcapsules from Interface Shearing for Magnetic Guided Ultrasound and Laser Activation. *Front. Phys.* **2020**, *8*, 581519. [[CrossRef](#)]
181. Zhang, H.; Yang, Y.; Bao, N.; Ding, J. Scalable route to mesoporous iron oxides and their Cr(VI) ions uptake capacity study. *Mater. Chem. Phys.* **2014**, *144*, 512–518. [[CrossRef](#)]
182. Zheng, W.; Hauwiller, M.R.; Liang, W.I.; Ophus, C.; Ercius, P.; Chan, E.M.; Chu, Y.H.; Asta, M.; Du, X.; Alivisatos, A.P.; et al. Real time imaging of two-dimensional iron oxide spherulite nanostructure formation. *Nano Res.* **2019**, *12*, 2889–2893. [[CrossRef](#)]

183. Aisida, S.O.; Ugwu, K.; Akpa, P.A.; Nwanya, A.C.; Nwankwo, U.; Bashir, A.K.H.; Madiba, I.G.; Ahmed, I.; Ezema, F.I. Synthesis and characterization of iron oxide nanoparticles capped with Moringa Oleifera: The mechanisms of formation effects on the optical, structural, magnetic and morphological properties. In *Materials Today: Proceedings*; Elsevier Ltd.: Amsterdam, The Netherlands, 2021; Volume 36, pp. 214–218.
184. Baalousha, M.; Manciulea, A.; Cumberland, S.; Kendall, K.; Lead, J.R. Aggregation and surface properties of iron oxide nanoparticles: Influence of pH and natural organic matter. *Environ. Toxicol. Chem.* **2008**, *27*, 1875–1882. [[CrossRef](#)]
185. Bhar, R.; Kaur, G.; Mehta, S.K. Exploring drying pattern of a sessile droplet of genomic DNA in the presence of hematite nanoparticles. *Sci. Rep.* **2018**, *8*, 6352. [[CrossRef](#)]
186. Fomin, A.; Poliak, M.; Rahinov, I.; Tsionsky, V.; Cheskis, S. Combined particle mass spectrometer-quartz crystal microbalance apparatus for in situ nanoparticle monitoring during flame assisted synthesis. *Combust. Flame* **2013**, *160*, 2131–2140. [[CrossRef](#)]
187. Lemine, O.M. Transformation of goethite to hematite nanocrystallines by high energy ball milling. *Adv. Mater. Sci. Eng.* **2014**, *2014*, 589146. [[CrossRef](#)]
188. Liu, J.; Zhu, R.; Ma, L.; Fu, H.; Lin, X.; Parker, S.C.; Molinari, M. Adsorption of phosphate and cadmium on iron (oxyhydr)oxides: A comparative study on ferrihydrite, goethite, and hematite. *Geoderma* **2021**, *383*, 114799. [[CrossRef](#)]
189. Lu, Y.; Hu, S.; Liu, F.; Liang, Y.; Shi, Z. Effects of humic acid and fulvic acid on the sequestration of copper and carbon during the iron oxide transformation. *Chem. Eng. J.* **2020**, *383*, 123194. [[CrossRef](#)]
190. Pallela, P.N.V.K.; Ummey, S.; Ruddaraju, L.K.; Gadi, S.; Cherukuri, C.S.L.; Barla, S.; Pammi, S.V.N. Antibacterial efficacy of green synthesized α -Fe₂O₃ nanoparticles using Sida cordifolia plant extract. *Heliyon* **2019**, *5*, e02765. [[CrossRef](#)] [[PubMed](#)]
191. Sharma, G.; Jeevanandam, P. Synthesis of self-assembled prismatic iron oxide nanoparticles by a novel thermal decomposition route. *RSC Adv.* **2013**, *3*, 189–200. [[CrossRef](#)]
192. Soltis, J.A.; Feinberg, J.M.; Gilbert, B.; Penn, R.L. Phase Transformation and Particle-Mediated Growth in the Formation of Hematite from 2-Line Ferrihydrite. *Cryst. Growth Des.* **2016**, *16*, 922–932. [[CrossRef](#)]
193. Ramasubramanian, N.; Preocanin, N.; Davidson, R.D. Analysis of Passive Films on Stainless Steel by Cyclic Voltammetry and Auger Spectroscopy. *J. Electrochem. Soc.* **1985**, *132*, 793–798. [[CrossRef](#)]
194. Jin, X.; Hu, G.; Wang, L.; Wang, H. Characterization of surface layers of oxidation-reduction treated Si and Mn added advanced high strength steel. *Surf. Coatings Technol.* **2020**, *382*, 125172. [[CrossRef](#)]
195. Lutz, B.S.; Holcomb, G.R.; Meier, G.H. Determination of the Initiation and Propagation Mechanism of Fireside Corrosion. *Oxid. Met.* **2015**, *84*, 353–381. [[CrossRef](#)]
196. Guo, W.; Sun, W.; Lv, L.P.; Kong, S.; Wang, Y. Microwave-Assisted Morphology Evolution of Fe-Based Metal-Organic Frameworks and Their Derived Fe₂O₃ Nanostructures for Li-Ion Storage. *ACS Nano* **2017**, *11*, 4198–4205. [[CrossRef](#)] [[PubMed](#)]
197. Ivanova, A.; Fominykh, K.; Fattakhova-Rohlfing, D.; Zeller, P.; Döblinger, M.; Bein, T. Nanocellulose-assisted formation of porous hematite nanostructures. *Inorg. Chem.* **2015**, *54*, 1129–1135. [[CrossRef](#)]
198. Allen, C.C.; Probst, L.W.; Flood, B.E.; Longazo, T.G.; Schelble, R.T.; Westall, F. Meridiani Planum hematite deposit and the search for evidence of life on Mars—Iron mineralization of microorganisms in rock varnish. *Icarus* **2004**, *171*, 20–30. [[CrossRef](#)]
199. Beitler, B.; Parry, W.T.; Chan, M.A. Fingerprints of fluid flow: Chemical diagenetic history of the Jurassic Navajo Sandstone, southern Utah, USA. *J. Sediment. Res.* **2005**, *75*, 547–561. [[CrossRef](#)]
200. Azevedo, J.; Fernández-García, M.P.; Magén, C.; Mendes, A.; Araújo, J.P.; Sousa, C.T. Double-walled iron oxide nanotubes via selective chemical etching and Kirkendall process. *Sci. Rep.* **2019**, *9*, 11994. [[CrossRef](#)] [[PubMed](#)]
201. Budiman, F.; Tan, W.K.; Kawamura, G.; Muto, H.; Matsuda, A.; Razak, K.A.; Lockman, Z. Formation of Dense and High-Aspect-Ratio Iron Oxide Nanowires by Water Vapor-Assisted Thermal Oxidation and Their Cr(VI) Adsorption Properties. *ACS Omega* **2021**, *6*, 28203–28214. [[CrossRef](#)]
202. Chen, T.; Xie, Q.; Xu, H.; Chen, J.; Ji, J.; Lu, H.; Balsam, W. Characteristics and formation mechanism of pedogenic hematite in Quaternary Chinese loess and paleosols. *Catena* **2010**, *81*, 217–225. [[CrossRef](#)]
203. De Carvalho, V.A.N.; Luz, R.A.D.S.; Lima, B.H.; Crespilho, F.N.; Leite, E.R.; Souza, F.L. Highly oriented hematite nanorods arrays for photoelectrochemical water splitting. *J. Power Sources* **2012**, *205*, 525–529. [[CrossRef](#)]
204. Delgado, A.; Cordova, S.; Shafirovich, E. Thermite reactions with oxides of iron and silicon during combustion of magnesium with lunar and Martian regolith simulants. *Combust. Flame* **2015**, *162*, 3333–3340. [[CrossRef](#)]
205. Dias, L.; Rosado, T.; Candeias, A.; Mirão, J.; Caldeira, A.T. A change in composition, a change in colour: The case of limestone sculptures from the Portuguese National Museum of Ancient Art. *J. Cult. Herit.* **2020**, *42*, 255–262. [[CrossRef](#)]
206. Dunn, S.C.; von der Heyden, B.P. Gold remobilization in gossans of the Amani area, southwestern Tanzania. *Ore Geol. Rev.* **2021**, *131*, 104033. [[CrossRef](#)]
207. Ebaid, Y.Y.; Nasr, M.M.; Santos, J.K.B.; Makhlof, O. Behavior of uranium series in groundwater of the Wajid Formation, Wadi AdDawasir, Saudi Arabia. *Environ. Monit. Assess.* **2020**, *192*, 564. [[CrossRef](#)] [[PubMed](#)]
208. Egglseder, M.S.; Cruden, A.R.; Tomkins, A.G.; Wilson, S.A.; Dalstra, H.J.; Rielli, A.; Li, C.; Baumgartner, J.; Faivre, D. Tiny particles building huge ore deposits—Particle-based crystallisation in banded iron formation-hosted iron ore deposits (Hamersley Province, Australia). *Ore Geol. Rev.* **2019**, *104*, 160–174. [[CrossRef](#)]
209. Einert, M.; Ostermann, R.; Weller, T.; Zellmer, S.; Garnweithner, G.; Smarsly, B.M.; Marschall, R. Hollow α -Fe₂O₃ nanofibres for solar water oxidation: Improving the photoelectrochemical performance by formation of α -Fe₂O₃/ITO-composite photoanodes. *J. Mater. Chem. A* **2016**, *4*, 18444–18456. [[CrossRef](#)]

210. Fru, E.C.; Ivarsson, M.; Kilias, S.P.; Bengtson, S.; Belivanova, V.; Marone, F.; Fortin, D.; Broman, C.; Stampanoni, M. Fossilized iron bacteria reveal a pathway to the biological origin of banded iron formation. *Nat. Commun.* **2013**, *4*, 2050. [[CrossRef](#)] [[PubMed](#)]
211. Gash, A.E.; Tillotson, T.M.; Satcher, J.H.; Poco, J.F.; Hrubesh, L.W.; Simpson, R.L. Use of epoxides in the sol-gel synthesis of porous iron(III) oxide monoliths from Fe(III) salts. *Chem. Mater.* **2001**, *13*, 999–1007. [[CrossRef](#)]
212. Han, X.; Tomaszewski, E.J.; Sorwat, J.; Pan, Y.; Kappler, A.; Byrne, J.M. Oxidation of green rust by anoxygenic phototrophic Fe(II)-oxidising bacteria. *Geochim. Perspect. Lett.* **2020**, *12*, 52–57. [[CrossRef](#)]
213. Kikuchi, S.; Makita, H.; Takai, K.; Yamaguchi, N.; Takahashi, Y. Characterization of biogenic iron oxides collected by the newly designed liquid culture method using diffusion chambers. *Geobiology* **2014**, *12*, 133–145. [[CrossRef](#)]
214. Kirk, A.M.; Sun, W.; Bennett, C.J.; Shipway, P.H. Interaction of displacement amplitude and frequency effects in fretting wear of a high strength steel: Impact on debris bed formation and subsurface damage. *Wear* **2021**, *482–483*, 203981. [[CrossRef](#)]
215. Kuai, J.; Zhang, J.; Ardashev, D.V.; Zhang, H. Properties of α -Fe₂O₃ in Oxide Film of α -Fe Grinding Wheel without Abrasive Particles. *Ferroelectrics* **2019**, *548*, 1–7. [[CrossRef](#)]
216. Li, Y.; Cheng, Y.F. Photocatalytic anti-bioadhesion and bacterial deactivation on nanostructured iron oxide films. *J. Mater. Chem. B* **2018**, *6*, 1458–1469. [[CrossRef](#)] [[PubMed](#)]
217. Liu, B.; Zhang, S.G.; Chang, C.C.; Volinsky, A.A. Preparation and formation mechanism of monodisperse micaceous iron oxide from iron chromium grinding waste. *Powder Technol.* **2018**, *329*, 401–408. [[CrossRef](#)]
218. Martín-González, M.; Martínez-Moro, R.; Aguirre, M.H.; Flores, E.; Caballero-Calero, O. Unravelling nanoporous anodic iron oxide formation. *Electrochim. Acta* **2020**, *330*, 135241. [[CrossRef](#)]
219. Mechakra, H.; Sehili, T.; Kribache, M.A.; Ayachi, A.A.; Rossignol, S.; George, C. Use of natural iron oxide as heterogeneous catalyst in photo-Fenton-like oxidation of chlorophenylurea herbicide in aqueous solution: Reaction monitoring and degradation pathways. *J. Photochem. Photobiol. A Chem.* **2016**, *317*, 140–150. [[CrossRef](#)]
220. Natile, M.M.; Glisenti, A. New NiO/Co₃O₄ and Fe₂O₃/Co₃O₄ nanocomposite catalysts: Synthesis and characterization. *Chem. Mater.* **2003**, *15*, 2502–2510. [[CrossRef](#)]
221. Pang, Q.; DorMohammadi, H.; Isgor, O.B.; Árnadóttir, L. The Effect of Surface Defects on Chloride-Induced Depassivation of Iron—A Density Functional Theory Study. *Corrosion* **2020**, *76*, 690–697. [[CrossRef](#)]
222. Peng, L.; Peng, H.; Li, N.; Zhong, W.; Mao, L.; You, K.; Yin, D. Facile access to nitroalkanes: Nitration of alkanes by selective CH nitration using metal nitrate, catalyzed by in-situ generated metal oxide. *Catal. Commun.* **2020**, *142*, 106035. [[CrossRef](#)]
223. Popov, N.; Bošković, M.; Perović, M.; Zadro, K.; Gilja, V.; Krehula, L.K.; Robić, M.; Marciuš, M.; Ristić, M.; Musić, S.; et al. Effect of Ru³⁺ ions on the formation, structural, magnetic and optical properties of hematite (α -Fe₂O₃) nanorods. *J. Magn. Magn. Mater.* **2021**, *538*, 168316. [[CrossRef](#)]
224. Qu, C.; Qian, S.; Chen, L.; Guan, Y.; Zheng, L.; Liu, S.; Chen, W.; Cai, P.; Huang, Q. Size-dependent bacterial toxicity of hematite particles. *Environ. Sci. Technol.* **2019**, *53*, 8147–8156. [[CrossRef](#)]
225. Rackauskas, S.; Nasibulin, A.G.; Jiang, H.; Tian, Y.; Kleshch, V.I.; Sainio, J.; Obraztsova, E.D.; Bokova, S.N.; Obraztsov, A.N.; Kauppinen, E.I. A novel method for metal oxide nanowire synthesis. *Nanotechnology* **2009**, *20*, 165603. [[CrossRef](#)] [[PubMed](#)]
226. Ratanaphain, C.; Viboonratanasri, D.; Prompinit, P.; Krajangpan, S.; Khan, E.; Punyapalakul, P. Reactivity characterization of SiO₂-coated nano zero-valent iron for iodoacetamide degradation: The effects of SiO₂ thickness, and the roles of dehalogenation, hydrolysis and adsorption. *Chemosphere* **2022**, *286*, 131816. [[CrossRef](#)] [[PubMed](#)]
227. Ren, G.; Yan, Y.; Nie, Y.; Lu, A.; Wu, X.; Li, Y.; Wang, C.; Ding, H. Natural extracellular electron transfer between semiconducting minerals and electroactive bacterial communities occurred on the rock varnish. *Front. Microbiol.* **2019**, *10*, 293. [[CrossRef](#)]
228. Ryu, Y.J.; Kim, M.; Yoo, C.S. Phase Diagram and Transformations of Iron Pentacarbonyl to nm Layered Hematite and Carbon-Oxygen Polymer under Pressure. *Sci. Rep.* **2015**, *5*, 15139. [[CrossRef](#)] [[PubMed](#)]
229. Shi, P.; Wang, F.; Zhu, J.; Zhang, B.; Zhao, T.; Wang, Y.; Wang, J. Effect of phase separation on the Jian ware blue colored glaze with iron oxide. *Ceram. Int.* **2018**, *44*, 16407–16413. [[CrossRef](#)]
230. Sun, J.; Wei, L.; Yin, R.; Jiang, F.; Shang, C. Microbial iron reduction enhances in-situ control of biogenic hydrogen sulfide by FeOOH granules in sediments of polluted urban waters. *Water Res.* **2020**, *171*, 115453. [[CrossRef](#)]
231. Sundararajan, J.A.; Kaur, M.; Qiang, Y. Mechanism of electron beam induced oxide layer thickening on iron-iron oxide core-shell nanoparticles. *J. Phys. Chem. C* **2015**, *119*, 8357–8363. [[CrossRef](#)]
232. Taniguchi, A.; Taniguchi, T.; Wagata, H.; Katsumata, K.I.; Okada, K.; Matsushita, N. Liquid-phase atomic layer deposition of crystalline hematite without post-growth annealing. *CrystEngComm* **2019**, *21*, 4184–4191. [[CrossRef](#)]
233. Umar, A.; Ibrahim, A.A.; Kumar, R.; Albargi, H.; Alsaiari, M.A.; Ahmed, F. Cubic shaped hematite (α -Fe₂O₃) micro-structures composed of stacked nanosheets for rapid ethanol sensor application. *Sens. Actuators B Chem.* **2021**, *326*, 128851. [[CrossRef](#)]
234. Vasilyeva, M.S.; Rudnev, V.S.; Zvereva, A.A.; Ustinov, A.Y.; Arefieva, O.D.; Kuryavyi, V.G.; Zverev, G.A. FeOx, SiO₂, TiO₂/Ti composites prepared using plasma electrolytic oxidation as photo-Fenton-like catalysts for phenol degradation. *J. Photochem. Photobiol. A Chem.* **2018**, *356*, 38–45. [[CrossRef](#)]
235. Vinayagam, R.; Pai, S.; Varadavankatesan, T.; Narasimhan, M.K.; Narayanasamy, S.; Selvaraj, R. Structural characterization of green synthesized α -Fe₂O₃ nanoparticles using the leaf extract of *Spondias dulcis*. *Surf. Interfaces* **2020**, *20*, 100618. [[CrossRef](#)]
236. Wang, Y.; Cao, Z.Z.; Niu, Y.; Lyu, H.B. Macromechanics, microstructure and particle contact model of artificially cemented laterite. *Mater. Express* **2021**, *11*, 732–739. [[CrossRef](#)]

237. Xie, K.; Guo, M.; Huang, H.; Liu, Y. Fabrication of iron oxide nanotube arrays by electrochemical anodization. *Corros. Sci.* **2014**, *88*, 66–75. [[CrossRef](#)]
238. Yang, Y.; Luo, X.; Elsayed, Y.E.A.N.; Hong, C.; Yadav, A.; Rogowska, M.; Ambat, R. Characteristics of scales and their impacts on under-deposit corrosion in an oil production well. *Mater. Corros.* **2021**, *72*, 1051–1064. [[CrossRef](#)]
239. Zha, J.; Wei, S.; Wang, C.; Li, Z.; Cai, Y.; Ma, Q. Weathering mechanism of red discolorations on Limestone object: A case study from Lingyan Temple, Jinan, Shandong Province, China. *Herit. Sci.* **2020**, *8*, 54. [[CrossRef](#)]
240. Zhang, F.S.; Itoh, H. Iron oxide-loaded slag for arsenic removal from aqueous system. *Chemosphere* **2005**, *60*, 319–325. [[CrossRef](#)]
241. Zhang, R.; Dai, H.; Du, Y.; Zhang, L.; Deng, J.; Xia, Y.; Zhao, Z.; Meng, X.; Liu, Y. P123-PMMA dual-templating generation and unique physicochemical properties of three-dimensionally ordered macroporous iron oxides with nanovoids in the crystalline walls. *Inorg. Chem.* **2011**, *50*, 2534–2544. [[CrossRef](#)] [[PubMed](#)]
242. Zhang, M.; Fang, K.; Lin, M.; Hou, B.; Zhong, L.; Zhu, Y.; Wei, W.; Sun, Y. Controlled fabrication of iron oxide/mesoporous silica core-shell nanostructures. *J. Phys. Chem. C* **2013**, *117*, 21529–21538. [[CrossRef](#)]
243. Zhu, G.; Sushko, M.L.; Loring, J.S.; Legg, B.A.; Song, M.; Soltis, J.A.; Huang, X.; Rosso, K.M.; De Yoreo, J.J. Self-similar mesocrystals form via interface-driven nucleation and assembly. *Nature* **2021**, *590*, 416–422. [[CrossRef](#)]
244. Baldovi, H.G. Optimization of α -Fe₂O₃ nanopillars diameters for photoelectrochemical enhancement of α -Fe₂O₃-TiO₂ heterojunction. *Nanomaterials* **2021**, *11*, 2019. [[CrossRef](#)]
245. Basak, S.; Tiwari, V.; Fan, J.; Achilefu, S.; Sethi, V.; Biswas, P. Single step aerosol synthesis of nanocomposites by aerosol routes: γ -Fe₂O₃/SiO₂ and their functionalization. *J. Mater. Res.* **2011**, *26*, 1225–1233. [[CrossRef](#)]
246. Ikoma, S.; Ohki, K.; Yokoi, H. Preparation and characterization of silica-supported maghemite. *J. Ceram. Soc. Jpn.* **1992**, *100*, 864–866. [[CrossRef](#)]
247. Coddens, E.M.; Huang, L.; Wong, C.; Grassian, V.H. Influence of Glyoxal on the Catalytic Oxidation of S(IV) in Acidic Aqueous Media. *ACS Earth Space Chem.* **2019**, *3*, 142–149. [[CrossRef](#)]
248. Inamdar, S.; Choi, H.S.; Kim, M.S.; Chaudhari, K.; Yu, J.S. Flame synthesis of 26-faceted maghemite polyhedrons grown via 14-faceted polyhedrons and their carbon composites for Li-ion battery application. *CrystEngComm* **2012**, *14*, 7009–7014. [[CrossRef](#)]
249. Kaewsaneha, C.; Elaissari, A.; Opaprakasit, P.; Sreearunothai, P.; Tangboriboonrat, P. Poly(styrene-b-acrylic Acid) Nanoparticles with High Magnetic Loading for Magnetic Hyperthermia Cancer Therapy. *ACS Appl. Nano Mater.* **2021**, *4*, 1841–1848. [[CrossRef](#)]
250. Mishra, D.; Greving, D.; Confalonieri, G.A.B.; Perlich, J.; Toperberg, B.P.; Zabel, H.; Petracic, O. Growth modes of nanoparticle superlattice thin films. *Nanotechnology* **2014**, *25*, 205602. [[CrossRef](#)]
251. Sharifi, T.; Gracia-Espino, E.; Barzegar, H.R.; Jia, X.; Nitze, F.; Hu, G.; Nordblad, P.; Tai, C.W.; Wågberg, T. Formation of nitrogen-doped graphene nanoscrolls by adsorption of magnetic γ -Fe₂O₃ nanoparticles. *Nat. Commun.* **2013**, *4*, 2319. [[CrossRef](#)]
252. Wang, C.M.; Baer, D.R.; Thomas, L.E.; Amonette, J.E.; Antony, J.; Qiang, Y.; Duscher, G. Void formation during early stages of passivation: Initial oxidation of iron nanoparticles at room temperature. *J. Appl. Phys.* **2005**, *98*, 094308. [[CrossRef](#)]
253. Wen, Z.; Lu, J.; Zhang, Y.; Cheng, G.; Huang, S.; Chen, J.; Xu, R.; Ming, Y.A.; Wang, Y.; Chen, R. Facile inverse micelle fabrication of magnetic ordered mesoporous iron cerium bimetal oxides with excellent performance for arsenic removal from water. *J. Hazard. Mater.* **2020**, *383*, 121172. [[CrossRef](#)]
254. Ahamed, I.; Skomski, R.; Kashyap, A. Controlling the magnetocrystalline anisotropy of ϵ -Fe₂O₃. *AIP Adv.* **2019**, *9*, 035231. [[CrossRef](#)]
255. Gorbachev, E.; Soshnikov, M.; Wu, M.; Alyabyeva, L.; Myakishev, D.; Kozlyakova, E.; Lebedev, V.; Anokhin, E.; Gorshunov, B.; Brylev, O.; et al. Tuning the particle size, natural ferromagnetic resonance frequency and magnetic properties of ϵ -Fe₂O₃ nanoparticles prepared by a rapid sol-gel method. *J. Mater. Chem. C* **2021**, *9*, 6173–6179. [[CrossRef](#)]
256. Jang, M.S.; Ok, H.J.; Oh, I.; Kang, G.H.; Yoo, J.W.; Lee, K.S. Formation of Y₃Fe₅O₁₂ matrix including ϵ -phase Fe₂O₃ with the giant coercive field via optimized sol-gel method. *J. Magn. Magn. Mater.* **2022**, *552*, 169218. [[CrossRef](#)]
257. López-Sánchez, J.; Serrano, A.; del Campo, A.; Muñoz-Noval, Á.; Salas-Colera, E.; Cabero, M.; Varela, M.; Abuín, M.; Castro, G.R.; Rubio-Zuazo, J.; et al. A combined micro-Raman, X-ray absorption and magnetic study to follow the glycerol-assisted growth of epsilon-iron oxide sol-gel coatings. *J. Alloys Compd.* **2022**, *892*, 162061. [[CrossRef](#)]
258. Maccato, C.; Carraro, G.; Peddis, D.; Varvaro, G.; Barreca, D. Magnetic properties of ϵ iron(III) oxide nanorod arrays functionalized with gold and copper(II) oxide. *Appl. Surf. Sci.* **2018**, *427*, 890–896. [[CrossRef](#)]
259. Nikolić, V.N.; Tadić, M.; Panjan, M.; Kopanja, L.; Cvjetićanin, N.; Spasojević, V. Influence of annealing treatment on magnetic properties of Fe₂O₃/SiO₂ and formation of ϵ -Fe₂O₃ phase. *Ceram. Int.* **2017**, *43*, 3147–3155. [[CrossRef](#)]
260. Suturin, S.M.; Korovin, A.M.; Sitnikova, A.A.; Kirilenko, D.A.; Volkov, M.P.; Dvortsova, P.A.; Ukleev, V.A.; Tabuchi, M.; Sokolov, N.S. Correlation between crystal structure and magnetism in PLD grown epitaxial films of ϵ -Fe₂O₃ on GaN. *Sci. Technol. Adv. Mater.* **2021**, *22*, 85–99. [[CrossRef](#)]
261. Tadic, M.; Milosevic, I.; Kralj, S.; Hanzel, D.; Barudzija, T.; Motte, L.; Makovec, D. Surface-induced reversal of a phase transformation for the synthesis of ϵ -Fe₂O₃ nanoparticles with high coercivity. *Acta Mater.* **2020**, *188*, 16–22. [[CrossRef](#)]
262. Tokoro, H.; Namai, A.; Ohkoshi, S.I. Advances in magnetic films of epsilon-iron oxide toward next-generation high-density recording media. *Dalton Trans.* **2021**, *50*, 452–459. [[CrossRef](#)]
263. Ukleev, V.; Volkov, M.; Korovin, A.; Saerbeck, T.; Sokolov, N.; Suturin, S. Stabilization of ϵ -Fe₂O₃ epitaxial layer on MgO(111)/GaN via an intermediate γ -phase. *Phys. Rev. Mater.* **2019**, *3*, 094401. [[CrossRef](#)]

264. Myhill, R.; Ojwang, D.O.; Ziberna, L.; Frost, D.J.; Ballaran, T.B.; Miyajima, N. On the P–T–fO₂ stability of Fe₄O₅, Fe₅O₆ and Fe₄O₅-rich solid solutions. *Contrib. Mineral. Petrol.* **2016**, *171*, 51. [[CrossRef](#)]
265. Ovsyannikov, S.V.; Bykov, M.; Bykova, E.; Kozlenko, D.P.; Tsirlin, A.A.; Karkin, A.E.; Shchennikov, V.V.; Kichanov, S.E.; Gou, H.; Abakumov, A.M.; et al. Charge-ordering transition in iron oxide Fe₄O₅ involving competing dimer and trimer formation. *Nat. Chem.* **2016**, *8*, 501–508. [[CrossRef](#)] [[PubMed](#)]
266. Bligh, M.W.; Waite, T.D. Formation, reactivity, and aging of ferric oxide particles formed from Fe(II) and Fe(III) sources: Implications for iron bioavailability in the marine environment. *Geochim. Cosmochim. Acta* **2011**, *75*, 7741–7758. [[CrossRef](#)]
267. Bligh, M.W.; Maheshwari, P.; Waite, T.D. Formation, reactivity and aging of amorphous ferric oxides in the presence of model and membrane bioreactor derived organics. *Water Res.* **2017**, *124*, 341–352. [[CrossRef](#)] [[PubMed](#)]
268. Brigante, M.; Parolo, M.E.; Schulz, P.C.; Avena, M. Synthesis, characterization of mesoporous silica powders and application to antibiotic remotion from aqueous solution. Effect of supported Fe-oxide on the SiO₂ adsorption properties. *Powder Technol.* **2014**, *253*, 178–186. [[CrossRef](#)]
269. Greenberg, E.; Armon, N.; Kapon, O.; Ben-Ishai, M.; Shpaisman, H. Nanostructure and Mechanism of Metal Deposition by a Laser-Induced Photothermal Reaction. *Adv. Mater. Interfaces* **2019**, *6*, 1900541. [[CrossRef](#)]
270. Chow, S.S.; Taillefert, M. Effect of arsenic concentration on microbial iron reduction and arsenic speciation in an iron-rich freshwater sediment. *Geochim. Cosmochim. Acta* **2009**, *73*, 6008–6021. [[CrossRef](#)]
271. Karakaya, Y.; Kluge, S.; Wiggers, H.; Schulz, C.; Kasper, T. Investigation of the combustion of iron pentacarbonyl and the formation of key intermediates in iron oxide synthesis flames. *Chem. Eng. Sci.* **2021**, *230*, 116169. [[CrossRef](#)]
272. Paur, H.R.; Baumann, W.; Mätzing, H.; Seifert, H. Formation of nanoparticles in flames; Measurement by particle mass spectrometry and numerical simulation. *Nanotechnology* **2005**, *16*, S354–S361. [[CrossRef](#)]
273. Poliak, M.; Fomin, A.; Tsionsky, V.; Cheskins, S.; Wlokas, I.; Rahinov, I. On the mechanism of nanoparticle formation in a flame doped by iron pentacarbonyl. *Phys. Chem. Chem. Phys.* **2015**, *17*, 680–685. [[CrossRef](#)]
274. Xie, Y.; Dong, F.; Heinbuch, S.; Rocca, J.J.; Bernstein, E.R. Investigation of the reactions of small neutral iron oxide clusters with methanol. *J. Chem. Phys.* **2009**, *130*, 114306. [[CrossRef](#)]
275. Yan, B.; Li, L.; Yu, Q.; Hang, W.; He, J.; Huang, B. High irradiance laser ionization mass spectrometry for direct speciation of iron oxides. *J. Am. Soc. Mass Spectrom.* **2010**, *21*, 1227–1234. [[CrossRef](#)]
276. Zeth, K.; Offermann, S.; Essen, L.O.; Oesterhelt, D. Iron-oxo clusters biomimeticizing on protein surfaces: Structural analysis of Halobacterium salinarum DpsA in its low- and high-iron states. *Proc. Natl. Acad. Sci. USA* **2004**, *101*, 13780–13785. [[CrossRef](#)]
277. Zeth, K. Dps biomimeticizing proteins: Multifunctional architects of nature. *Biochem. J.* **2012**, *445*, 297–311. [[CrossRef](#)] [[PubMed](#)]
278. Lyons, M.E.G.; Doyle, R.L.; Brandon, M.P. Redox switching and oxygen evolution at oxidized metal and metal oxide electrodes: Iron in base. *Phys. Chem. Chem. Phys.* **2011**, *13*, 21530–21551. [[CrossRef](#)]
279. Weng, X.; Jin, X.; Lin, J.; Naidu, R.; Chen, Z. Removal of mixed contaminants Cr(VI) and Cu(II) by green synthesized iron based nanoparticles. *Ecol. Eng.* **2016**, *97*, 32–39. [[CrossRef](#)]
280. Soldemo, M.; Lundgren, E.; Weissenrieder, J. Oxidation of Fe(110) in oxygen gas at 400 °C. *Surf. Sci.* **2016**, *644*, 172–179. [[CrossRef](#)]
281. Barcaro, G.; Monti, S. Modeling generation and growth of iron oxide nanoparticles from representative precursors through ReaxFF molecular dynamics. *Nanoscale* **2020**, *12*, 3103–3111. [[CrossRef](#)]
282. Ai, L.; Zhou, Y.; Chen, M. Role of Dissolved Oxygen in Iron Oxidation in Supercritical Water: Insights from Reactive Dynamics Simulations. *J. Phys. Chem. C* **2019**, *123*, 15009–15016. [[CrossRef](#)]
283. Kim, C.; Ahn, J.Y.; Kim, T.Y.; Hwang, I. Mechanisms of electro-assisted persulfate/nano-Fe0 oxidation process: Roles of redox mediation by dissolved Fe. *J. Hazard. Mater.* **2020**, *388*, 121739. [[CrossRef](#)] [[PubMed](#)]
284. O'Neill, H.A.; Gakh, O.; Park, S.; Cui, J.; Mooney, S.M.; Sampson, M.; Ferreira, G.C.; Isaya, G. Assembly of human frataxin is a mechanism for detoxifying redox-active iron. *Biochemistry* **2005**, *44*, 537–545. [[CrossRef](#)] [[PubMed](#)]
285. Palchoudhury, S.; An, W.; Xu, Y.; Qin, Y.; Zhang, Z.; Chopra, N.; Holler, R.A.; Turner, C.H.; Bao, Y. Synthesis and growth mechanism of iron oxide nanowhiskers. *Nano Lett.* **2011**, *11*, 1141–1146. [[CrossRef](#)] [[PubMed](#)]
286. Panda, C.; Debupta, J.; Díaz, D.D.; Singh, K.K.; Gupta, S.S.; Dhar, B.B. Homogeneous photochemical water oxidation by biuret-modified Fe-TAML: Evidence of FeV(O) intermediate. *J. Am. Chem. Soc.* **2014**, *136*, 12273–12282. [[CrossRef](#)] [[PubMed](#)]
287. Sun, Y.; Zuo, X.; Sankaranarayanan, S.K.R.S.; Peng, S.; Narayanan, B.; Kamath, G. Quantitative 3D evolution of colloidal nanoparticle oxidation in solution. *Science* **2017**, *356*, 303–307. [[CrossRef](#)]
288. Tamura, K.; Kunoh, T.; Nakanishi, M.; Kusano, Y.; Takada, J. Preparation and characterization of additional metallic element-containing tubular iron oxides of bacterial origin. *ACS Omega* **2020**, *5*, 27287–27294. [[CrossRef](#)]
289. Tian, B.; Świątowska, J.; Maurice, V.; Zanna, S.; Seyeux, A.; Klein, L.H.; Marcus, P. Combined surface and electrochemical study of the lithiation/delithiation mechanism of the iron oxide thin-film anode for lithium-ion batteries. *J. Phys. Chem. C* **2013**, *117*, 21651–21661. [[CrossRef](#)]
290. Walker, J.D.; Tannenbaum, R. Characterization of the sol-gel formation of iron(III) oxide/hydroxide nanonetworks from weak base molecules. *Chem. Mater.* **2006**, *18*, 4793–4801. [[CrossRef](#)]
291. Wang, T.; Lin, J.; Chen, Z.; Megharaj, M.; Naidu, R. Green synthesized iron nanoparticles by green tea and eucalyptus leaves extracts used for removal of nitrate in aqueous solution. *J. Clean. Prod.* **2014**, *83*, 413–419. [[CrossRef](#)]
292. Wu, X.; Wei, Y.; Wang, J.; Wang, D.; She, L.; Wang, J.; Cai, C. Effects of soil physicochemical properties on aggregate stability along a weathering gradient. *Catena* **2017**, *156*, 205–215. [[CrossRef](#)]

293. Zhu, H.; Wang, L.; Li, J.; Zhao, J.; Yu, Y. Effects of metallurgical factors on reticular crack formations in Nb-bearing pipeline steel. *High Temp. Mater. Process.* **2020**, *39*, 81–87. [[CrossRef](#)]
294. Gareev, K.G.; Grouzdev, D.S.; Kharitonskii, P.V.; Kirilenko, D.A.; Kosterov, A.; Kozaeva, V.V.; Levitskii, V.S.; Multhoff, G.; Nepomnyashchaya, E.K.; Nikitin, A.V.; et al. Magnetic properties of bacterial magnetosomes produced by magnetospirillum caucaseum so-1. *Microorganisms* **2021**, *9*, 1854. [[CrossRef](#)]
295. Grevey, A.L.; Vignal, V.; Krawiec, H.; Ozga, P.; Peche-Quilichini, K.; Rivalan, A.; Mazière, F. Microstructure and long-term corrosion of archaeological iron alloy artefacts. *Herit. Sci.* **2020**, *8*, 57. [[CrossRef](#)]
296. Bi, J.; Tao, Q.; Ren, J.; Huang, X.; Wang, T.; Hao, H. P25-inspired α/γ -Fe₂O₃ isolement heterostructures for visible-light photocatalysis: Optimization of crystalline ratios and mechanism investigation. *J. Alloys Compd.* **2023**, *937*, 168422. [[CrossRef](#)]
297. Ghafarpour, A.; Khormali, F.; Balsam, W.; Forman, S.L.; Cheng, L.; Song, Y. The formation of iron oxides and magnetic enhancement mechanisms in northern Iranian loess-paleosol sequences: Evidence from diffuse reflectance spectrophotometry and temperature dependence of magnetic susceptibility. *Quat. Int.* **2021**, *589*, 68–82. [[CrossRef](#)]
298. Long, X.; Ji, J.; Balsam, W. Rainfall-dependent transformations of iron oxides in a tropical saprolite transect of Hainan Island, South China: Spectral and magnetic measurements. *J. Geophys. Res. Earth Surf.* **2011**, *116*, F03015. [[CrossRef](#)]
299. Anju, M.; Renuka, N.K. A novel template free synthetic strategy to graphene-iron oxide nanotube hybrid. *RSC Adv.* **2015**, *5*, 78648–78654. [[CrossRef](#)]
300. Patel, S.; Hota, G. Iron oxide nanoparticle-immobilized PAN nanofibers: Synthesis and adsorption studies. *RSC Adv.* **2016**, *6*, 15402–15414. [[CrossRef](#)]
301. Sousa, L.S.; Chagas, P.; Oliveira, L.C.A.D.; Castro, C.S.D. Carbon/FexOy magnetic composites obtained from PET and red mud residues: Paracetamol and dye oxidation. *Environ. Technol.* **2019**, *40*, 2840–2852. [[CrossRef](#)]
302. Hernández-Espejel, A.; Palomar-Pardavé, M.; Cabrera-Sierra, R.; Romero-Romo, M.; Ramírez-Silva, M.T.; Arce-Estrada, E.M. Kinetics and mechanism of the electrochemical formation of iron oxidation products on steel immersed in sour acid media. *J. Phys. Chem. B* **2011**, *115*, 1833–1841. [[CrossRef](#)]
303. Angerer, T.; Thorne, W.; Hagemann, S.G.; Tribus, M.; Evans, N.J.; Savard, D. Iron oxide chemistry supports a multistage hydrothermal genesis of BIF-hosted hematite ore in the Mt. Tom Price and Mt. Whaleback deposits. *Ore Geol. Rev.* **2022**, *144*, 104840. [[CrossRef](#)]
304. Ebotehoua, C.G.; Xie, Y.; Adomako-Ansah, K.; Gourcerol, B.; Qu, Y. Depositional environment and genesis of the nabeba banded iron formation (Bif) in the ivindo basement complex, republic of the congo: Perspective from whole-rock and magnetite geochemistry. *Minerals* **2021**, *11*, 579. [[CrossRef](#)]
305. Egglseder, M.S.; Cruden, A.R.; Dalstra, H.J.; Nicholas, L. The role of deformation in the formation of banded iron formation-hosted high-grade iron ore deposits, Hamersley Province (Australia). *Precambrian Res.* **2017**, *296*, 62–77. [[CrossRef](#)]
306. Kreiner, D.C.; Barton, M.D. Sulfur-poor intense acid hydrothermal alteration: A distinctive hydrothermal environment. *Ore Geol. Rev.* **2017**, *88*, 174–187. [[CrossRef](#)]
307. Mercer, C.N.; Watts, K.E.; Gross, J. Apatite trace element geochemistry and cathodoluminescent textures—A comparison between regional magmatism and the Pea Ridge IOAREE and Boss IOCG deposits, southeastern Missouri iron metallogenic province, USA. *Ore Geol. Rev.* **2020**, *116*, 103129. [[CrossRef](#)]
308. Sheshukov, O.Y.; Mikheenkov, M.A.; Vyaznikova, E.A.; Bykov, A.S.; Vedmid', L.B. Changes in phase composition of soderites of the bakal deposit at heating. *Izv. Ferr. Metall.* **2018**, *61*, 891–897. [[CrossRef](#)]
309. Sun, S.; Konhauser, K.O.; Kappler, A.; Li, Y.L. Primary hematite in Neoarchean to Paleoproterozoic oceans. *GSA Bull.* **2015**, *127*, 850–861. [[CrossRef](#)]
310. Fischer, W.W.; Knoll, A.H. An iron shuttle for deepwater silica in late Archean and early Paleoproterozoic iron formation. *GSA Bull.* **2009**, *121*, 222–235. [[CrossRef](#)]
311. Rego, E.S.; Busigny, V.; Lalonde, S.V.; Philippot, P.; Bouyon, A.; Rossignol, C.; Babinski, M.; de Cássia Zapparoli, A. Anoxygenic photosynthesis linked to Neoarchean iron formations in Carajás (Brazil). *Geobiology* **2021**, *19*, 326–341. [[CrossRef](#)]
312. Ali, G.; Park, Y.J.; Hussain, A.; Cho, S.O. A novel route to the formation of 3D nanoflower-like hierarchical iron oxide nanostructure. *Nanotechnology* **2019**, *30*, 095601. [[CrossRef](#)]
313. Cao, S.W.; Zhu, Y.J. Iron oxide hollow spheres: Microwave-hydrothermal ionic liquid preparation, formation mechanism, crystal phase and morphology control and properties. *Acta Mater.* **2009**, *57*, 2154–2165. [[CrossRef](#)]
314. Gracien, E.B.; Ruimin, Z.; LiHui, X.; Kanza, L.K.; Lopaka, I. Effects of pH on the morphology of iron oxides synthesized under gamma-irradiation. *J. Radioanal. Nucl. Chem.* **2006**, *270*, 473–478. [[CrossRef](#)]
315. Alemani, M.; Gialanella, S.; Straffolini, G.; Ciudin, R.; Olofsson, U.; Perricone, G.; Metinoz, I. Dry sliding of a low steel friction material against cast iron at different loads: Characterization of the friction layer and wear debris. *Wear* **2017**, *376–377*, 1450–1459. [[CrossRef](#)]
316. Fatimah, I.; Amaliah, S.N.; Andrian, M.F.; Handayani, T.P.; Nurillahi, R.; Prakoso, N.I.; Wicaksono, W.P.; Chuenchom, L. Iron oxide nanoparticles supported on biogenic silica derived from bamboo leaf ash for rhodamine B photodegradation. *Sustain. Chem. Pharm.* **2019**, *13*, 100149. [[CrossRef](#)]
317. Lim, J.H.; Min, S.G.; Malkinski, L.; Wiley, J.B. Iron oxide nanotubes synthesized via template-based electrodeposition. *Nanoscale* **2014**, *6*, 5289–5295. [[CrossRef](#)]

318. Aligizaki, K.K.; De Rooij, M.R.; Macdonald, D.D. Analysis of iron oxides accumulating at the interface between aggregates and cement paste. *Cem. Concr. Res.* **2000**, *30*, 1941–1945. [[CrossRef](#)]
319. Budiman, F.; Kian, T.W.; Razak, K.A.; Matsuda, A.; Lockman, Z. The Assessment of Cr(VI) Removal by Iron Oxide Nanosheets and Nanowires Synthesized by Thermal Oxidation of Iron in Water Vapour. *Procedia Chem.* **2016**, *19*, 586–593. [[CrossRef](#)]
320. Carranza, E.J.M.; de Souza Filho, C.R.; Haddad-Martim, P.M.; Katsuta, N.; Shimizu, I. Macro-scale ore-controlling faults revealed by micro-geochemical anomalies. *Sci. Rep.* **2019**, *9*, 4410. [[CrossRef](#)] [[PubMed](#)]
321. Ershov, B.G. Radiation-induced oxidation of iron in the ocean of the early Earth. *Precambrian Res.* **2021**, *364*, 106360. [[CrossRef](#)]
322. Gaikwad, V.; Badesab, F.; Dewangan, P.; Kotha, M. Diagenesis of Magnetic Minerals in Active/Relict Methane Seep: Constraints From Rock Magnetism and Mineralogical Records From Bay of Bengal. *Front. Earth Sci.* **2021**, *9*, 638594. [[CrossRef](#)]
323. Huang, R.; Lin, C.T.; Sun, W.; Ding, X.; Zhan, W.; Zhu, J. The production of iron oxide during peridotite serpentinization: Influence of pyroxene. *Geosci. Front.* **2017**, *8*, 1311–1321. [[CrossRef](#)]
324. Johnston, C.J.; Pepper, R.A.; Martens, W.N.; Couperthwaite, S. Improvement of aluminium extraction from low-grade kaolinite by iron oxide impurities: Role of clay chemistry and morphology. *Miner. Eng.* **2022**, *176*, 107346. [[CrossRef](#)]
325. Konhauser, K.O.; Amskold, L.; Lalonde, S.V.; Posth, N.R.; Kappler, A.; Anbar, A. Decoupling photochemical Fe(II) oxidation from shallow-water BIF deposition. *Earth Planet. Sci. Lett.* **2007**, *258*, 87–100. [[CrossRef](#)]
326. Levett, A.; Gagen, E.; Paz, A.; Vasconcelos, P.; Southam, G. Strategising the bioremediation of Brazilian iron ore mines. *Crit. Rev. Environ. Sci. Technol.* **2022**, *52*, 2749–2771. [[CrossRef](#)]
327. Liu, Z.; Zheng, Y. Effect of Fe(II) on the formation of iron oxide synthesized from pyrite cinders by hydrothermal process. *Powder Technol.* **2011**, *209*, 119–123. [[CrossRef](#)]
328. Ohmoto, H. Nonredox transformations of magnetite-hematite in hydrothermal systems. *Econ. Geol.* **2003**, *98*, 157–161. [[CrossRef](#)]
329. Boulard, E.; Menguy, N.; Auzende, A.L.; Benzerara, K.; Bureau, H.; Antonangeli, D.; Corgne, A.; Morard, G.; Siebert, J.; Perrillat, J.P.; et al. Experimental investigation of the stability of Fe-rich carbonates in the lower mantle. *J. Geophys. Res. Solid Earth* **2012**, *117*, B02208. [[CrossRef](#)]
330. Matthew, S.P.; Cho, T.R.; Hayes, P.C. Mechanisms of porous iron growth on wustite and magnetite during gaseous reduction. *Metall. Trans. B* **1990**, *21*, 733–741. [[CrossRef](#)]
331. Meng, S.; Wu, J.; Zhao, L.; Zheng, H.; Jia, S.; Hu, S.; Meng, W.; Pu, S.; Zhao, D.; Wang, J. Atomistic Insight into the Redox Reactions in Fe/Oxide Core-Shell Nanoparticles. *Chem. Mater.* **2018**, *30*, 7306–7312. [[CrossRef](#)]
332. Cotin, G.; Kiefer, C.; Perton, F.; Ihiawakrim, D.; Blanco-Andujar, C.; Moldovan, S.; Lefevre, C.; Ersen, O.; Pichon, B.; Mertz, D.; et al. Unravelling the thermal decomposition parameters for the synthesis of anisotropic iron oxide nanoparticles. *Nanomaterials* **2018**, *8*, 881. [[CrossRef](#)]
333. Glasgow, W.; Fellows, B.; Qi, B.; Darroudi, T.; Kitchens, C.; Ye, L.; Crawford, T.M.; Mefford, O.T. Continuous synthesis of iron oxide (Fe_3O_4) nanoparticles via thermal decomposition. *Particuology* **2016**, *26*, 47–53. [[CrossRef](#)]
334. Miguel-Sancho, N.; Bomati-Miguel, O.; Roca, A.G.; Martinez, G.; Arruebo, M.; Santamaría, J. Synthesis of magnetic nanocrystals by thermal decomposition in glycol media: Effect of process variables and mechanistic study. *Ind. Eng. Chem. Res.* **2012**, *51*, 8348–8357. [[CrossRef](#)]
335. Nandakumaran, N.; Barnsley, L.; Feoktystov, A.; Ivanov, S.A.; Huber, D.L.; Fruhner, L.S.; Leffler, V.; Ehlert, S.; Kentzinger, E.; Qdemat, A.; et al. Unravelling Magnetic Nanochain Formation in Dispersion for in Vivo Applications. *Adv. Mater.* **2021**, *33*, 2008683. [[CrossRef](#)] [[PubMed](#)]
336. Pušnik, K.; Goršák, T.; Drofenik, M.; Makovec, D. Synthesis of aqueous suspensions of magnetic nanoparticles with the co-precipitation of iron ions in the presence of aspartic acid. *J. Magn. Magn. Mater.* **2016**, *413*, 65–75. [[CrossRef](#)]
337. Vogt, C.; Toprak, M.S.; Muhammed, M.; Laurent, S.; Bridot, J.L.; Müller, R.N. High quality and tuneable silica shell-magnetic core nanoparticles. *J. Nanoparticle Res.* **2010**, *12*, 1137–1147. [[CrossRef](#)]
338. Wen, J.Z.; Richter, H.; Green, W.H.; Howard, J.B.; Treska, M.; Jardim, P.M.; Sande, J.B.V. Experimental study of catalyst nanoparticle and single walled carbon nanotube formation in a controlled premixed combustion. *J. Mater. Chem.* **2008**, *18*, 1561–1569. [[CrossRef](#)]
339. Chen, Z. Size and shape controllable synthesis of monodisperse iron oxide nanoparticles by thermal decomposition of iron oleate complex. *Synth. React. Inorganic Metal Nano-Metal Chem.* **2012**, *42*, 1040–1046. [[CrossRef](#)]
340. Besenhard, M.O.; Lagrow, A.P.; Famiani, S.; Pucciarelli, M.; Lettieri, P.; Thanh, N.T.K.; Gavriilidis, A. Continuous production of iron oxide nanoparticles: Via fast and economical high temperature synthesis. *React. Chem. Eng.* **2020**, *5*, 1474–1483. [[CrossRef](#)]
341. Lin, J.; He, F.; Su, B.; Sun, M.; Owens, G.; Chen, Z. The stabilizing mechanism of cadmium in contaminated soil using green synthesized iron oxide nanoparticles under long-term incubation. *J. Hazard. Mater.* **2019**, *379*, 120832. [[CrossRef](#)]
342. Slimani, S.; Meneghini, C.; Abdolrahimi, M.; Talone, A.; Murillo, J.P.M.; Barucca, G.; Yaacoub, N.; Imperatori, P.; Illés, E.; Smari, M.; et al. Spinel iron oxide by the co-precipitation method: Effect of the reaction atmosphere. *Appl. Sci.* **2021**, *11*, 5433. [[CrossRef](#)]
343. Bernard, M.C.; Joiret, S. Understanding corrosion of ancient metals for the conservation of cultural heritage. *Electrochim. Acta* **2009**, *54*, 5199–5205. [[CrossRef](#)]
344. Leon, Y.; Saheb, M.; Drouet, E.; Neff, D.; Foy, E.; Leroy, E.; Dynes, J.J.; Dillmann, P. Interfacial layer on archaeological mild steel corroded in carbonated anoxic environments studied with coupled micro and nano probes. *Corros. Sci.* **2014**, *88*, 23–35. [[CrossRef](#)]
345. Grosvenor, A.P.; Kobe, B.A.; McIntyre, N.S. Examination of the oxidation of iron by oxygen using X-ray photoelectron spectroscopy and QUASESTM. *Surf. Sci.* **2004**, *565*, 151–162. [[CrossRef](#)]

346. Monnier, J.; Réguer, S.; Foy, E.; Testemale, D.; Mirambet, F.; Saheb, M.; Dillmann, P.; Guillot, I. XAS and XRD in situ characterisation of reduction and reoxidation processes of iron corrosion products involved in atmospheric corrosion. *Corros. Sci.* **2014**, *78*, 293–303. [[CrossRef](#)]
347. Ohtsuka, T.; Fushimi, K. Optical characterization of passive oxides on metals. *Electrochemistry* **2016**, *84*, 826–832. [[CrossRef](#)]
348. Velimirovic, M.; Auffan, M.; Carniato, L.; Batka, V.M.; Schmid, D.; Wagner, S.; Borschneck, D.; Proux, O.; von der Kammer, F.; Hofmann, T. Effect of field site hydrogeochemical conditions on the corrosion of milled zerovalent iron particles and their dechlorination efficiency. *Sci. Total Environ.* **2018**, *618*, 1619–1627. [[CrossRef](#)]
349. Sánchez-Moreno, M.; Takenouti, H.; García-Jareño, J.J.; Vicente, F.; Alonso, C. A theoretical approach of impedance spectroscopy during the passivation of steel in alkaline media. *Electrochim. Acta* **2009**, *54*, 7222–7226. [[CrossRef](#)]
350. Song, Y.; Wightman, E.; Tian, Y.; Jack, K.; Li, X.; Zhong, H.; Bond, P.L.; Yuan, Z.; Jiang, G. Corrosion of reinforcing steel in concrete sewers. *Sci. Total Environ.* **2019**, *649*, 739–748. [[CrossRef](#)]
351. Silva-Bedoya, L.M.; Watkin, E.; Machuca, L.L. Deep-sea corrosion rusticles from iron-hulled shipwrecks. *Mater. Corros.* **2021**, *72*, 1138–1151. [[CrossRef](#)]
352. Bautista-Guzman, J.; Gomez-Morales, R.; Asmat-Campos, D.; Checca, N.R. Influence of the alcoholic/ethanolic extract of mangifera indica residues on the green synthesis of feo nanoparticles and their application for the remediation of agricultural soils. *Molecules* **2021**, *26*, 7633. [[CrossRef](#)]
353. Gallo-Cordova, A.; Castro, J.J.; Winkler, E.L.; Lima, E.; Zysler, R.D.; Morales, M.D.P.; Ovejero, J.G.; Streitwieser, D.A. Improving degradation of real wastewaters with self-heating magnetic nanocatalysts. *J. Clean. Prod.* **2021**, *308*, 127385. [[CrossRef](#)]
354. Kastrinaki, G.; Lorentzou, S.; Karagiannakis, G.; Rattenbury, M.; Woodhead, J.; Konstandopoulos, A.G. Parametric synthesis study of iron based nanoparticles via aerosol spray pyrolysis route. *J. Aerosol. Sci.* **2018**, *115*, 96–107. [[CrossRef](#)]
355. Lagrow, A.P.; Besenhard, M.O.; Hodzic, A.; Sergides, A.; Bogart, L.K.; Gavriilidis, A.; Thanh, N.T.K. Unravelling the growth mechanism of the co-precipitation of iron oxide nanoparticles with the aid of synchrotron X-ray diffraction in solution. *Nanoscale* **2019**, *11*, 6620–6628. [[CrossRef](#)]
356. Patiño-Ruiz, D.A.; De Ávila, G.; Alarcón-Suesca, C.; González-Delgado, Á.D.; Herrera, A. Ionic cross-linking fabrication of chitosan-based beads modified with FeO and TiO₂ nanoparticles: Adsorption mechanism toward naphthalene removal in seawater from cartagena bay area. *ACS Omega* **2020**, *5*, 26463–26475. [[CrossRef](#)]
357. Ramkumar, J.; Majeed, J.; Chandramouleeswaran, S. Insight to sorption mechanism employing nanocomposite: Case study of toxic species removal. *Microporous Mesoporous Mater.* **2021**, *314*, 110858. [[CrossRef](#)]
358. Abutalib, N.H.; Lagrow, A.P.; Besenhard, M.O.; Bondarchuk, O.; Sergides, A.; Famiani, S.; Ferreira, L.P.; Cruz, M.M.; Gavriilidis, A.; Thanh, N.T.K. Shape controlled iron oxide nanoparticles: Inducing branching and controlling particle crystallinity. *CrystEngComm* **2021**, *23*, 550–561. [[CrossRef](#)]
359. Gerber, O.; Pichon, B.P.; Ihiawakrim, D.; Florea, I.; Moldovan, S.; Ersen, O.; Begin, D.; Grenèche, J.M.; Lemonnier, S.; Barraud, E.; et al. Synthesis engineering of iron oxide raspberry-shaped nanostructures. *Nanoscale* **2017**, *9*, 305–313. [[CrossRef](#)]
360. Hu, Z.; Nourafkan, E.; Gao, H.; Wen, D. Microemulsions stabilized by in-situ synthesized nanoparticles for enhanced oil recovery. *Fuel* **2017**, *210*, 272–281. [[CrossRef](#)]
361. Ruiz-Baltazar, A.; Esparza, R.; Rosas, G.; Pérez, R. Effect of the Surfactant on the Growth and Oxidation of Iron Nanoparticles. *J. Nanomater.* **2015**, *2015*, 240948. [[CrossRef](#)]
362. Suppiah, D.D.; Johan, M.R. Influence of solution pH on the formation of iron oxide nanoparticles. *Mater. Res. Express* **2019**, *6*, 015008. [[CrossRef](#)]
363. Buonsanti, R.; Grillo, V.; Carlino, E.; Giannini, C.; Gozzo, F.; Garcia-Hernandez, M.; Garcia, M.A.; Cingolani, R.; Cozzoli, P.D. Architectural control of seeded-grown magnetic-semiconductor iron oxide-TiO₂ nanorod heterostructures: The role of seeds in topology selection. *J. Am. Chem. Soc.* **2010**, *132*, 2437–2464. [[CrossRef](#)]
364. Briones, F.C.; Guerrero-Contreras, J.; Benito-Santiago, S.E.; Llamazares, J.L.S.; Espinosa-Faller, F.J. Formation of magnetic nanoscrolls and nanoribbons in iron oxide-decorated graphene oxide. *Mater. Lett.* **2022**, *309*, 131321. [[CrossRef](#)]
365. Cao, S.W.; Zhu, Y.J. Surfactant-free preparation and drug release property of magnetic hollow core/shell hierarchical nanostructures. *J. Phys. Chem. C* **2008**, *112*, 12149–12156. [[CrossRef](#)]
366. Abou-Elanwar, A.M.; Shirke, Y.M.; Yoo, C.H.; Kwon, S.J.; Choi, W.K.; Lee, J.S.; Hong, S.U.; Lee, H.K.; Jeon, J.D. Water vapor dehumidification using thin-film nanocomposite membranes by the in situ formation of ultrasmall size iron-chelated nanoparticles. *Appl. Surf. Sci.* **2021**, *542*, 148562. [[CrossRef](#)]
367. Aslan, T.N. Relaxivity properties of magnetoferitin: The iron loading effect. *J. Biosci. Bioeng.* **2022**, *133*, 474–480. [[CrossRef](#)]
368. Acevedo, P.G.; Gómez, M.A.G.; Prieto, Á.A.; Garitaonandia, J.S.; Piñeiro, Y.; Rivas, J. Significant Surface Spin Effects and Exchange Bias in Iron Oxide-Based Hollow Magnetic Nanoparticles. *Nanomaterials* **2022**, *12*, 456. [[CrossRef](#)]
369. Badri, W.; Tarhini, M.; Lgourna, Z.; Lebaz, N.; Saadaoui, H.; Zine, N.; Errachid, A.; Elaissari, A. Preparation and Characterization of Glued Corn Flakes-Like Protein-Based Magnetic Particles. *Chem. Afr.* **2020**, *3*, 803–811. [[CrossRef](#)]
370. Giardiello, M.; Hatton, F.L.; Slater, R.A.; Chambon, P.; North, J.; Peacock, A.K.; He, T.; McDonald, T.O.; Owen, A.; Rannard, S.P. Stable, polymer-directed and SPION-nucleated magnetic amphiphilic block copolymer nanoprecipitates with readily reversible assembly in magnetic fields. *Nanoscale* **2016**, *8*, 7224–7231. [[CrossRef](#)]
371. Kim, J.D.; Yee, N.; Nanda, V.; Falkowski, P.G. Anoxic photochemical oxidation of siderite generates molecular hydrogen and iron oxides. *Proc. Natl. Acad. Sci. USA* **2013**, *110*, 10073–10077. [[CrossRef](#)]

372. Li, M.; Fu, S.; Cai, Z.; Li, D.; Liu, L.; Deng, D.; Jin, R.; Ai, H. Dual regulation of osteoclastogenesis and osteogenesis for osteoporosis therapy by iron oxide hydroxyapatite core/shell nanocomposites. *Regen. Biomater.* **2021**, *8*, rbab027. [[CrossRef](#)]
373. Singh, N.; Riyajuddin, S.; Ghosh, K.; Mehta, S.K.; Dan, A. Chitosan-Graphene Oxide Hydrogels with Embedded Magnetic Iron Oxide Nanoparticles for Dye Removal. *ACS Appl. Nano Mater.* **2019**, *2*, 7379–7392. [[CrossRef](#)]
374. Wu, Y.; Yu, H.; Peng, F.; Wang, H. Facile synthesis of porous hollow iron oxide nanoparticles supported on carbon nanotubes. *Mater. Lett.* **2012**, *67*, 245–247. [[CrossRef](#)]
375. Zhang, C.; Liu, S.; Phelps, T.J.; Cole, D.R.; Horita, J.; Fortier, S.M.; Elless, M.; Valley, J.W. Physiochemical, mineralogical, and isotopic characterization of magnetite-rich iron oxides formed by thermophilic iron-reducing bacteria. *Geochim. Cosmochim. Acta* **1997**, *61*, 4621–4632. [[CrossRef](#)]
376. Zhao, H.; Wang, Y.; Wang, Y.; Cao, T.; Zhao, G. Electro-Fenton oxidation of pesticides with a novel $\text{Fe}_3\text{O}_4@\text{Fe}_2\text{O}_3$ /activated carbon aerogel cathode: High activity, wide pH range and catalytic mechanism. *Appl. Catal. B Environ.* **2012**, *125*, 120–127. [[CrossRef](#)]
377. Zou, Y.; Ito, S.; Fujiwara, M.; Komatsu, N. Probing the Role of Charged Functional Groups on Nanoparticles Grafted with Polyglycerol in Protein Adsorption and Cellular Uptake. *Adv. Funct. Mater.* **2022**, *32*, 2111077. [[CrossRef](#)]
378. Wlokas, I.; Faccinetto, A.; Tribalet, B.; Schulz, C.; Kempf, A. Mechanism of iron oxide formation from iron pentacarbonyl-doped low-pressure hydrogen/oxygen flames. *Int. J. Chem. Kinet.* **2013**, *45*, 487–498. [[CrossRef](#)]
379. Zhu, W.; Winterstein, J.; Maimon, I.; Yin, Q.; Yuan, L.; Kolmogorov, A.N.; Sharma, R.; Zhou, G. Atomic structural evolution during the reduction of $\alpha\text{-Fe}_2\text{O}_3$ nanowires. *J. Phys. Chem. C* **2016**, *120*, 14854–14862. [[CrossRef](#)]
380. Kim, D.-Y.; Yoon, S.-S.; Takahashi, M. Study on Formation Mechanism of Iron Oxide Nanoparticles. *J. Korean Magn. Soc.* **2012**, *22*, 167–172. [[CrossRef](#)]
381. Lin, J.; Sun, M.; Su, B.; Owens, G.; Chen, Z. Immobilization of cadmium in polluted soils by phytogenic iron oxide nanoparticles. *Sci. Total Environ.* **2019**, *659*, 491–498. [[CrossRef](#)]
382. Ning, D.; Shoshin, Y.; van Stiphout, M.; van Oijen, J.; Finotello, G.; de Goey, P. Temperature and phase transitions of laser-ignited single iron particle. *Combust. Flame* **2022**, *236*, 111801. [[CrossRef](#)]
383. Fang, G.; Ding, W.; Liu, Y.; Zhang, J.; Xing, F.; Dong, B. Identification of corrosion products and 3D distribution in reinforced concrete using X-ray micro computed tomography. *Constr. Build. Mater.* **2019**, *207*, 304–315. [[CrossRef](#)]
384. Moloko, K.G.; Van Der Merwe, J.W. Investigation of the mechanism for fireside corrosion in coal-fired boilers in South Africa. *J. S. Afr. Inst. Min. Metall.* **2021**, *121*, 305–316. [[CrossRef](#)]
385. Pilić, Z.; Martinović, I. Electrochemical behaviour of iron and AISI 304 stainless steel in simulated acid rain solution. *Int. J. Mater. Res.* **2016**, *107*, 925–934. [[CrossRef](#)]
386. Ishizaka, K.; Lewis, S.R.; Hammond, D.; Lewis, R. Chemistry of black leaf films synthesised using rail steels and their influence on the low friction mechanism. *RSC Adv.* **2018**, *8*, 32506–32521. [[CrossRef](#)]
387. Melfo, W.M.; Dippenaar, R.J. In situ observations of early oxide formation in steel under hot-rolling conditions. *J. Microsc.* **2007**, *225*, 147–155. [[CrossRef](#)]
388. Kelly, H.; Spilde, M.N.; Jones, D.S.; Boston, P.J. Insights into the geomicrobiology of biovermiculations from rock billet incubation experiments. *Life* **2021**, *11*, 59. [[CrossRef](#)]
389. Peng, X.; Zhou, H.; Li, J.; Li, J.; Chen, S.; Yao, H.; Wu, Z. Intracellular and extracellular mineralization of a microbial community in the Edmond deep-sea vent field environment. *Sediment. Geol.* **2010**, *229*, 193–206. [[CrossRef](#)]
390. Levett, A.; Gagen, E.J.; Southam, G. Small but mighty: Microorganisms offer inspiration for mine remediation and waste stabilisation. *Microbiol. Aust.* **2019**, *40*, 190–194. [[CrossRef](#)]
391. Walter, X.A.; Picazo, A.; Miracle, M.R.; Vicente, E.; Camacho, A.; Aragno, M.; Zopfi, J. Phototrophic Fe(II)-oxidation in the chemocline of a ferruginous meromictic lake. *Front. Microbiol.* **2014**, *5*, 713. [[CrossRef](#)]
392. Zeng, Z.; Tice, M.M. Electron Transfer Strategies Regulate Carbonate Mineral and Micropore Formation. *Astrobiology* **2018**, *18*, 28–36. [[CrossRef](#)]
393. Bulavchenko, O.A.; Vinokurov, Z.S.; Saraev, A.A.; Tsapina, A.M.; Trigub, A.L.; Gerasimov, E.Y.; Gladky, A.Y.; Fedorov, A.V.; Yakovlev, V.A.; Kachev, V.V. The Influence of Cu and Al Additives on Reduction of Iron(III) Oxide: In Situ XRD and XANES Study. *Inorg. Chem.* **2019**, *58*, 4842–4850. [[CrossRef](#)]
394. Coombes, M.J.; Olivier, E.J.; Prestat, E.; Haigh, S.J.; du Plessis, E.; Neethling, J.H. Iron-silica interaction during reduction of precipitated silica-promoted iron oxides using in situ XRD and TEM. *Appl. Catal. A Gen.* **2021**, *613*, 118031. [[CrossRef](#)]
395. Yu, G.; Sun, B.; Pei, Y.; Xie, S.; Yan, S.; Qiao, M.; Fan, K.; Zhang, X.; Zong, B. $\text{Fe}_{\text{x}}\text{O}_{\text{y}}@\text{C}$ spheres as an excellent catalyst for Fischer-Tropsch synthesis. *J. Am. Chem. Soc.* **2010**, *132*, 935–937. [[CrossRef](#)]
396. Bica, I.; Anitas, E.M.; Anitas, E.M.; Choi, H.J.; Sfirloaga, P. Microwave-assisted synthesis and characterization of iron oxide microfibers. *J. Mater. Chem. C* **2020**, *8*, 6159–6167. [[CrossRef](#)]
397. Xu, Z.; Wan, Z.; Sun, Y.; Cao, X.; Hou, D.; Alessi, D.S.; Ok, Y.S.; Tsang, D.C.W. Unraveling iron speciation on Fe-biochar with distinct arsenic removal mechanisms and depth distributions of As and Fe. *Chem. Eng. J.* **2021**, *425*, 131489. [[CrossRef](#)]
398. Wang, T.; Tian, Z.; Tunlid, A.; Persson, P. Nitrogen acquisition from mineral-associated proteins by an ectomycorrhizal fungus. *New Phytol.* **2020**, *228*, 697–711. [[CrossRef](#)]
399. Celi, L.; Prati, M.; Magnacca, G.; Santoro, V.; Martin, M. Role of crystalline iron oxides on stabilization of inositol phosphates in soil. *Geoderma* **2020**, *374*, 114442. [[CrossRef](#)]

400. Agrawal, S.; Dhawan, N. Investigation of carbothermic microwave reduction followed by acid leaching for recovery of iron and aluminum values from Indian red mud. *Miner. Eng.* **2020**, *159*, 106653. [[CrossRef](#)]
401. Dong, Q.; Li, X.; Wang, Z.; Bi, Y.; Yang, R.; Zhang, J.; Luo, H.; Niu, M.; Qi, B.; Lu, C. Effect of iron(III) ion on moso bamboo pyrolysis under microwave irradiation. *Bioresour. Technol.* **2017**, *243*, 755–759. [[CrossRef](#)]
402. Hamed, M.H.; Mueller, D.N.; Müller, M. Thermal phase design of ultrathin magnetic iron oxide films: From Fe_3O_4 to $\gamma\text{-Fe}_2\text{O}_3$ and FeO . *J. Mater. Chem. C* **2020**, *8*, 1335–1343. [[CrossRef](#)]
403. He, W.; Lv, X.; Pan, F.; Li, X.; Yan, Z. Novel preparation process of iron powders with semisteel by rotary cup atomizer. *Powder Technol.* **2019**, *356*, 1087–1096. [[CrossRef](#)]
404. Huang, Y.; Hu, H.; Gong, H.; Xing, H.; Yuan, B.; Fu, B.; Li, A.; Yao, H. Mechanism study of selenium retention by iron minerals during coal combustion. In *Proceedings of the Combustion Institute*; Elsevier Ltd.: Amsterdam, The Netherlands, 2021; Volume 38, pp. 4189–4197.
405. Marinca, T.F.; Chicinaş, H.F.; Neamtu, B.V.; Popa, F.; Chicinaş, I. Reactive spark plasma sintering of mechanically activated $\alpha\text{-Fe}_2\text{O}_3/\text{Fe}$. *Ceram. Int.* **2017**, *43*, 14281–14291. [[CrossRef](#)]
406. Mu, Y.; Ai, Z.; Zhang, L.; Song, F. Insight into core-shell dependent anoxic Cr(VI) removal with $\text{Fe}@\text{Fe}_2\text{O}_3$ nanowires: Indispensable role of surface bound Fe(II). *ACS Appl. Mater. Interfaces* **2015**, *7*, 1997–2005. [[CrossRef](#)]
407. Wu, W.; Xiao, X.; Zhang, S.; Zhou, J.; Fan, L.; Ren, F.; Jiang, C. Large-scale and controlled synthesis of iron oxide magnetic short nanotubes: Shape evolution, growth mechanism, and magnetic properties. *J. Phys. Chem. C* **2010**, *114*, 16092–16103. [[CrossRef](#)]
408. Shen, H.; Liu, B.; Zhao, S.; Zhang, J.; Yuan, J.; Zhang, Y.; Zhang, S. Iron oxide and jadeite nucleation in high alumina glass-ceramics prepared from secondary aluminum dross. *Ceram. Int.* **2021**, *47*, 21744–21750. [[CrossRef](#)]
409. Prim, S.R.; Folgueras, M.V.; de Lima, M.A.; Hotza, D. Synthesis and characterization of hematite pigment obtained from a steel waste industry. *J. Hazard. Mater.* **2011**, *192*, 1307–1313. [[CrossRef](#)]
410. Chen, H.; Lin, H.; Zhang, P.; Yu, L.; Chen, L.; Huang, X.; Jiao, B.; Li, D. Immobilisation of heavy metals in hazardous waste incineration residue using $\text{SiO}_2\text{-Al}_2\text{O}_3\text{-Fe}_2\text{O}_3\text{-CaO}$ glass-ceramic. *Ceram. Int.* **2021**, *47*, 8468–8477. [[CrossRef](#)]
411. Karnik, B.S.; Baumann, M.J.; Corneal, L.M.; Masten, S.J.; Davies, S.H. TEM characterization of iron-oxide-coated ceramic membranes. *J. Mater. Sci.* **2009**, *44*, 4148–4154. [[CrossRef](#)]
412. Ocaña, M.; Caballero, A.; González-Carreño, T.; Serna, C.J. Preparation by pyrolysis of aerosols and structural characterization of Fe-doped mullite powders. *Mater. Res. Bull.* **2000**, *35*, 775–788. [[CrossRef](#)]
413. Shi, Y.; Han, X.X.; Li, B.W.; Chen, Y.X.; Zhang, M.X. Modification of glass network and crystallization of $\text{CaO}\text{-Al}_2\text{O}_3\text{-MgO}\text{-SiO}_2$ based glass ceramics with addition of iron oxide. *Ceram. Int.* **2020**, *46*, 9207–9217. [[CrossRef](#)]
414. Karamanov, A.; Paunović, P.; Ranguelov, B.; Ljatifi, E.; Kamusheva, A.; Načevski, G.; Karamanova, E.; Grozdanov, A. Vitrification of hazardous Fe-Ni wastes into glass-ceramic with fine crystalline structure and elevated exploitation characteristics. *J. Environ. Chem. Eng.* **2017**, *5*, 432–441. [[CrossRef](#)]
415. Karamanov, A.; Kamusheva, A.; Karashanova, D.; Ranguelov, B.; Avdeev, G. Structure of glass-ceramic from Fe-Ni wastes. *Mater. Lett.* **2018**, *223*, 86–89. [[CrossRef](#)]
416. Shankhwar, N.; Srinivasan, A. Evaluation of sol-gel based magnetic 45S5 bioglass and bioglass-ceramics containing iron oxide. *Mater. Sci. Eng. C* **2016**, *62*, 190–196. [[CrossRef](#)]
417. Zhou, W.; Ge, L.; Chen, Z.G.; Liang, F.; Xu, H.Y.; Motuzas, J.; Julbe, A.; Zhu, Z. Amorphous iron oxide decorated 3D heterostructured electrode for highly efficient oxygen reduction. *Chem. Mater.* **2011**, *23*, 4193–4198. [[CrossRef](#)]
418. Nitnavare, R.; Bhattacharya, J.; Thongmee, S.; Ghosh, S. Photosynthetic microbes in nanobiotechnology: Applications and perspectives. *Sci. Total Environ.* **2022**, *841*, 156457. [[CrossRef](#)]
419. Rufus, A.; Sreeju, N.; Philip, D. Synthesis of biogenic hematite ($\alpha\text{-Fe}_2\text{O}_3$) nanoparticles for antibacterial and nanofluid applications. *RSC Adv.* **2016**, *6*, 94206–94217. [[CrossRef](#)]
420. Dave, S.; Dave, S.; Mathur, A.; Das, J. Biological synthesis of magnetic nanoparticles. In *Nanobiotechnology: Microbes and Plant Assisted Synthesis of Nanoparticles, Mechanisms and Applications*; Elsevier: Amsterdam, The Netherlands, 2021; pp. 225–234. ISBN 9780128228784.
421. Buchanan, D.M.; Newsome, L.; Lloyd, J.R.; Kazemian, M.; Kaulich, B.; Araki, T.; Bagshaw, H.; Waters, J.; van der Laan, G.; N'Diaye, A.; et al. Investigating Nanoscale Electron Transfer Processes at the Cell-Mineral Interface in Cobalt-Doped Ferrihydrite Using Geobacter sulfurreducens: A Multi-Technique Approach. *Front. Earth Sci.* **2022**, *10*, 799328. [[CrossRef](#)]
422. Kishor, B.; Rawal, N. Studies on natural biogenic iron oxides for removal of copper (II) ion from aqueous solution. *Desalin. Water Treat.* **2017**, *88*, 145–153. [[CrossRef](#)]
423. Li, D.; Zhou, J.; Chen, X.; Song, H. Amorphous Fe_2O_3 /Graphene Composite Nanosheets with Enhanced Electrochemical Performance for Sodium-Ion Battery. *ACS Appl. Mater. Interfaces* **2016**, *8*, 30899–30907. [[CrossRef](#)]
424. Enman, L.J.; Kast, M.G.; Cochran, E.A.; Pledger, E.; Stevens, M.B.; Boettcher, S.W. Transition-Metal-Incorporated Aluminum Oxide Thin Films: Toward Electronic Structure Design in Amorphous Mixed-Metal Oxides. *J. Phys. Chem. C* **2018**, *122*, 13691–13704. [[CrossRef](#)]
425. Li, Y.; Wang, X.; Ding, B.; He, C.; Zhang, C.; Li, J.; Wang, H.; Li, Z.; Wang, G.; Wang, Y.; et al. Synergistic Apoptosis-Ferroptosis: Oxaliplatin loaded amorphous iron oxide nanoparticles for High-efficiency therapy of orthotopic pancreatic cancer and CA19-9 levels decrease. *Chem. Eng. J.* **2023**, *464*, 142690. [[CrossRef](#)]

426. Ioffe, M.; Kundu, S.; Perez-Lapid, N.; Radian, A. Heterogeneous Fenton catalyst based on clay decorated with nano-sized amorphous iron oxides prevents oxidant scavenging through surface complexation. *Chem. Eng. J.* **2022**, *433*, 134609. [[CrossRef](#)]
427. Chandrababu, P.; Cherian, S.; Raghavan, R. Aloe vera leaf extract-assisted facile green synthesis of amorphous Fe_2O_3 for catalytic thermal decomposition of ammonium perchlorate. *J. Therm. Anal. Calorim.* **2020**, *139*, 89–99. [[CrossRef](#)]
428. Lin, Z.; Du, C.; Yan, B.; Yang, G. Amorphous Fe_2O_3 for photocatalytic hydrogen evolution. *Catal. Sci. Technol.* **2019**, *9*, 5582–5592. [[CrossRef](#)]
429. Zhao, Q.; Liu, J.; Li, X.; Xia, Z.; Zhang, Q.; Zhou, M.; Tian, W.; Wang, M.; Hu, H.; Li, Z.; et al. Graphene oxide-induced synthesis of button-shaped amorphous Fe_2O_3 /rGO/CNFs films as flexible anode for high-performance lithium-ion batteries. *Chem. Eng. J.* **2019**, *369*, 215–222. [[CrossRef](#)]
430. Persdotter, A.; Boll, T.; Jonsson, T. Minor element effect on high temperature corrosion of a low-alloyed steel: Insight into alkali- and chlorine induced corrosion by means of atom probe tomography. *Corros. Sci.* **2021**, *192*, 109779. [[CrossRef](#)]
431. Jiang, L.; Fu, J.; He, C. Reliability analysis of wood-plastic composites in simulated seawater conditions: Effect of iron oxide pigments. *J. Build. Eng.* **2020**, *31*, 101318. [[CrossRef](#)]
432. Singh, S.; Singh, G.; Bala, N. Electrophoretic deposition of Fe_3O_4 nanoparticles incorporated hydroxyapatite-bioglass-chitosan nanocomposite coating on AZ91 Mg alloy. *Mater. Today Commun.* **2021**, *26*, 101870. [[CrossRef](#)]
433. Nikravesh, B.; Ramezanzadeh, B.; Sarabi, A.A.; Kasiriha, S.M. Evaluation of the corrosion resistance of an epoxy-polyamide coating containing different ratios of micaceous iron oxide/Al pigments. *Corros. Sci.* **2011**, *53*, 1592–1603. [[CrossRef](#)]
434. Fan, C.; Shi, J.; Sharafeev, A.; Lemmens, P.; Dilger, K. Optical spectroscopic and electrochemical characterization of oxide films on a ferritic stainless steel. *Mater. Corros.* **2020**, *71*, 440–450. [[CrossRef](#)]
435. Gareev, K.G.; Grouzdev, D.S.; Kharitonskii, P.V.; Kosterov, A.; Koziaeva, V.V.; Sergienko, E.S.; Shevtsov, M.A. Magnetotactic bacteria and magnetosomes: Basic properties and applications. *Magnetochemistry* **2021**, *7*, 86. [[CrossRef](#)]
436. Toropova, Y.G.; Golovkin, A.S.; Malashicheva, A.B.; Korolev, D.V.; Gorshkov, A.N.; Gareev, K.G.; Afonin, M.V.; Galagudza, M.M. In vitro toxicity of Fe_mO_n , $\text{Fe}_m\text{O}_n\text{-SiO}_2$ composite, and $\text{SiO}_2\text{-Fe}_m\text{O}_n$ core-shell magnetic nanoparticles. *Int. J. Nanomed.* **2017**, *12*, 593–603. [[CrossRef](#)]
437. Toropova, Y.G.; Zelinskaya, I.A.; Gorshkova, M.N.; Motorina, D.S.; Korolev, D.V.; Velikonivtsev, F.S.; Gareev, K.G. Albumin covering maintains endothelial function upon magnetic iron oxide nanoparticles intravenous injection in rats. *J. Biomed. Mater. Res.—Part A* **2021**, *109*, 2017–2026. [[CrossRef](#)] [[PubMed](#)]
438. Kharitonskii, P.; Zolotov, N.; Kirillova, S.; Gareev, K.; Kosterov, A.; Sergienko, E.; Yanson, S.; Ustinov, A.; Ralin, A. Magnetic granulometry, Mössbauer spectroscopy, and theoretical modeling of magnetic states of $\text{Fe}_m\text{O}_n\text{-Fe}_{m-x}\text{Ti}_x\text{O}_n$ composites. *Chin. J. Phys.* **2022**, *78*, 271–296. [[CrossRef](#)]
439. Gareev, K.G.; Grouzdev, D.S.; Koziaeva, V.V.; Sitkov, N.O.; Gao, H.; Zimina, T.M.; Shevtsov, M. Biomimetic Nanomaterials: Diversity, Technology, and Biomedical Applications. *Nanomaterials* **2022**, *12*, 2485. [[CrossRef](#)] [[PubMed](#)]

Disclaimer/Publisher's Note: The statements, opinions and data contained in all publications are solely those of the individual author(s) and contributor(s) and not of MDPI and/or the editor(s). MDPI and/or the editor(s) disclaim responsibility for any injury to people or property resulting from any ideas, methods, instructions or products referred to in the content.